April 20, 2006

Beth Nerrie
SRA International
2801 Clarendon Blvd, Suite 100
Arlington, VA 22201

Re: GE-Pittsfield/Housatonic River Site
Rest of River
Comments on EPA's Model Validation Report

Dear Ms. Nerrie:

In accordance with Peer Review process for EPA's Model Validation Report (MVR) for the Housatonic River (dated March 2006), I am enclosing a document entitled *General Electric Company's Comments on the EPA Model Validation: Modeling of PCB Contamination in the Housatonic River,* which was prepared on GE's behalf by Quantitative Environmental Analysis. This document presents GE's comments on the MVR for consideration by the Peer Review Panel. These comments address the specific questions in the MVR charge, which the Peer Review Panel will be using to evaluate the MVR.

To assist in the distribution of this document to the Peer Review Panel, the document is being provided to SRA in three different formats: an electronic-PDF file format sent via email to gepittsfield@sra.com and followed up with paper-bound and paper-unbound formats sent via Federal Express.

Please let me know if you have any questions.

Very truly yours,

Andrew Silfer, P.E.
GE Project Coordinator

Enclosures

cc: Susan Svirsky, EPA
      Dean Tagliaferro, EPA
      Timothy Conway, EPA
      Holly Inglis, EPA
      Rose Howell, EPA (w/o encl.)
      Susan Steenstrup, MDEP
      Susan Peterson, MDEP
      Michael Carroll, GE
      Rod McLaren, GE
      Kevin Mooney, GE
      James Rhea, QEA
      Kevin Russell, QEA
      James Bieke, Goodwin Procter
      Samuel Gutter, Sidley Austin
      Dale Young, MA EOEA

General Electric Company's Comments on the EPA Model Validation: Modeling Study of PCB Contamination in the Housatonic River

Prepared for:

General Electric Company

Pittsfield, MA

Prepared by:

Quantitative Environmental Analysis, LLC

Liverpool, NY

April 19, 2006

Table of Contents

SECTION 1
INTRODUCTION

1.1   BACKGROUND

On behalf of General Electric Company (GE), Quantitative Environmental Analysis, LLC (QEA) has prepared these comments on the U.S. Environmental Protection Agency's (EPA's) document titled *Model Validation: Modeling Study of PCB Contamination in the Housatonic River* (Model Validation Report or MVR; Weston 2006a). The MVR describes the final phase of a three-phase modeling effort of the fate, transport, and bioaccumulation of polychlorinated biphenyls (PCBs) in the Housatonic River. The first phase included the development of a Model Framework Design (MFD; Weston 2000a) and Quality Assurance Project Plan (QAPP; Weston 2000b), which described the modeling plans for this system. These plans were subject to peer review in April 2001 and subsequently reissued by EPA in April 2004 (Weston 2004b). The second phase of the modeling effort included the development and calibration of watershed, hydrodynamic, sediment transport, PCB fate and transport, and PCB bioaccumulation models of the Housatonic River between the confluence of the East and West Branches and Woods Pond Dam (the Primary Study Area or PSA), and was documented in the Model Calibration Report (MCR; Weston 2004a). The MCR was peer reviewed in May 2005, and based upon the written comments from the Peer Review Panel submitted in July 2005, EPA developed a Responsiveness Summary (MCR-RS) in January 2006 (Weston 2006b). The MVR documents the third phase of the modeling effort, which includes the Phase 2 calibration, sensitivity/uncertainty analysis, and validation of the suite of models described in the MCR. Furthermore, the MVR documents the efforts associated with both upstream and downstream expansions of the model domain. Upon completion of the peer review for the MVR, EPA will provide the model (including the computer code as well as the input and output files) to GE for use in evaluating remedial alternatives as part of the Corrective Measures Study (CMS) for the Rest of River portion of the GE-Pittsfield/Housatonic River Site.

This document presents GE's comments on the MVR for consideration by the Peer Review Panel.

1.2 OVERVIEW OF CHANGES MADE TO THE MODEL SINCE THE MCR PEER REVIEW

Since the May 2005 model calibration peer review, EPA has made a number of changes to the models; many of those changes were based on the recommendations of the Peer Review Panel. The major changes to the model framework, the model domain, the overall approach to calibration and validation, and the methods for sensitivity/uncertainty analyses that were implemented by EPA during the validation phase are described in the following sections.

1.2.1 Model Framework

As documented in the MCR-RS and the MVR, a number of additions and changes have been made to the framework of the Environmental Fluid Dynamics Code (EFDC) model, which is the code used to simulate hydrodynamics, sediment transport, and PCB fate and transport. These include:

- A different formulation for grain-related shear stress was implemented to increase the mobilization of the largest simulated non-cohesive sediment size class (see Section 4.1.1 of the MVR).

- A formulation to represent bank erosion and slumping was developed and included in the model framework (see Section 4.1.4 of the MVR).

- The approach used to specify incoming PCB loads from the East and West Branches as a function of river flow rate was modified (see Section 4.1.5 of the MVR).

- Model hindcast simulations were conducted to develop scaling factors that were subsequently used to specify the sediment PCB initial conditions for the beginning of the Phase 2 calibration and validation periods (see Section 4.1.6 of the MVR).

- An extensive review of freshwater bioturbation literature and Housatonic River benthic invertebrate data was conducted and used to support a reduction in the model's

specification of the bioavailable depth (that sediment depth from which PCBs potentially enter the food chain) from 15 cm to 4 to 10 cm (see Section 4.1.7 of the MVR and Attachment 1 of the MCR-RS).

- Volatilization of PCBs was included in the processes simulated by the EFDC fate and transport model (see Section 4.1.8 of the MVR).

1.2.2 Model Domain

The MVR includes a description of two expansions of the reach of the river that is simulated by the EPA's model framework:

1. The model domain was extended upstream approximately two miles from the confluence, to Newell Street Bridge. A separate EFDC model (the upstream model) was developed for this reach to simulate hydrodynamics, sediment transport, and PCB fate and transport (see Section 8 of the MVR). The model was extended to include this reach so that specification of boundary conditions (i.e., relationships between stage height, flow rate, and TSS) for future simulations with the model would not be impacted by changes to the river morphology that have resulted from remediation activities within this section of the river.

2. EPA's model domain was also extended downstream a distance of 19 miles, to Rising Pond Dam. Separate EFDC and Food Chain Model (FCM) applications (the downstream model) were developed to simulate this reach of the river (see Section 6.4 of the MVR). This extension of the model provided additional tests for the validation, and is intended to provide the ability to assess the impacts of potential remedial scenarios on this section of the river.

1.2.3 Calibration/Validation Approach

In response to comments from the MCR Peer Review Panel that 14 months was too short a period for model calibration, EPA modified the modeling approach to simulate longer

timeframes. First, the calibration was extended to span a period of approximately 10 years, from 1990 to 2000. Calibration of the EFDC and FCM models was conducted over this period, and results are presented as the Phase 2 calibration in Section 4 of the MVR. Likewise, a long-term period was selected for model validation, which spans from 1979 to 2005. For model validation, EPA did not include data from the Phase 2 calibration period in model-data comparisons.

1.2.4   Sensitivity/Uncertainty Analyses

Model sensitivity and uncertainty were not fully characterized during the calibration phase of EPA's modeling effort. In the MVR, the sensitivity analysis for EFDC was expanded to include additional parameters, and to cover the longer timeframe of the Phase 2 calibration period. Furthermore, uncertainty analyses were conducted for each of the component models in EPA's framework. Specifically:

- a Monte Carlo analysis was conducted to assess the uncertainty of the HSPF watershed model;

- due to the computational burden of EFDC simulations, a unique Kolmogorov-Smirnov approach was used to construct confidence limits for that model's outputs; and

- a Monte Carlo approach was used to quantify the uncertainty of FCM.

The uncertainty analysis was conducted in series so that the uncertainty of HSPF was propagated through EFDC, and that of EFDC was included in the quantification of FCM's uncertainty.

1.3   THE PEER REVIEW CHARGE FOR MODEL VALIDATION

The charge for the modeling peer review includes a number of specific questions relating to the model validation, as well as the Phase 2 calibration. A summary of GE's major comments

as they pertain to these charge questions is provided below. A detailed discussion is provided in Sections 2 through 7 of this document.

1. Considering the changes implemented in the Phase 2 Calibration, does the model as calibrated and validated, based on your technical judgment, reasonably account for the relevant processes affecting PCB fate, transport, and bioaccumulation in the Housatonic River to a degree consistent with achieving the goal of the modeling study?

- The formulation developed for bank erosion is not consistent with accepted theory and published literature and produces estimates of annual solids loads due to bank erosion that are lower than other data-based estimates (details in Section 2.1).

- The model does not capture the general decrease shown by the data in water column PCB concentrations across Woods Pond during low flows, which indicates that the balance among the various fate processes is incorrectly represented (details in Section 3.2.2).

2. Are the comparisons of the model predictions with data sufficient to evaluate the capability of the model on the spatial and temporal scales of the final calibration and validation?

- Given the limited presentation of model results in the MVR, the ability of the model to simulate trends in sediment PCBs cannot be fully evaluated. Further comparisons of model results with additional treatments of the data as well as other data sets are needed to better assess the model (details in Section 3.3.1).

- The documentation of the modeling is incomplete in some cases. Additional modeling results are needed to allow a full evaluation of the Phase 2 calibration and validation (details in Section 7.1).

- The upstream model, as presented in the MVR, is incomplete and cannot be considered fully validated given that PCB fate and transport were not simulated and the model-data comparisons are insufficient (details in Section 7.2).

- The downstream model, as presented in the MVR, is incomplete and cannot be considered fully validated since model results were not compared against available data sets for TSS, water column PCBs, and sediment PCBs (details in Section 7.3).

3. Is there evidence of bias in the models, as indicated by the distribution of residuals of model/data comparisons?

- Model predictions of TSS at low flow are biased high, which leads to an under-prediction of particulate-phase PCBs in the water column. Through compensation in the FCM calibration, this would likely result in an overprediction by the FCM of the relative contribution of sediment-derived PCB sources to fish tissue PCB concentrations (details in Section 3.1).

- Low flow water column PCB concentrations are consistently over-predicted in both the East Branch boundary condition and at Holmes Road. Because the model better matches concentrations at downstream locations, this bias in the upper reach suggests that low flow PCB fate processes and/or the balance between external and internal PCB sources are not represented correctly (details in Section 3.2.1).

- The model predictions of surface sediment PCB concentrations appear to exceed the data at the end of the validation period in some cases. This potential bias could result in an over-prediction by the bioaccumulation model of the proportion

of PCB obtained by fish from the water column relative to the sediments (details in Section 3.3.2).[*]

4. Have the sensitivities of the models to the parameterization of the significant state and process variables been adequately characterized?

- Additional model results and analyses are required to fully address the sensitivity of the sediment transport model, and the PCB fate model sensitivity results at low flows appear to contain contradictory results with regard to the pore water diffusion process (details in Section 4.1).

5. Are the uncertainties in model output(s) acknowledged and described?

- The approach used to develop initial sediment PCB concentrations for the Phase 2 calibration and validation periods precludes a robust test of long-term model predictions and therefore should have been evaluated through sensitivity and uncertainty analyses. Additionally, development of these initial conditions is not documented with sufficient detail (details in Section 2.2).

- The uncertainty analysis approach presented in the MVR cannot be used to evaluate uncertainty in the model simulations conducted during the CMS because it produces ranges of PCB concentrations that lie far outside of the bounds of the field data and because the computational burden of running numerous EFDC simulations renders that approach infeasible (details in Section 4.2).

---

[*] Note that potential offsetting biases in predicting the relative contributions of water column PCB sources versus sediment sources are not acceptable, because if PCB or TSS concentrations change in differing relative amounts in future projections, the biases will result in incorrect predictions of fish tissue PCB levels.

6. Upon review of the model projections of changes in PCB concentrations in environmental media in the example scenarios, are such projections reasonable, using your technical judgment, and are they plausible given the patterns observed in the data?

- Because GE will need to use the model to evaluate remedial scenarios during the CMS, it is critical that the MVR provide a good indication of how the model will behave during long-term future simulations. The example scenarios presented in the MVR do not provide that information because they do not project forward from the end of the validation period and because they do not include FCM results (details in Section 6).

7. Is the final model framework, as calibrated and validated, adequate to achieve the goal of the modeling study to simulate future conditions 1) in the absence of remediation and 2) for use in evaluating the effectiveness of remedial alternatives?

- Simulation times must be of reasonable duration in order to use the model for its intended purpose of evaluating alternative remedial scenarios. The simulation time for EFDC is too long to efficiently evaluate long-term simulations of remedial alternatives during the CMS (details in Section 5.1).

- There are some indications that the EFDC model may not be computationally stable; additional evaluation is needed to assess that issue (details in Section 5.2).

SECTION 2
CHANGES MADE TO THE MODEL FRAMEWORK AND APPROACH

With regard to the changes EPA made to its modeling framework and approach that are presented in the MVR, GE has concerns with two of these changes. First, the formulation developed to represent bank erosion is not consistent with the accepted conceptual model of how this process occurs. Second, the approach used to develop sediment bed PCB concentrations for the beginning of the Phase 2 calibration and validation periods does not provide for a robust test of long-term model predictions.

2.1   BANK EROSION

MVR Charge Reference:

- ***Question 1 (model's ability to account for relevant PCB fate, transport, and bioaccumulation processes)***

As documented in the MVR (Section 4.1.4), EPA developed an empirical approach to simulate bank erosion. The model formulation includes two components that contribute equally to the total bank erosion: a term that simulates a continuous release of bank soils, and a second term that represents bank failure on the receding limb of a storm hydrograph. Both terms include a power function that computes the solids loading rate from bank erosion based on river flow rate at the confluence.

In several respects, the approach adopted by EPA is not supported by accepted theory or the literature:

- No justification or literature support is provided for the theoretical basis of the model formulations, or for the assumed equal split between continuous erosion and mass failure. The MVR states (Page 4-5) that information regarding the split between the two bank

erosion processes could not be located in the literature; however, the potential effects of this important assumption on sediment transport and PCB fate and transport simulations were not evaluated during the model sensitivity analysis.

- The assumption that continuous erosion occurs at all flow rates (i.e., that there is no threshold velocity or shear stress for initiation of bank erosion; MVR Pages 4-5 to 4-6) is inconsistent with the accepted conceptual model of bank erosion that is presented in the peer-reviewed literature (e.g., Millar and Quick 1998; Alonso and Combs 1990; and Osman and Thorne 1988 – all included in Attachment 1).

- Insufficient detail is provided on how the bank erosion model was parameterized. First, no justification is provided for the choice of the flow criteria used in the MVR (Page 4-6) to specify when mass failure occurs (i.e., when Coltsville flow is between 600 and 250 cfs and decreasing at a rate of 5 cfs/hour or greater). Second, the precision of estimated changes in top-of-bank locations from the 1972 aerial photographs (MVR Page 4-7) is not discussed nor presented. Were analyses conducted to evaluate the uncertainty in the estimates (e.g., comparison of changes in fixed locations, such as buildings, between the 1972 and 2000 photos)? Finally, the MVR also states (Page 4-6) that the approach used by EPA is preferable to alternate approaches because it eliminates the need to calibrate empirical constants within EFDC simulations. However, no information is provided to support this assertion. In addition, the model used by EPA contains empirical constants that were adjusted individually to calibrate the model to bank erosion rates estimated at 69 locations (i.e., the coefficients a and b; MVR Pages 4-5 and 4-6), which brings into question the validity of this statement.

In addition, this approach results in lower estimates of annual solids loads due to bank erosion than the data-based estimates of such annual loads reported in the MCR and the RFI Report (BBL and QEA 2003), as shown in Table 2-1.

Table 2-1. Estimates of annual average solids load from bank erosion.

Approach and Data Used	Reference	Solids Loading from Bank Erosion (MT/yr)
Analysis used for model. Based on 1972 and 2000 aerial photographs.	MVR Section 4.1.4	840
Long-term rate based on 1952 and 2000 aerial photographs.	MCR Table B.4.1	1376
Short-term rates based on 2000-2002 EPA toe pin study.	MCR Table B.4.1	1197
Estimates based on 1998 EPA maps of eroding banks and average migration rates from 2000-2002 EPA toe pin study and 2001-2002 EPA meander survey study.	RFI Report Section 8.8.1.9 (copy in Attachment 2 to these comments)	1400 to 3200

The formulation developed for bank erosion is not consistent with accepted theory and published literature and produces estimates of annual solids loads due to bank erosion that are lower than other data-based estimates.

2.2   DEVELOPMENT OF SEDIMENT PCB INITIAL CONDITIONS

MVR Charge Reference:

- *Question 5 (acknowledgement of model uncertainties)*

To establish initial sediment PCB concentrations for the beginning of the Phase 2 calibration period (i.e., 1990) and the validation period (i.e., 1979), a "hindcast" approach was used. In this approach, preliminary long-term simulations were conducted to quantify the model-predicted rates of change for various sediment segments (e.g., individual grid cells or reach averages). These rates were then used in conjunction with the sediment PCB data from the Phase 1 calibration period (i.e., 1998-99) to estimate the 1990 and 1979 initial conditions (MVR Section 4.1.6). The limited data in the earlier years (i.e., 1980 and 1990) were given as the reason for using this approach (MVR Page 4-9). GE has two comments regarding this approach:

- EPA's approach does not allow for a robust test of the model's predicted long-term temporal trends. Using the model's temporal trend and concentrations at the end of the simulation to estimate initial conditions essentially precludes an independent evaluation

of the model's ability to simulate long-term processes in the system. At a minimum, this limitation should be acknowledged in the MVR and its implications should be discussed. Additionally, sensitivity/uncertainty analyses should have been conducted to evaluate how this approximation affected model predictions.

- Additional information on how the initial conditions for the Phase 2 calibration and validation were developed is needed to fully assess the model. Specifically, comparisons between the estimated initial conditions and the data collected in 1990 and 1979-1980 should be made to evaluate whether this approach produced initial conditions that are consistent with the data. At a minimum, a set of plots showing the initial conditions, as well as a comparison with the 1979-1982 data (beyond that provided in the validation result figures), should have been provided. Furthermore, no information is provided on how initial conditions were established for sediment PCBs below the surface. Was the same approach used? Or, were the 1998-1999 data for depths below 6" assigned for the 1990 and 1980 initial conditions?

The approach used to develop initial sediment PCB concentrations for the Phase 2 calibration and validation periods precludes a robust test of long-term model predictions and therefore should have been evaluated through sensitivity and uncertainty analyses. Additionally, development of these initial conditions is not documented with sufficient detail.

SECTION 3
PHASE 2 CALIBRATION AND VALIDATION RESULTS

Upon review of the Phase 2 calibration and validation results in the MVR, GE has two concerns. First, the model results indicate high biases in both TSS and water column PCB concentrations during low flow periods. Second, the predicted long-term trends in sediment PCBs are not adequately evaluated or documented with sufficient detail, and appear to be inconsistent with the data in some cases.

3.1   TSS CONCENTRATIONS AT LOW FLOW

MVR Charge Reference:

- *Question 3 (evidence of bias in the models)*

The model-data comparisons that are presented for the Phase 2 calibration and the validation in the MVR indicate that the sediment transport model consistently over-predicts TSS at non-storm flows. This result appears to stem largely from the East Branch boundary conditions, in which the model values in the East Branch at base flows are typically on the order of 10 mg/L, except on days of sampling, when they are "forced" to match the data, which typically are in the 2-5 mg/L range (e.g., MVR Figures 4.2-31 and 6.2-12). This problem with the boundary condition appears to propagate downstream, as over-prediction of the routine non-storm TSS data is clearly visible at Holmes Road (e.g., MVR Figures 4.2-38 and 6.2-19) and New Lenox Road (e.g., MVR Figures 4.2-39 and 6.2-20), while the differences are less evident at the Woods Pond Headwaters and Footbridge stations.

The high bias in low flow TSS concentrations is acknowledged in the MVR, but the report states that low flow data are less important for the long-term mass balance (MVR Page 6-57). Indeed, in the MVR's presentation of statistical metrics of model performance for the validation, an alternative set of results that censor the <5 mg/L data (i.e., MVR Tables 6.2-5

and 6.2-6) is included. However, it is inappropriate to dismiss this apparent bias in low flow TSS in this manner. Although EPA's assessment that this bias does not impact the overall sediment mass balance may be correct, low flow TSS concentrations do impact prediction of water column PCB concentrations. For example, at a given total PCB concentration, over-predicting TSS of 2 mg/L as 10 mg/L will cause the calculated PCB concentrations on water column particulate matter (which determine the particulate organic matter (POM) exposures used in the FCM) to be under-predicted by about a factor of two (based on the partitioning parameters used in the EPA's model). Because the FCM predictions of fish tissue PCB concentrations generally match the data, it is likely that this under-prediction in particulate-phase PCB concentrations in the water column was compensated for during the calibration of the FCM by increasing the predicted contribution from sediment-based PCB sources. In other words, under-predicting PCB concentrations on POM would require specification of a larger amount of sediment-derived PCBs to obtain the same body burden in fish. Thus, the bias in low flow TSS may have resulted in an incorrect representation of the balance between water column and sediment PCB uptake by fish.

Model predictions of TSS at low flow are biased high, which leads to an under-prediction of particulate-phase PCBs in the water column. Through compensation in the FCM calibration, this would likely result in an overprediction by the FCM of the relative contribution of sediment-derived PCB sources to fish tissue PCB concentrations.

3.2   WATER COLUMN PCB CONCENTRATIONS AT LOW FLOW

3.2.1   Over-prediction of Low Flow Water Column PCB Concentrations in East Branch Boundary Condition and Reach 5A

MVR Charge References:
- ***Question 1 (model's ability to account for relevant PCB fate, transport, and bioaccumulation processes)***

- ***Question 3 (evidence of bias in the models)***

High Bias in East Branch Boundary Condition

The temporal plots presenting the water column PCB concentrations at Pomeroy Avenue (i.e., MVR Figures 4.2-63 and 6.2-39) indicate that the East Branch PCB boundary condition is biased high during non-storm conditions, for both the Phase 2 calibration and validation periods. As shown on those figures, comparison of the model boundary conditions with the data indicates that a majority of the routine (non-storm) data are over-estimated by a factor of two to five, or more. It appears that the boundary condition functions developed for the East Branch have not properly represented the non-detect samples, although the boundary condition is forced through the individual non-detect data points over a two-day period when data exist. The resulting predicted PCB concentrations at Pomeroy Avenue for non-storm flows (i.e., baseline concentrations) are approximately 100 ng/L throughout the Phase 2 calibration and validation periods, even though samples were in the 20-50 ng/L range, with many below the method detection limit (MDL), which are plotted at the ½ MDL value of approximately 10 ng/L (see MVR Figures 4.2-63 and 6.2-39). This high bias in the East Branch boundary at low flows impacts model predictions of low flow water column PCBs at downstream locations in Reach 5A, and with it the calculated PCB exposures used by the bioaccumulation model at those locations, as discussed below.

High Bias in Reach 5A Predictions

The apparent high bias in low flow water column PCB concentrations at Pomeroy Avenue also appears to be evident in the model-data comparisons at Holmes Road for the Phase 2 calibration and validation periods (MVR Figures 4.2-65 and 6.2-41). This high bias may be a direct consequence of the over-prediction of the low flow PCB boundary condition. The MVR notes that the model results for Holmes Road compare well with the detected concentrations, but that the non-detects (NDs) are over-predicted (MVR Page 6-72). The MVR states that treating NDs as the MDL instead of ½ MDL would account for the high bias in the model predictions at Holmes Road. However, plotting the ND samples at the MDL would place them at approximately 20 ng/L; yet the model predictions at Holmes Road for non-storm flows are

almost always in the 30-100 ng/L range. Thus, the representation of ND samples does not fully account for this high bias.

In its discussion of the tendency to over-predict low flow PCB concentrations at Holmes Road, the MVR places much emphasis on the fact that the detected samples are matched by the model better than the non-detect samples (MVR Page 6-72). To some extent, the MVR discussion appears to trivialize the non-detect data, suggesting that over-prediction of the low flow PCB concentrations is unimportant. The report further states that low flow PCB concentrations are less important for long-term sediment and contaminant transport assessments (MVR Page 6-82). Finally, in its presentation of the statistical metrics of model performance, the MVR evaluates the model results compared to all the PCB data, as well as compared to just a censored subset of the PCB data for which PCBs <40 ng/L were excluded from the statistical comparisons (MVR Tables 6.2-10 and 6.2-11, respectively).

It is not correct to censor the data set in this way. First, the ND samples represent a significant portion of the data set used for Phase 2 calibration and validation (for example, over half of the routine samples from Holmes Road in 2001-2002 were non-detect). Moreover, these low flow data are important, and cannot be excluded from the overall assessment of model performance. Although data-based calculations and EPA's modeling have shown that high flow periods do account for a majority of the annual PCB mass transport, low flow PCB concentrations are important for evaluation of fish PCB exposure given the amount of time the river is at low flows, and given that PCB uptake by fish is greater during times of higher metabolic activity, which occur in the summer when flows are generally low. In evaluating such PCB exposures, the high bias in predictions of low flow PCB concentrations in Reach 5A would likely lead, through compensation in the FCM calibration, to an under-prediction of the contribution of sediment-based PCBs sources to such exposures in that reach. Thus, that high bias is of greater consequence than suggested in the MVR since it likely impacts the FCM calibration in that reach.

Additional discussion of the importance of the bias in low flow PCB predictions is provided in Section 6.2.3.4 of the MVR. The discussion acknowledges the high bias, and states

that FCM bounding calculations that had all water column concentrations less than 60 ng/L replaced with zero resulted in changes in fish PCB concentrations of 5% to 8% (MVR page 6-87). However, it is not clear whether this bounding analysis accounted for the full set of data that are over-predicted, since model results in the range of 60-100 ng/L, which account for a larger portion of time than the <60 ng/L results, also reflect the high bias.

Furthermore, the report observes (Page 6-87) that the high biases in low flow TSS concentrations (see Section 3.1, above) and low flow PCB concentrations tend to offset each other in terms of predicted PCB concentrations on POM, thereby minimizing "the concern". However, it is unacceptable to rely on offsetting biases in model results for future applications of the model. If PCB or TSS concentrations in the inputs to future simulations change in differing relative amounts, the bias in one will result in incorrect predictions of PCBs on POM, which would in turn result in incorrect future predictions of fish tissue PCB concentrations.

Reach 5 PCB Fate Processes

The low flow results for water column PCBs at the New Lenox Road, Woods Pond Headwaters, and Woods Pond Footbridge locations exhibit smaller differences between the model and data than do the results from further upstream (e.g., MVR Figures 6.2-42 through 6.2-44). Because the model tends to match the low flow data at New Lenox Road, this indicates that the balance between upstream loads and internal sources within Reach 5A is incorrect at non-storm conditions.

Moreover, the PCB mass balance for the validation period (MVR Figure 6.2-63) indicates that the single largest load of PCBs in the model is advection from the East Branch (i.e., the boundary condition). This result is contrary to: 1) the analyses of available site data presented in the RFI Report, which indicated that sediments in Reaches 5A and 5B are the largest source of PCBs to Reach 5 (BBL and QEA 2003, Figure 9-2, a copy of which is provided as Attachment 3); and 2) the data-based computations developed by EPA as part of its flux analysis (MVR Figure 2.2). In these analyses, there is a net increase in PCB load from the confluence to New Lenox Road, by a factor of two to three. The model validation results, however, indicate a much

larger load entering from upstream, and as a consequence, a net loss of PCB mass occurs between the confluence and New Lenox Road, reflecting a twofold reduction. These mass balance results further illustrate that the balance between PCB loads from upstream versus those derived from sediments and banks in Reach 5A may be incorrect in EPA's model.

Low flow water column PCB concentrations are consistently over-predicted in both the East Branch boundary condition and at Holmes Road. Because the model better matches concentrations at downstream locations, this bias in the upper reach suggests that low flow PCB fate processes and/or the balance between external and internal PCB sources are not represented correctly.

3.2.2   Woods Pond Spatial Patterns

MVR Charge Reference:

- ***Question 1 (model's ability to account for relevant PCB fate, transport, and bioaccumulation processes)***

The predicted spatial pattern in low-flow water-column PCBs across Woods Pond (i.e., between Woods Pond Headwaters and Lenoxdale Bridge) that is shown in the Phase 2 calibration and validation results does not appear to be consistent with the routine data. Although a spatial plot comparing a longer-term average of low flow conditions with the routine data is not provided in the MVR, the spatial plots for averages of Phase 2 model calibration results from several 1999 events (e.g., MVR Figures 4.2-69 and 4.2-70) show little to no spatial gradient across the pond. The data, however, indicate a decline, which is consistent with the conceptual model of deposition processes occurring within the pond. Moreover, the text of the MVR states (Page 4-89) that PCBs decrease by 17% across Woods Pond, which is not consistent with the plots. Similar results are evident in the low flow spatial patterns for the validation, where the model results show no change in PCBs across the pond and the data suggest a decrease (e.g., MVR Figure 6.2-45).

Furthermore, inspection of the temporal plots for complete years with routine monitoring data (e.g., Phase 2 calibration for year 1997 from MVR Figures 4.2-67 and 4.2-68) indicates that the model tends to sufficiently match the low flow data from Woods Pond outlet, but under-predicts the data from Woods Pond Headwaters, thus missing the general decrease in PCB concentrations across the pond at low flows that is consistently indicated by the routine data. Similarly, the example model mass balance results for low flows (upper-left panel in MVR Figure 4.2-80) show no change in PCB load across Woods Pond, whereas data-based analyses of the low flow data presented in the RFI Report indicate a decrease of approximately 20% in low flow PCB load across the pond (BBL and QEA 2003, Figure 9-2, see Attachment 3). Again, these differences may indicate that the "balance" of PCB fate-determining processes is not reflective of what is occurring in the system.

The model does not capture the general decrease shown by the data in water column PCB concentrations across Woods Pond during low flows, which indicates that the balance among the various fate processes is incorrectly represented.

3.3   SEDIMENT PCB CONCENTRATIONS

3.3.1   Model-Data Comparison Metrics

MVR Charge Reference:
- *Question 2 (sufficiency of model-data comparisons)*

The MVR presents Phase 2 calibration and validation results for sediment PCBs in terms of temporal trends in model-predicted surface concentrations averaged over spatial bins that span approximately 0.2 to 0.9 river miles (MVR Figures 4.2-77 and 6.2-49). No representation of the model's variability within the spatial bins is provided and no presentation of model results has been made for deeper sediments. This additional information is needed to fully evaluate how accurately EPA's model can simulate trends in sediment PCB concentrations.

The data in the sediment PCB temporal figures are plotted as monthly averages +/-2 standard errors of the mean. It is unclear why the data were presented as monthly averages, given that surface sediment PCB concentrations tend to change on annual timescales (or slower). It would be more appropriate to plot these data as averages by year or by individual sampling program, especially since many of the sampling programs spanned several months such that the samples from individual months may not necessarily yield a representative sample of a given spatial bin. The presentation of monthly averages obscures the comparisons with the 1998-1999 data, and the model's ability to simulate the central tendency of those sampling events. If the data are plotted as averages by year or by individual sampling program, additional evaluation of whether the model predicts sediment PCB concentrations without bias would be permitted.

Furthermore, although the MVR recognizes the limited historical data, there are some years and locations for which the quantity of historical sampling data allows model-data comparisons (e.g., the 1980-1982 data set contains ~15 samples near River Mile 128 and over 10 samples in the River Mile 125.5 area, and the 1994-1996 dataset contains over 40 samples between the confluence and River Mile 134). In some cases, the model does not match the historical data, calling into question the "hindcast" procedure used to develop the initial conditions, and the model's ability to predict long-term trends in sediment PCBs. More detailed evaluation of sediment temporal trends, including evaluation of specific areas in the river with sufficient data to evaluate changes, should be conducted to better evaluate model performance.

Finally, additional information on temporal trends in sediment PCBs is provided by the finely segmented cores that were collected by GE and EPA from various locations within the PSA (primarily Woods Pond) and dated using radioisotope techniques (see Section 4.5.4 of the RFI Report, excerpts of which are provided in Attachment 4). Model results for sediment PCBs (or PCB concentrations on depositing particles) should be compared to the estimated sediment PCB temporal trends from those cores (e.g., Figures 4-21, 4-22, and 4-26 in the RFI Report; see Attachment 4) as an additional test of the model's ability to reproduce the available information on temporal trends in the system.

Given the limited presentation of model results in the MVR, the ability of the model to simulate trends in sediment PCBs cannot be fully evaluated. Further comparisons of model results with additional treatments of the data as well as other data sets are needed to better assess the model.

3.3.2   Model-Predicted Temporal Trends

MVR Charge Reference:
- *Question 3 (evidence of bias in the models)*

Upon viewing the model results for temporal trends in sediment PCBs (i.e., MVR Figures 4.2-77 and 6.2-49), it appears that the model averages over-predict the 1998-99 data (monthly averaged) for several spatial bins. Some of these differences may be due to the averaging techniques used for initial conditions, but in several spatial bins, the model mean is higher than a majority of the individual monthly averages of the data (e.g., Bins 135.13-134.89, 129.65-129.19, 128.69-128.07, and 125.84-124.94 in MVR Figure 6.2-49). Woods Pond provides the most robust data set to evaluate temporal trends in surface sediment PCBs predicted by the model. The validation results for Woods Pond suggest that the model may be under-predicting the rate of decline suggested by the data (MVR Figure 6-50). Although the model passes through the error bars of most monthly averages of the data, the predicted concentrations exceed the data means for 9 out of the 10 monthly averages between 1995 and 2004. Thus, the model's prediction of long-term trends in sediment PCBs appears problematic since the data at the end of the validation period are over-predicted in some cases.

The apparent over-prediction of sediment PCB concentrations at the end of the validation period has implications for the FCM. Because the FCM was calibrated based on the sediment concentrations predicted by EFDC, the FCM calibration must have compensated for a high bias in those predicted sediment concentrations in some manner. Again, it is likely that this compensation was achieved by assigning a higher proportion of uptake from water column food sources, which tend to have lower PCB concentrations than the sediments. Thus, as with the

biases discussed in Sections 3.1 and 3.2.1, the bias in EFDC predictions of sediment PCB concentrations can result in an incorrect FCM prediction of the proportion of sediment-derived versus water column-derived PCBs in fish.

The model predictions of surface sediment PCB concentrations appear to exceed the data at the end of the validation period in some cases. This potential bias could result in an over-prediction by the bioaccumulation model of the proportion of PCB obtained by fish from the water column relative to the sediments.

SECTION 4
SENSITIVITY AND UNCERTAINTY ANALYSES

4.1   SENSITIVITY ANALYSES

MVR Charge Reference:

-   ***Question 4 (characterization of model sensitivities)***

Sensitivity analyses for the EFDC model, which consisted of conducting model simulations over the Phase 2 calibration period with selected parameters varied by +/- 50%, are presented in Section 5.1 of the MVR.   Overall, the EFDC sensitivity analysis results for the hydrodynamic model appear reasonable; however, additional analysis of the model results is needed to fully evaluate how the sediment transport model is behaving. The sediment transport model sensitivity is quantified in terms of changes in mean and peak TSS flux.   However, because deposition and erosion processes are significant determinants of long-term PCB fate, the sediment transport sensitivity analyses should also evaluate how variations in input parameters affect gross deposition and erosion fluxes as well as net bed elevation changes over the 10-year Phase 2 calibration period.

In addition, the EFDC PCB fate sensitivity results indicate that there may be a problem with the model's simulation of low flow conditions. The low flow event sensitivity analysis results (MVR Figure 5.1-8) reveal that the PCB flux at New Lenox Road is sensitive to partition coefficients and the diffusion mass transfer coefficient (e.g., sensitivity of 60-90%), as would be expected given the importance of pore water diffusion under low flow conditions. However, the results presented for the PCB flux at Woods Pond Footbridge from the same analysis (MVR Figure 5.1-9) show virtually no response to these parameters (sensitivity of 1% or less). If diffusion is the major PCB fate process at low flow across the PSA, it would be expected that the water column PCB concentrations at Woods Pond would respond to changes in the parameters affecting diffusion. At a minimum, the sensitivity of the flux passing New Lenox Road should be reflected at Woods Pond Footbridge in the absence of any additional inputs between these two

locations. It is unclear why one portion of the model domain exhibits a response to the diffusive flux parameters, while a portion further downstream does not. These results suggest that there may be a problem with the sensitivity results, or that low flow PCB fate processes may be misrepresented within Woods Pond.

Additional model results and analyses are required to fully address the sensitivity of the sediment transport model, and the PCB fate model sensitivity results at low flows appear to contain contradictory results with regard to the pore water diffusion process.

4.2   UNCERTAINTY ANALYSES

MVR Charge References:
- *Question 5 (model uncertainty)*
- *Question 7 (model's ability to be used to simulate future conditions)*

As discussed in Section 1, GE will be required to use the model developed by EPA to evaluate potential remedial alternatives during the CMS. As part of this evaluation, it is likely that the uncertainty of model predictions will need to be considered when differences in simulated future PCB concentrations are compared among various alternatives. At this point, it is premature to define the exact methods that will be used to account for model uncertainty in the CMS. However, the uncertainty approach presented in the MVR cannot be used for the CMS because the results are unrealistic and the computational requirements are too great.

The uncertainty results in the MVR are considered unrealistic for two primary reasons. First, the uncertainty bounds based on the approach presented in the MVR are much wider than the uncertainty indicated by the site data. For example, for largemouth bass at Woods Pond, the average of the data is ~70 ppm, with uncertainty bounds defined by +/- 2 standard errors of the mean (SEM) of about 45 to 85 (MVR Figure 4.3-5). The mean +/- 2SEM provides bounds on what can be considered reasonable model results; that is, the model, to be considered realistic,

should predict fish concentrations within this range. The computed FCM mean PCB concentration, based on the empirical distribution function (EDF) from the EFDC Kolmogorov-Smirnov (KS) analysis, is 83.8 ppm (MVR Table 5.2-14). This is reasonably close to the mean of the data. However, the means based on the left and right KS uncertainty bounds are 50 to 210 ppm (MVR Table 5.2-14). The upper end of this range is considerably greater than the upper uncertainty bound on the data (85 ppm) and is therefore not a realistic representation of model uncertainty.

Second, correlations among parameters were not discussed or incorporated in the EFDC or FCM uncertainty analyses. For example, in EFDC, the partition coefficient (KOC) in the water column and sediment would be expected to be related, but there is no relationship in the values tested for the input sets (MVR Attachment 5-1, Table 1). In the FCM, no restriction was placed on the combinations of water and sediment PCB concentrations sampled from the EDFs (or right and left KS bounds). However, a relationship is expected. For the results to be realistic, some evaluation of correlations among parameters should have been incorporated in the uncertainty analysis.

Furthermore, a substantial level of effort was required to complete the uncertainty analyses documented in the MVR. Over 50 long-term simulations with the EFDC model were needed to generate the uncertainty bounds for the KS analysis on the Phase 2 calibration results. Incorporation of this approach in the CMS would therefore require a similar number of runs to generate the uncertainty bounds, for each potential remedial alternative that is simulated. Given that the estimated simulation time required to conduct a single long-term future simulation with the model will be on the order of months (see Section 5.1), this approach is clearly not an option if the CMS is to be completed within a realistic timeframe.

The uncertainty analysis approach presented in the MVR cannot be used to evaluate uncertainty in the model simulations conducted during the CMS because it produces ranges of PCB concentrations that lie far outside of the bounds of the field data and because the computational burden of running numerous EFDC simulations renders that approach infeasible.

SECTION 5
EFDC COMPUTATIONAL ISSUES

MVR Charge Reference:

- *Question 7 (model's ability to be used to simulate future conditions)*

5.1   MODEL SIMULATION TIME

Assessment of remedial alternatives in the CMS will be based on long-term simulations with EPA's model that project PCB concentrations several decades into the future. Based on the model simulation time cited in the MCR (i.e., 40 hours for 1.33 years) (see MCR, Page 7-15), it would take 50 to 90 days of computation time to complete a single long-term simulation of PCB fate that projects 40 to 70 years into the future. More recent model execution statistics provided by EPA indicate that run times of approximately 10 to 19 hours per year are possible, depending on the hydrograph for a given year and the type of computer system used (Garland 2006). Thus, computation time is still on the order of 25 to 44 days for a single 40 to 70 year projection (assuming an average of 15 hours/year run time) with the model. The CMS will necessarily require numerous runs to fully evaluate a variety of remedial options. Moreover, based on past experience, it is oftentimes necessary to conduct multiple runs to fully evaluate a single remedial scenario, since testing and sensitivity analysis are needed to verify model results and evaluate the assumptions used to represent future conditions. Therefore, the model's current simulation times will not allow the CMS Report to be submitted within 180 days after EPA approval of the CMS Proposal (which is the default timeframe specified in the Reissued RCRA Permit). Hence, an alternative schedule will need to be proposed in the CMS Proposal.

Based upon review of the MVR, it appears that no substantial changes to the EFDC model framework or approach have been implemented to further address the run time issue. In the MCR-RS (Response to General Issue 3), EPA listed a number of methods that have been implemented to produce improvements in EFDC's run time, including: 1) utilization of both dynamic and split time steps; 2) bypassing sections of the model grid that are changing slowly

(or not at all) over time; and 3) conducting simulations for selected portions of the calibration period like high flow events (see MCR-RS Page 7). However, while implementation of these methods has contributed in part to reducing model run time, the run time required for a single projection is still intractable for efficient conduct of the CMS. Moreover, EPA discounted, with limited discussion but no model testing, other ideas presented by the Peer Review Panel and GE that could be used to improve EFDC's computational efficiency (e.g., separating hydrodynamic, sediment transport, and PCB fate simulations, and use of alternative grid approaches; see MCR-RS Pages 6 through 8). Regardless of the improvements that have been implemented by EPA, run times will still be on the order of months to complete even a single long-term simulation.

Simulation times must be of reasonable duration in order to use the model for its intended purpose of evaluating alternative remedial scenarios. The simulation time for EFDC is too long to efficiently evaluate long-term simulations of remedial alternatives during the CMS.

5.2 POTENTIAL MODEL INSTABILITIES

Complex simulation models, such as those developed for the Housatonic River, can produce erratic results that are inconsistent with local model trajectories or fail due to numerical instabilities. In some cases, such model behavior is transitory and of little or no consequence to the model predictions. In other cases, they are symptoms of a larger problem with the model. The fact that GE will be required to continuously run the models for one to two months for each simulation of 40 to 70 years magnifies the potential for failure. Against this background, there are two instances documented in the MVR that raise some concerns about the behavior of EFDC:

- First, of the 55 EFDC simulations developed for the KS analysis of uncertainty, four simulations failed for "unknown" reasons (MVR Page 5-26). More discussion or exploration into the reasons for this failure is warranted, as it may be indicative of a larger problem in the model. Is the failure repeatable? Is it a function of the parameters tested and the model becoming unstable? If so, was it hydrodynamics, sediment transport, or PCB fate?

- Second, there appears to be some instability in the flow rates predicted by the hydrodynamic model during low flow periods. For example, flows at New Lenox Road in 1980 are very low, highly variable, and in fact appear to go negative (MVR Figure 6.2-3). Similar oscillations are noted in the West Branch flow and stage height for many years (MVR Figure 6.2-3) and in the flows at Holmes Road for several years between 1992 and 2003 (e.g., MVR Figure 6.2-19). Such model behavior suggests that there may be issues with hydrodynamic model stability at low flows. Additional evaluation or discussion of these results is warranted.

There are some indications that the EFDC model may not be computationally stable; additional evaluation is needed to assess that issue.

SECTION 6
EXAMPLE MODEL SCENARIOS

MVR Charge Reference:

- ***Question 6 (reasonableness of example scenarios)***

In Section 7 of the MVR, examples are provided to demonstrate how the model would respond when simulating potential remedial options. However, the MVR's description and setup of these demonstration runs are insufficient to evaluate how the model will perform during the long-term simulations that will need to be conducted by GE during the CMS.

To allow for a complete evaluation of model performance during long-term future simulations, the example remedial scenario simulations should have been set up to more closely follow how the model will be used in the CMS – i.e., model simulations that project forward from the end of the validation period, utilizing sediment bed properties and PCB concentrations from the end of the validation period). The model demonstration runs presented in the MVR do not appear to have been configured in this manner. Rather, it appears that initial sediment conditions (i.e., PCB concentrations, grain size distribution, and bed elevations) were set to be the same as those used at the beginning of the Phase 1 calibration, based on a comparison of spatial plots from the MCR (Figure 7-2) and MVR (Figure 6.2-51). As stated above, it would have been more appropriate to start the model with the bed elevations, grain size distributions, and sediment PCB concentrations predicted at the end of the validation period, thereby treating the model demonstration runs as more representative future projections. If the cumulative changes that occurred in the simulated sediment bed during the 26-year validation period are not incorporated in the initial conditions of EPA's model demonstration runs, then the long-term response of the model presented in the MVR may be a model artifact.

Furthermore, it is unclear why the model predictions were not run through FCM. An assessment of results from FCM using exposures from the EFDC demonstration runs is needed to fully evaluate how the model behaves under conditions that are different from the calibration and validation periods. This is especially important since there have been no model sensitivity

tests conducted with FCM to evaluate the relative importance of benthic versus water column food sources as sources of PCBs to the food web.

Because GE will need to use the model to evaluate remedial scenarios during the CMS, it is critical that the MVR provide a good indication of how the model will behave during long-term future simulations. The example scenarios presented in the MVR do not provide that information because they do not project forward from the end of the validation period and because they do not include FCM results.

SECTION 7
ADDITIONAL INFORMATION NEEDED TO FULLY ASSESS THE MODELS

Upon review of the MVR, GE has identified several aspects of the modeling for which results are lacking or not presented with sufficient detail to allow a complete evaluation of the model's performance. First, additional comparisons of the Phase 2 calibration and validation results to data are required to assess the model's ability to predict bank erosion, low flow water column PCB spatial patterns, and floodplain soil PCB concentrations. Second, the calibration and validation of the upstream and downstream models, as presented in the MVR, are incomplete because the necessary model-data comparisons have not been conducted.

7.1 PHASE 2 CALIBRATION/VALIDATION RESULTS

MVR Charge References:
- *Question 2 (sufficiency of model-data comparisons)*
- *Question 7 (model's ability to be used to simulate future conditions)*

7.1.1 No Model-Data Comparisons of Bank Erosion

As discussed in Section 2.1 of these comments, the empirical approach used by EPA to simulate bank erosion provides estimates of solids loads due to bank erosion on an annual basis for the model. However, the bank erosion rates computed by the model should have been compared to bank erosion measurements made by EPA. Two specific field studies conducted by EPA provide measurements of short term bank erosion rates: toe pins were installed at five locations in Reach 5 and monitored between 2000 and 2002; and detailed surveys of 15 meander bends in Reach 5 were conducted in November 2001 and June 2002 (see Section 8.8.1.9 of the RFI Report, which is included as Attachment 1). These data provide an important constraint on the bank erosion model, and therefore should have been compared with the model predictions at these locations.

7.1.2 Limited Model-Data Comparisons for Low Flow Water Column PCB Spatial Patterns

MVR Figures 6.2-45 and 6.2-46 show model-data comparisons for low flow (i.e., Coltsville flow between 14 and 29 cfs) and moderate flow (i.e., Coltsville flow between 44 and 75 cfs) water column PCBs for the Phase 2 calibration period. For these charts, several sampling events were averaged, but nearly all are from a very limited timeframe (e.g., most of the data included in the low flow average were collected in June 1999). Based on Table 4.2-8, it appears that only water column data from 1999 and 2000 were included in the data averages shown on the charts. However, there is a substantial set of low flow routine monitoring data collected prior to 1999 that were not included in these assessments (e.g., see MVR Table 4.2-7). A more robust evaluation of the model's ability to predict spatial patterns in low flow PCBs would be to include data from several years and sampling seasons.

7.1.3 No Model-Data Comparisons of Floodplain PCB Temporal Trends

As stated in the MVR (page 6-65), EPA utilized floodplain initial conditions developed for the Phase 1 and Phase 2 calibration (i.e., based on data from 1998-99) for model validation. This was done based on the assertion that there is less variability in floodplain soil PCBs, and it thus implicitly assumed that little change in floodplain PCBs would occur over the 26 year validation period. However, some large changes in floodplain surface soil PCB concentrations are predicted by the model. For example, the model predicts a greater than 50% increase in the surficial 6-inch PCB concentration in several areas of the floodplain over the validation period (MVR Figure 6.2-55). Such significant predicted changes are contradicted by the underlying assumption that little change in floodplain PCBs would occur over the 26-year validation period. However, EPA did not provide any model-data comparisons to evaluate the predicted changes. At a minimum, EPA should have compared the model results at the end of the validation period with the 1998-1999 EPA floodplain data (the same data used to develop floodplain initial conditions) to assess whether changes predicted by the model produce concentrations that are consistent with the data. Furthermore, EPA should have provided additional justification for this approach by comparing model-predicted changes in PCB concentrations with historical data in areas of the floodplain having sufficient data. A substantial amount of data was collected in

some areas of the floodplain during the early- to mid-1990s that would allow for this type of an evaluation.

The documentation of the modeling is incomplete in some cases. Additional modeling results are needed to allow a full evaluation of the Phase 2 calibration and validation.

7.2   UPSTREAM MODEL

MVR Charge Reference:
* *Question 2 (sufficiency of model-data comparisons)*

Section 8 of the MVR describes the development of an EFDC model of the East Branch, which extends approximately two miles upstream to Newell Street Bridge. EPA states in the MVR (Page 8-1) that the purpose for developing this upstream model was to construct and test a revised upstream boundary model that would be representative of the upstream area, for use in simulating future conditions with the PSA model.

The upstream model, as described in the MVR, is largely incomplete. Simulations of hydrodynamics and sediment transport were run over the 26-year validation period. However, model-data comparisons were limited to simple comparisons of model-predicted TSS with data from one "interior location" (the station name is not given) for one year (2002-2003). Although TSS within this reach may be impacted by the ongoing remediation, comparison of the model results for additional locations and years is necessary. Furthermore, quantitative comparisons of model and data, similar to those performed for the PSA model, are needed to fully evaluate the upstream model results.

In addition, PCB fate and transport were not simulated by EPA with the upstream model; the MVR states (Page 8-1) that this was due to the "lack of suitable data in the downstream portion of this reach of the river." However, water column PCB data are available at the same

spatial and temporal resolution as TSS for this reach of the river. Thus, at a minimum, model-data comparisons of PCBs should have been made over the one-year timeframe used for TSS. Similar to TSS, PCB results may have been impacted by the ongoing remediation. Nonetheless, comparisons of model results for the PCB data set should have been made. By not simulating PCB fate and transport, an important test of the upstream model was not completed.

While GE appreciates the fact that ongoing remediation hinders development of the upstream model, incorporation of this model in the MVR is premature given that substantial additional development efforts will be required before this model could be used during the CMS.

The upstream model, as presented in the MVR, is incomplete and cannot be considered fully validated given that PCB fate and transport were not simulated and the model-data comparisons are insufficient.

7.3 DOWNSTREAM (REACH 7-8) MODEL

MVR Charge Reference:
- *Question 2 (sufficiency of model-data comparisons)*

EPA has extended its model domain approximately 19 miles downstream to Rising Pond Dam, which will provide the ability to evaluate the downstream impacts of potential remedial action scenarios during the CMS. However, the downstream model, as developed and presented in the MVR, is largely incomplete and cannot be considered a validated model. First, the entirety of the downstream EFDC discussion presented in the MVR (Section 6.4) focuses on parameterization of the model in these reaches and does present any comparisons of model results with site-specific data (i.e., no model calibration). The only model results presented in the MVR are the PCB concentrations predicted by EFDC that were input to FCM for a two-year period (1997-98; MVR Figures 6.4.14 and 6.4.15), with no comparison to the available data. Additional information is thus required to assess the ability of the downstream model to

reasonably simulate hydrodynamic, sediment transport, and PCB fate processes simulated by EFDC in these reaches.

In the MVR, EPA states that the downstream EFDC model validation period was restricted to 1997 and 1998 because fewer data are available in Reaches 7 and 8. There are, however, several available data sets that were not utilized by EPA to demonstrate the accuracy and reliability of the downstream model.

- *Routine water column PCB and TSS data at Division Street* – Division Street Bridge is located in Great Barrington, less than one mile downstream of Rising Pond Dam. While this monitoring station is located downstream of the extended model domain, it is reasonable to use as a calibration point. Furthermore, a relatively extensive data set exists at this location over the 26-year model validation period (see Table 7-1). These data should thus be compared with model predictions of TSS and PCBs passing over Rising Pond Dam.

Table 7-1. Summary of Samples Collected at Division Street Bridge

Year	Sample Count		Program
	PCB	TSS	
1982	26	13	Housatonic River Study, 1980 and 1982 Invest.
1989	10	5	1990 MCP Phase II
1990	14	9	1990 MCP Phase II
1991	18	18	1990 MCP Phase II
1991	20	39	LMS Fate and Transport Model
1992	48	35	LMS Fate and Transport Model
1993	16	8	LMS Fate and Transport Model
1995	4	2	1994 and 1995 MCP Supp. Phase II/RFI
1996	21	10	Monthly Water Column Monitoring
1997	14	12	Monthly Water Column Monitoring
1998	20	20	Monthly Water Column Monitoring
1999	7	7	Monthly Water Column Monitoring
2000	12	12	Monthly Water Column Monitoring
2001	12	12	Monthly Water Column Monitoring
2002	12	12	Monthly Water Column Monitoring
2003	12	12	Monthly Water Column Monitoring
2004	12	12	Monthly Water Column Monitoring
2005	12	12	Monthly Water Column Monitoring

Data Source: GE Housatonic River Database, March 2006 release.

- *USGS Sediment Loading Data* – Between April 1994 and March 1996, USGS conducted an extensive study of suspended sediment characteristics in the Housatonic River Basin (USGS 2000). Daily sampling for TSS was conducted at Division Street in Great Barrington during this study. These data thus provide an additional constraint on the downstream model's sediment transport predictions and should have been included in model-data comparisons in the MVR.

- *Rising Pond High-Resolution Sediment Cores* – As described in the RFI Report, two finely segmented sediment cores were collected in 1998 from Rising Pond and analyzed for PCBs and the radioisotope Cesium-137 (BBL and QEA 2003, Section 4.5.4; see Attachment 4 to these comments). Although limited in number, these cores provide additional calibration data for the downstream model. First, the radioisotope data provide estimates of net sediment deposition rates that should be compared with results from the sediment transport model. Second, pairing of sediment radioisotope dating with vertical patterns in PCB concentrations from these cores provide a means of assessing the PCB fate model's ability to reasonably simulate temporal trends in the PCB concentration on depositing particles within Rising Pond.

- *Reaches 7 and 8 Historic Sediment Data* – Historically, numerous sediment cores have been collected from Reaches 7 and 8 that could be used to evaluate temporal changes in sediment concentrations in this downstream reach. For example, approximately 50 locations were sampled in Reaches 7 and 8 in 1980 to 1982; nearly 20 of these locations were in Rising Pond. Further, nearly 10 cores were collected from Rising Pond in 1990. These data are presented in Section 4 and Appendix B of the RFI Report. While these historical data sets are less robust than those from the PSA, they do provide additional information that should have been used to calibrate the downstream model.

The downstream model, as presented in the MVR, is incomplete and cannot be considered fully validated since model results were not compared against available data sets for TSS, water column PCBs, and sediment PCBs.

SECTION 8
SUMMARY

Upon review of the MVR, it is clear that EPA and its contractors have put a substantial effort into the modeling project over the last year. Changes were made to the modeling framework and approach in response to the MCR peer review, calibration over a 10½-year period was completed, sensitivity and uncertainty analyses were conducted based on that calibration, validation over a 26-year period was conducted, long-term simulations of example future scenarios were completed, and models of sections of the river upstream and downstream of the PSA were developed to extend the modeled domain. In general, it appears that a credible effort has been made to improve the model. However, because GE is required to use the model developed by the EPA during the CMS to evaluate potential remedial alternatives, a thorough scrutiny of the model framework and its results, and a complete evaluation of its performance must be afforded during the validation phase and its associated peer review. Based on GE's review of the MVR, we have a number of concerns in this regard:

- First, there are some problems with the modeling framework and approach. The formulation used to represent bank erosion is not consistent with the accepted conceptual model of that process, and the methods used to develop sediment initial conditions do not provide a robust test of the model's ability to simulate sediment PCB concentrations over long time scales.

- Second, there are potential biases evident in the model predictions of low flow TSS, low flow water column PCB, and surface sediment PCB concentrations. These biases, coupled with the model's inability to match low flow spatial patterns in PCBs at Woods Pond and its apparent insensitivity to pore water diffusion parameters, indicate the that relative importance of external versus internal PCB sources, as well as fate processes during low flows, may not be properly represented by the model. These biases also can result in incorrect predictions by the FCM of the relative importance of water column-versus sediment-derived sources of PCBs to the fish.

- Third, the model results and comparisons to data provided in the MVR are not sufficient to support a full assessment of the model's ability to predict temporal trends in sediment PCBs, bank erosion, low flow water column PCB spatial patterns, and floodplain soil PCB concentrations. In addition, the upstream and downstream models, as documented in the MVR, are incomplete and cannot be considered validated because the necessary comparisons to the available site data have not been completed.

- Fourth, the approach developed for the MVR to quantify model uncertainty is not useful for assessing uncertainty in the modeling to be performed by GE during the CMS because the uncertainty bounds in the MVR approach are unrealistically large and that approach is computationally infeasible.

- Finally, there are computational issues with EFDC that will preclude efficient use of this model during the CMS. The model simulation time is too long, as the time required to complete just one simulation of a future remedial scenario several decades into the future will be one to two months. This will require a considerably longer time to perform the CMS than the 180-day default timeframe specified in the Reissued RCRA Permit. Additionally, the model results presented in the MVR indicate that there are potential instabilities with EFDC that may cause problems when that model is used to make future simulations.

Overall, unless these issues are addressed with proper detail during the model validation phase, including the peer review, it is likely that the model delivered to GE will have significant limitations and problems. GE may not be able to fully evaluate the extent of those issues until it begins working with the model to assess potential remedial alternatives during the CMS.

SECTION 9
REFERENCES

Alonso, C.V. and S.T. Combs, 1990. Streambank erosion due to bed degradation – a model concept. *Transactions of ASAE* 33(4):1239-1249.

Blasland, Bouck, and Lee, Inc. and Quantitative Environmental Analysis, LLC, 2003. *Housatonic River, Rest of River, RCRA Facility Investigation*. Prepared on behalf of the General Electric Company, Pittsfield, MA. September 2003.

Garland, E., 2006. Housatonic Model Requirements. E-mail message from E. Garland (HydroQual, Inc.) to S. Campbell (Weston Solutions) and K. Mooney (GE), April 10, 2006.

Millar, RG and Quick, MC, 1998. Stable width and depth of gravel-bed rivers with cohesive banks. *ASCE J. Hydr. Engr.* 124(10):1005-1013.

Osman, AM and Thorne, CR, 1988. Riverbank stability analysis I: theory. *ASCE J. Hydr.Engr.* 114(2):134-150.

USGS, 2000. *Suspended-Sediment Characteristics in the Housatonic River Basin, Western Massachusetts and Parts of Eastern New York and Northwestern Connecticut, 1994-96*. Water-Resources Investigations Report 00-4059, Northborough, Massachusetts, 2000.

Weston, 2000a. *Modeling Framework Design, Modeling Study of PCB Contamination in the Housatonic River*. Prepared by R.F. Weston, Inc. and Aqua Terra Consultants for the U.S. Environmental Protection Agency, Region I and U.S. Army Corps of Engineers, New England District. October 2000.

Weston, 2000b. *Quality Assurance Project Plan, Modeling Study of PCB Contamination in the Housatonic River*. Prepared by R.F. Weston, Inc. and Aqua Terra Consultants for the U.S. Environmental Protection Agency, Region I and U.S. Army Corps of Engineers, New England District. October 2000.

Weston, 2004a. *Model Calibration: Modeling Study of PCB Contamination in the Housatonic River*. Prepared for the U.S. Environmental Protection Agency, Region I, and the U.S. Army Corps of Engineers. December 2004.

Weston, 2004b. *Modeling Framework Design: Modeling Study of PCB Contamination in the Housatonic River*. Prepared for the U.S. Environmental Protection Agency, Region I, and the U.S. Army Corps of Engineers. April 2004.

Weston, 2006a. *Model Validation: Modeling Study of PCB Contamination in the Housatonic River*. Prepared for the U.S. Environmental Protection Agency, Region I, and the U.S. Army Corps of Engineers. March 2006.

Weston, 2006b. *Responsiveness Summary to the Peer Review of Model Calibration: Modeling Study of PCB Contamination in the Housatonic River*. Prepared for the U.S. Environmental Protection Agency, Region I, and the U.S. Army Corps of Engineers. January 2006.

Attachment 1
Citations
(Millar and Quick 1998; Alonso and Combs 1990; and
Osman and Thorne 1988)

Stable Width and Depth of Gravel-Bed Rivers with Cohesive Banks

By Robert G. Millar[1] and Michael C. Quick,[2] Member, ASCE

ABSTRACT: An analytical model is developed to determine the influence of the bank stability on the stable width and depth of alluvial gravel-bed rivers with cohesive banks. The formulation of the model is based on the assumption that the stable width corresponds with an optimum condition that is equivalent to the maximum bed load transporting capacity. The optimum condition develops when the channel banks are at their limiting stability with respect to either mass failure or fluvial erosion. Two basic channel types are identified: bank-height and bank-shear constrained. Mass failure stability is estimated using a simple total stress approach. A method for estimating the critical bank shear stress based on model calibration is proposed. Analysis of field data indicates that the effect of the bank vegetation on bank stability can be expressed in terms of the critical bank shear stress. The average critical bank shear stress value calculated for riverbanks covered by vegetation with well-developed root networks was found to be approximately three times that obtained from rivers with weakly vegetated, grass-covered banks.

INTRODUCTION

Despite receiving considerable attention this century, there is still no consensus to explain or predict the stable width of alluvial channels. It is widely recognized that bank stability represents an important constraint on the development of river geometry, and that rivers with erodible banks are typically wider and shallower than those with more resistive banks. Furthermore, changes in the bank erodibility, including removal of the bank vegetation, can result in destabilization of the banks, and can cause widening and instability in the river channel. There have been relatively few rationally based approaches that predict the effect of changes in the bank stability on the stable channel width. Previous efforts have been largely confined to rivers with noncohesive banks. These include lateral momentum transfer models (Parker 1978; Ikeda and Izumi 1990; Pizzuto 1990; Vigilar and Diplas 1997) and the steady-state optimization or "extremal" models (Millar and Quick 1993). There have been considerably fewer studies dealing with rivers with cohesive banks. Dynamic channel models formulated for cohesive banks, such as those of Osman and Thorne (1988) and Darby and Thorne (1996b), have been used to determine the steady-state geometry by allowing them to run until the transient adjustments become negligible.

The basic goal of the present study has been to quantify the effect that bank stability has on the stable width and depth of natural gravel rivers with cohesive banks. The term "stable" used herein refers to a channel with stable banks, but it may have mobile beds. This differs from the original definition that referred to threshold channels, for which sediment on the bed and banks was below the threshold for motion (Lane 1955).

In the present paper, a steady-state optimization or "extremal" model developed by Millar and Quick (1993) for noncohesive banks has been reformulated for application to rivers with cohesive banks. This approach is based on earlier extremal models by Chang (1980) and White et al. (1982), which did not explicitly account for the effect of bank stability.

[1]Asst. Prof., Dept. of Civ. Engrg., Univ. of British Columbia, Vancouver, BC, Canada, V6T 1Z4.

[2]Prof., Dept. of Civ. Engrg., Univ. of British Columbia, Vancouver, BC, Canada, V6T 1Z4.

OBJECTIVES

The principal objectives of the present study are to

- Represent bank erosion mechanisms in terms of simplified processes that can be incorporated into the optimization model
- Investigate how the bank stability constrains the development of a stable channel width
- Undertake preliminary testing of the approach using published field data
- Quantify the effects of bank vegetation on the critical bank shear stress

EROSION MECHANISMS

Broadly speaking, the principal erosion mechanisms that operate on cohesive riverbanks can be considered in terms of two distinct processes: mass failure and fluvial entrainment (Thorne 1982; Stevens 1989). Mass failure refers to the slumping or collapse of sections of the riverbank when the critical height for stability has been exceeded. Fluvial entrainment refers to the removal of individual grains or aggregates by the shearing action of the flow. Within these two broad categories are a number of subtypes or complementary processes—including soil piping and sapping (Ullrich et al. 1986; Hagerty 1991) for mass failure; and frost heave and desiccation cracking, which can influence subsequent fluvial erosion (Lawler 1992).

The intent of the bank stability analysis developed herein is to determine the limiting condition when the banks are just stable with respect to mass failure and/or fluvial erosion. The bank stability will be considered only in terms of sliding along a simple curved failure surface, and by fluvial erosion through direct removal of cohesive grains and particles by the flow. Mass failure stability will be estimated using the "$\phi = 0$" stability curve from Taylor (1948), which is described in the following section. This probably represents the simplest approach for routine stability analysis of homogeneous cohesive riverbanks that are subject to flood inundation and rapid drawdown, or saturation during prolonged rainfall or snowmelt. Stability with respect to fluvial erosion will be characterized in terms of a critical bank shear stress that must be exceeded before fluvial erosion of the banks occurs.

It will be argued that rivers with cohesive banks can be characterized either as bank-height or bank-shear constrained. Bank-height constrained channels have banks that are subject to erosion principally through mass failure, while the banks of bank-shear constrained channels are eroded principally through fluvial erosion processes.

Mass Failure

The mass failure stability of cohesive riverbanks can be estimated using a variety of methods developed for slope-stability analysis. The most commonly used methods are the various limit equilibrium methods that include analytical solutions for planar failure [e.g., Lohnes and Handy (1968)], the slip-circle method (Taylor 1948), and the various methods of slices [e.g., Bishop (1955)]. The primary difference between riverbanks and other hillslopes is that riverbanks are typically inundated by floodwaters periodically, and the limiting bank stability usually occurs during subsequent drawdown when bank strength is reduced due to increased unit weight of the soil, and by the development of excess pore-water pressures (Darby and Thorne 1996a).

In the present paper, mass failure stability of cohesive riverbanks will be analyzed on a total stress basis assuming saturated, undrained conditions at the time of failure. The advantages of a total stress analysis over one based on effective stress are twofold: (1) In a total stress analysis, pore-water pressures do not need to be accounted for directly; and (2) measurement of undrained soil strength in terms of total stress is generally easier and less costly than soil parameters in terms of effective stress.

The following is a brief summary of some fundamental soil mechanics principles relating to mass failure processes, and is presented to provide some background to the subsequent mass failure analysis. This material can generally be found in standard soil mechanics textbooks [e.g., Spangler and Handy (1982); Atkinson (1993)].

According to Mohr-Coulomb theory, the shearing strength of soil can be represented by

$$s = c + \sigma \tan \phi \tag{1}$$

where s = shear strength (kPa); c = cohesion (kPa); σ = total stress (kPa); and ϕ = friction angle (°). Mass failure analyses can be undertaken on either a total stress or an effective stress basis. The effective stress, σ'(kPa), is defined as the total stress minus the pore-water pressure

$$\sigma' = \sigma - u \tag{2}$$

where u = pore-water pressure (kPa). Values of c and ϕ are determined experimentally and will have different values depending upon the type of test, and whether the values are defined in terms of σ or σ'.

Total stress analyses are based on the undrained shear strength. The difference between drained and undrained conditions is illustrated in Fig. 1. Initially the water level in the river is close to bank-full and the riverbank is fully saturated [Fig. 1(a)]. The banks are stable because of the supporting hydrostatic forces from the water in the channel. For undrained conditions following drawdown [Fig. 1(b)], the phreatic surface remains essentially horizontal, and the pore-water pressure distribution within the bank would be hydrostatic. For drained conditions, the phreatic surface will have responded to drawdown of the free water surface, and ground-water flow into the channel will have been established. The pore-water pressure distribution within the bank would not be hydrostatic. Perfectly undrained conditions [Fig. 1(b)] are unlikely to be fully developed in a natural river. However, if drawdown of the free water surface is sufficiently rapid relative to the establishment of ground-water flow within the bank, then conditions along the incipient failure surface within the bank would be essentially undrained. In any case, the undrained bank stability represents the limiting, worst-case condition.

The undrained shear strength is independent of σ. During undrained testing of a saturated sample, σ' remains constant despite changes in σ, because any increase in σ is taken up
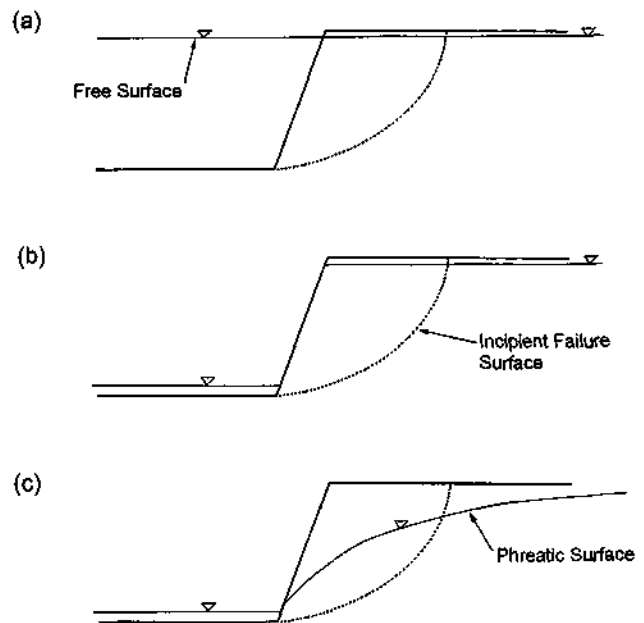
FIG. 1. Schematic Illustration of Drained and Undrained Conditions: (a) Submerged Bank during Near Bank-Full Flow; (b) Undrained Conditions Following Rapid Drawdown; (c) Drained Conditions (Ground-Water Flow Established into River)

as an increase in u. This results in the so-called $\phi = 0$ analysis—which is somewhat confusing, in that it does not actually mean that the soil is frictionless, but rather indicates that the undrained soil strength is independent of the applied total stress, σ. The undrained shear strength of saturated soil can therefore be represented in terms of total stress by the undrained cohesion, c_u, with $\phi = 0$ (Spangler and Handy 1982, page 433; Atkinson 1993, page 108).

Factor of Safety

A factor of safety with respect to height, FS_H, is defined as

$$FS_H = \frac{H_{crit}}{H} = \frac{N_s c_u}{H \gamma_t} \tag{3}$$

where H = vertical bank height (m); H_{crit} = maximum stable or critical bank height (m); γ_t = saturated unit weight of soil (kN/m³); and N_s = dimensionless stability number. Banks are considered to be at the limiting stability with respect to mass failure when $FS_H = 1.0$, and unstable when $FS_H < 1.0$.

Stability Curves

For slopes of simple geometry composed of homogeneous soil, existing solutions for N_s for the undrained $\phi = 0$ case may be used for the routine assessment of bank stability. The variation of N_s with the bank angle, ϕ (°), can be presented as a stability curve. The $\phi = 0$ stability curve for toe failures is shown in Fig. 2 [after Taylor (1948)]. Over the range $15° \le \theta \le 90°$, the variation of N_s can be closely approximated by the following equation (Fig. 2):

$$N_s = 3.83 + 0.052(90 - \theta) - 0.0001(90 - \theta)^2 \tag{4}$$

For any combination of H, θ, γ_t, and c_u, FS_H can be readily determined using (3) and (4).

The $\phi = 0$ stability analysis (Taylor 1948) was developed for slopes composed of homogeneous soil. For stratified banks with varying soil properties, "average" or representative values of c_u and γ_t need to be estimated. This may be difficult in practice, especially when stability is influenced by a weak layer within the bank, or when other mechanisms such as soil
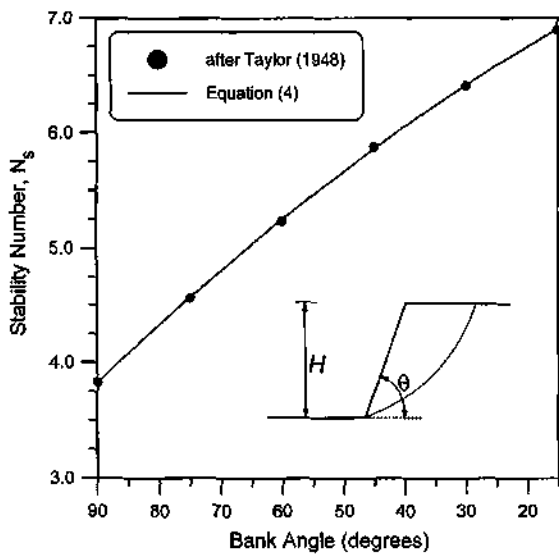
FIG. 2. $\phi = 0$ Stability Curve after Taylor (1948)

FIG. 3. Definition Sketch

piping are important. However, in the context of the present analysis, values for c_u and γ, averaged from a number of locations along a reach will be assumed to be representative. Undrained cohesion, c_u, can be estimated using a number of tests such as the unconfined compression test, or can be estimated directly in the field using a vane shear test.

Fluvial Erosion

The driving force during fluvial erosion is the shearing action of the fluid on the bank sediment. The resultant interparticle force for cohesive sediment is the net result of several forces of attraction and repulsion. These forces result from complex electrochemical processes, which include the clay mineralogy and content, and the temperature and chemistry of the pore and eroding fluids (Arulanandan et al. 1980; Grissinger 1982; Raudkivi 1990). Compared to mass failure stability analysis, which can be considered a relatively mature discipline, the mechanics of fluvial erosion of cohesive sediment are poorly understood.

The stability of the channel banks can be expressed in terms of a factor of safety with respect to bank shear, FS_τ

$$FS_\tau = \frac{\tau_{crit}}{\tau_{bank}} \quad (5)$$

where τ_{bank} = mean bank shear stress (kPa); and τ_{crit} = critical bank shear stress for bank sediment (kPa). Banks are considered to be at the limiting stability with respect to fluvial erosion when $FS_\tau = 1.0$, and unstable when $FS_\tau < 1.0$.

In practice, direct measurement of τ_{crit} is difficult, and its value may vary over time due to desiccation cracking and freeze-thaw activity (Lawler 1992). At present, there are no well-established methods for directly measuring τ_{crit}. Direct measurement of τ_{crit} using a rotating cylinder technique (Moore and Masch 1962; Chapuis and Gatien 1986) probably represents the most promising approach, although it may be difficult to obtain representative samples that replicate field conditions in the laboratory. An alternative approach will be presented, in which the current model can be calibrated to the observed channel geometry and used to obtain an indirect estimate of τ_{crit}.

OPTIMIZATION MODEL FORMULATION

The preceding bank stability criteria, (3) and (5), have been incorporated into an optimization model similar to that dev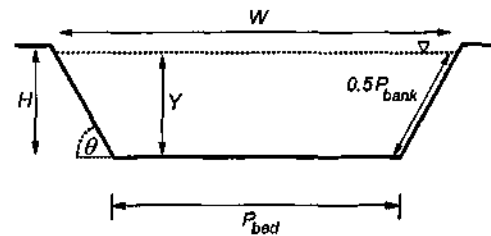eloped by Millar and Quick (1993) for noncohesive banks. To facilitate the modeling procedure, the natural river channel will be represented by a simplified trapezoidal cross-sectional geometry of average dimensions (Fig. 3). The banks are assumed to be composed of homogeneous cohesive soil, while the bed is composed of mobile noncohesive alluvial sediment. Strong, bend-induced secondary currents have not yet been included in the analysis. The various components of the model, to be discussed later, include the independent and dependent variables, objective function, and constraints on the channel system.

For clarity, the optimization model is developed in a somewhat simplified form, whereby the channel slope is assumed to be fixed, and is treated as an independent variable. This slope constraint is not strictly necessary and was not used in an earlier study (Millar and Quick 1993). However, the added complexity of allowing the slope to vary tends to obscure the main thrust of the present work, which is to determine the bank stability influence on channel width and depth.

Independent Variables

Independent variables with specified values include the bank-full discharge Q_{bf}, channel slope S, median grain diameter of the bed sediment D_{50}, channel roughness height k_s, undrained bank cohesion c_u, saturated unit weight of bank material γ_t, and critical shear stress for the bank soil τ_{crit}.

Dependent Variables

The following dependent variables will be estimated from the analysis: bed perimeter P_{bed}, bank perimeter P_{bank}, and bank angle θ (Fig. 3). From these primary variables, the secondary dependent variables, such as the friction factor f, mean velocity U, hydraulic radius R_h, surface width W, bank-full flow depth Y, average flow depth $\bar{Y}$, and vertical bank height H, can be determined.

Objective Function: Optimum Solution

The objective function, or "extremal hypothesis," is the maximum bed load transport capacity (White et al. 1982). For a specified slope, the channel will adjust its cross-sectional geometry such that its capacity to transport bed load sediment is a maximum. The geometry corresponding to this maximum bed load transport capacity is assumed to represent the optimum solution.

The bed load transport capacity, G_b (kg/s), is defined as

$$G_b = P_{bed} g_b \quad (6)$$

where g_b = bed load transport capacity per unit bed width (kg/s/m).

A bed load transport relation is required. In the present work, the value of g_b will be calculated using the Einstein-Brown relation (Vanoni 1975, page 170)

$$\frac{g_b}{F_1 \rho s \sqrt{(s-1)g D_{50}^3}} = \begin{cases} 2.15 \exp(-0.391/\tau_{D_{50}}^*), & \tau_{D_{50}}^* < 0.093 \\ 40 \tau_{D_{50}}^{*3}, & \tau_{D_{50}}^* \geq 0.093 \end{cases} \quad (7)$$

where ρ = density of water (kg/m³); s = specific gravity of sediment; g = gravitational acceleration (m/s²); $\tau_{D_{50}}^*$ = dimen-

Reach number (1)	River (2)	Q (m³/s) (3)	W_{obs} (m) (4)	H_{obs} (m) (5)	S (6)	k_s (m) (7)	D_{50} (m) (8)	γ_f^* (kN/m³) (9)	c_u (kPa) (10)	Vegetation type (11)
1	Afor Lwyd	64	17.4	1.78	0.0044	1.09	0.075	20.0	19.8	T
2	Alwen 1-5	10	14.0	0.73	0.0064	1.42	0.106	20.0	12.8	G
3	Alwen 5-9	10.7	9.8	0.73	0.0130	1.25	0.113	20.0	11.6	T
4	Arrow	29.5	13.7	1.34	0.0045	1.16	0.041	20.0	25.7	T
5	Ceirog 1-3	66	17.6	1.79	0.0048	1.21	0.071	20.0	11.7	T
6	Ceirog 4-7	66	19.0	1.36	0.0105	1.07	0.082	20.0	35.5	T
7	Exe	67	31.0	1.77	0.0018	1.35	0.043	20.0	13.1	G
8	Irfon C	81	28.7	1.63	0.0014	0.19	0.055	20.0	15.1	T
9	Otter	14.2	16.7	0.69	0.0032	0.29	0.057	20.0	12.9	G
10	Teign	66	19.0	2.47	0.0014	1.41	0.051	20.0	7.9	T
11	Trent	2.7	5.2	0.65	0.0023	0.56	0.033	20.0	18.4	G
12	Usk	157	39.3	2.64	0.0009	0.60	0.072	20.0	10.7	G
13	Wye	550	59.4	4.19	0.0007	0.28	0.028	20.0	8.0	G
14	Wrye	38	19.5	1.67	0.0020	1.54	0.040	20.0	20.0	G

Note: Data from Charlton et al. (1978). Parameters indicated by * are estimated values; T indicates banks with trees and vegetation that restricts bank erosion; G indicates weakly vegetated or grass-covered banks.

sionless shear stress; and F_1 = parameter related to the fall velocity. For the gravel-bed rivers in the present study, F_1 takes a constant value of about 0.82. The dimensionless shear stress is given by

$$\tau_{D_{50}}^* = \frac{\tau_{bed}}{\rho g(s - 1)D_{50}} \qquad (8)$$

where τ_{bed} is calculated using (12), described next.

Calculation of Bed and Bank Shear Stresses

Values of the average bed and bank shear stresses, τ_{bed} and τ_{bank}, are required to calculate the bed load transport capacity and to determine the stability of the channel banks. An approach developed by Knight (1981) and Knight et al. (1984), as subsequently modified by Flintham and Carling (1988), will be used. This method is based upon an estimate of the proportion of the total shear force that is acting on the channel banks, SF_{bank}, where

$$SF_{bank} = \frac{\tau_{bank} P_{bank}}{\tau P} \qquad (9)$$

and τ = mean channel shear stress; P = total wetted perimeter; and subscript "bank" indicates the bank component. The empirical relation developed from laboratory rectangular and trapezoidal channels is

$$SF_{bank} = 1.77 \left(\frac{P_{bed}}{P_{bank}} + 1.5 \right)^{-1.4} \qquad (10)$$

The values of τ_{bed} and τ_{bank} can be estimated using the following equations:

$$\frac{\tau_{bank}}{\gamma YS} = SF_{bank} \left[\frac{(W + P_{bed})\sin \theta}{4Y} \right] \qquad (11)$$

$$\frac{\tau_{bed}}{\gamma YS} = (1 - SF_{bank}) \left(\frac{W}{2P_{bed}} + 0.5 \right) \qquad (12)$$

CONSTRAINTS

The two principal constraints on the optimum solution are discharge and bank stability.

Discharge Constraint

The discharge constraint ensures that the channel has a discharge capacity equal to the imposed Q_{bf}

$$UA = Q_{bf} \qquad (13)$$

where U = mean velocity; and A = cross-sectional area of the flow. The value of U is obtained from the Darcy-Weisbach equation

$$U = \sqrt{\frac{8gR_h S}{f}} \qquad (14)$$

and the value of the friction factor, f, is calculated using the Keulegan equation

$$\frac{1}{\sqrt{f}} = 2.03 \log \left(\frac{12.2R_h}{k_s} \right) \qquad (15)$$

where k_s = equivalent roughness (m). In the subsequent analysis of field data from Charlton et al. (1978), the values of k_s for each channel have been back-calculated from the given data (Table 1). Otherwise, an independent value of k_s may be estimated from a multiple of a characteristic grain diameter such as 3.5 D_{84} or 6.8 D_{50} (Hey 1979; Bray 1980), where the subscript represents percent finer. The contribution of the bank roughness is not explicitly accounted for in the current model formulation.

Bank Stability Constraint

The bank stability constraint consists of bank-height and bank-shear components that correspond to erosion through mass failure and fluvial erosion, respectively

$$FS_H \geq 1.0 \qquad (16)$$

$$FS_\tau \geq 1.0 \qquad (17)$$

where FS_H and FS_τ are calculated using (3) and (5). Both components of the bank stability constraint must be satisfied for the banks to be considered stable.

Optimization Scheme

The optimum channel geometry is determined using a computer routine that satisfies the constraints in a stepwise fashion until the optimum solution is obtained. A flowchart is shown in Fig. 4. The optimum solution is obtained after the discharge and bank stability constraints have been satisfied, and the solution corresponds to the maximum bed load transporting capacity. The bisectrix method is used to solve each constraint and the objective function. This involves setting initial maximum and minimum bounds on the search region, and evaluating the constraint or objective function at the midpoint between the bounds. Depending on the midpoint value, the midpoint then becomes either the upper or the lower bound
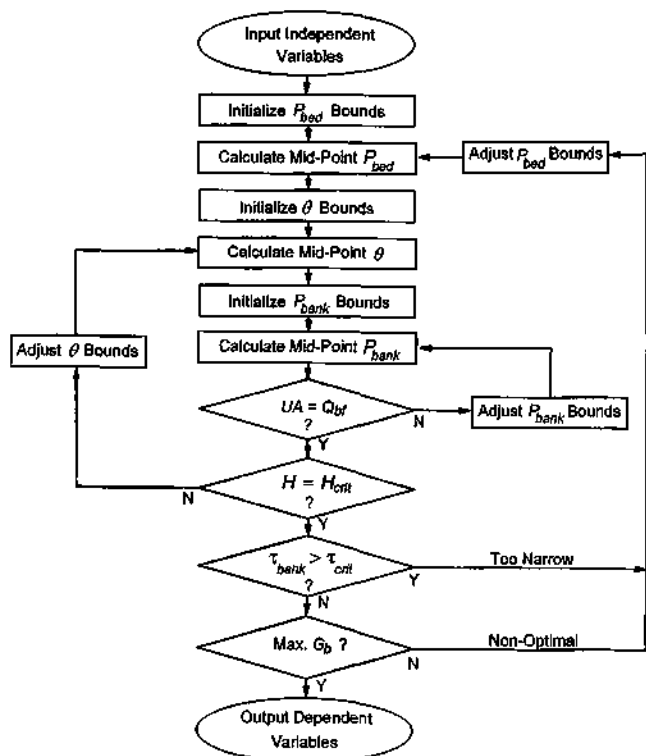
FIG. 4. Flowchart for Optimization Model

for the next stage of the search, reducing the search region by half. This is repeated until convergence is achieved when the difference between the minimum and maximum bounds falls below a preset criterion, typically 0.1% of the midpoint.

In all cases, the optimum has been found to occur at the limiting bank stability when either FS_H or FS_τ—or both—is equal to 1.0. This observation has been used to direct the search for the optimum, by first determining the value of θ where $H = H_{crit}$, and then checking the stability of the banks with respect to fluvial erosion.

The computational procedure is as follows (Fig. 4):

1. Input values of independent variables: Q_{bf}, S, D_{50}, k_s, c_u, γ_s, τ_{crit}.
2. Set minimum and maximum bounds for P_{bed}, θ, and P_{bank}.
3. Determine midpoints for P_{bed}, θ, and P_{bank}.
4. Calculate f and U at the midpoint using (15) and (14), respectively. Adjust P_{bank} bounds until discharge constraint is satisfied ($UA = Q_{bf}$). Update values of f and U for each new midpoint value of P_{bank}.
5. Calculate FS_H using (3) and (4). Adjust θ bounds until midpoint $FS_H = 1.0$ and/or convergence has been attained.
6. Calculate FS_τ using (5). If $FS_\tau < 1.0$, banks are not stable and the channel is too narrow. Reset P_{bed} bounds and go to step 4. Otherwise, banks are stable.
7. Calculate bed load transport capacity using (6) and (7). Does the current value of P_{bed} correspond to the maximum bed load transport? If yes, then the optimum solution has been obtained; output computed values of W, Y, and θ. If no, reset P_{bed} bounds and go to step 3.

Despite the nonlinear nature of the constraints and objective function, the optimum solution has not been found to be influenced by the choice of initial values in the model.

RESULTS

Model testing and data analysis will be undertaken in two stages. First, the proposed mass failure analysis will be tested

independently from the optimization model using field data from Thorne et al. (1981). Second, field data from Charlton et al. (1978) will be used to assess the optimization model, and to examine the influence of bank vegetation on τ_{crit}.

Test of Mass Failure Analysis

In this section, the mass failure stability analysis will be evaluated independently of the optimization model using field data collected by Thorne et al. (1981) for Hotophia Creek, northwest Mississippi. These data form part of the set that was used by Darby and Thorne (1996a) to test their planar failure stability analysis. The Hotophia Creek data set consists of 118 bank cross sections that were surveyed in January 1978, and resurveyed in June 1979. These basic data include bank height, H, and bank angle, θ. Between the two surveys, 41 of the stream banks were observed to be unstable. Soil strength parameters were obtained from the adjacent Johnson and Goodwin Creeks that have similar soil types and bank stratigraphy (Thorne et al. 1981).

Unconfined compression tests were performed on approximately 85 soil samples. Generally, the soil samples were not fully saturated at the time of testing; therefore, these results would not be representative of the undrained shear strength. Applying an unconfined compression test to unsaturated samples will yield erroneously high values of c_u because of compaction that occurs during compression. A grouping of five samples from the dominant soil strata (Old Paleosol) yielded values for the unconfined compressive strength, q_u, that were significantly lower than the majority of those tested. This would possibly indicate that these samples were saturated or nearly saturated at the time of testing, and therefore the lower values of q_u would be more reflective of the undrained soil strength. The mean value of q_u from these five samples is 76.6 kPa. For saturated soil, $c_u = q_u/2$ [e.g., Spangler and Handy (1982), page 461]; therefore, $c_u = 37.3$ kPa. This value of c_u will be assumed to be representative for all Hotophia Creek sections, and is analogous to the "worst-case" values assumed by Darby and Thorne (1996a). The average unit soil weight, γ_s, for the five samples is 19 kN/m³.

Thorne et al. (1981) emphasize the importance of tension cracking and subsequent slab-type failures at Hotophia Creek. Within the zone of tension, cracks are likely to exist; therefore, the cohesional portion of the shearing strength cannot be relied upon (Taylor 1948, page 450). The reduction in bank stability due to tension cracking can be approximated by reducing the value of c_u by the proportion of the failure surface that is within the tension zone (Terzaghi 1943, page 174; Taylor 1948, page 450). Actual tension crack depths from the banks of Hotophia Creek were measured by Thorne et al. (1981). The mean crack depth and the standard deviation were 2.6 m and 0.7 m, respectively ($n = 31$). Now Terzaghi (1943, page 154) has stated, "Under normal conditions the depth of tension cracks does not exceed about one half the height of a vertical slope." Therefore, for banks less than 5.2 m in height, a tension crack depth equal to $H/2$ will be assumed.

Stability of the Hotophia Creek banks will be assessed using (3) and (4), together with the modified undrained cohesion, c_m

$$c_m = \begin{cases} \dfrac{(H - 2.6)}{H} c_u, & H \geq 5.2 \text{ m} \\ \dfrac{c_u}{2}, & H < 5.2 \text{ m} \end{cases} \tag{18}$$

where $c_u = 37.3$ kPa. By using the modified undrained cohesion, c_m, Taylor's slip circle analysis can now be used to assess the stability of riverbanks subject to tension cracking and slab-type failures.

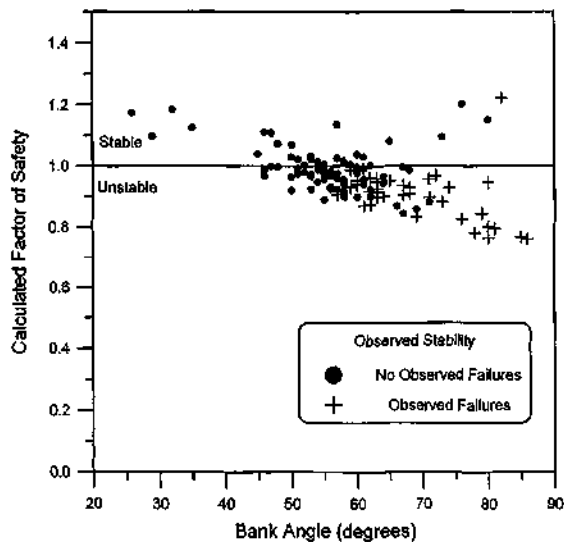Hotophia Creek and surrounding drainages were unstable

FIG. 5. Calculated FS_H for Hotophia Creek Survey Bank Sections [Data from Thorne et al. (1981)]

and actively degrading at the time of the surveys (Thorne et al. 1981); therefore, the values of FS_H should be close to 1.0. Values of FS_H calculated using (3) and (4) with c_m and $\gamma_t = 19$ kN/m³ ranged between 0.76 and 1.22, with an average value of 0.96. This average value compares well with the expected value of 1.0. With the exception of one outlier, the bank sections that failed between January 1978 and July 1979 correctly plot within the unstable region where $FS_H < 1.0$ (Fig. 5). However, the majority of the bank sections that did not fail between the two surveys also plot within the unstable region. This may indicate that these banks are inherently unstable, and would be liable to fail following heavy rainfall or flood inundation when the banks become saturated. Alternatively, the modified undrained cohesion, c_m, as calculated using (18), is strictly valid only for vertical banks, and may be overcompensating for tension cracking at lower angle banks.

In summary, the simple total stress analysis proposed in the present paper does indicate that the banks of Hotophia Creek are generally unstable, and does appear to provide a reasonable basis for estimating the stability of riverbanks with respect to mass failure.

Results from Data of Charlton et al. (1978)

The optimization model will now be used to analyze data from natural gravel-bed rivers collected by Charlton et al. (1978). Fourteen reaches described as having banks composed of fine sand, silt, or clay for which measures of the bank strength were given have been selected for analysis in the present paper (Table 1). Values for the channel roughness, k_s, were back-calculated for each reach using (14) and (15). The unconfined compressive strength of the bank material, q_u, was measured by Charlton et al. (1978) at a number of locations at each site, and an average was given. It has been assumed that samples of the bank material were saturated at the time of testing, and therefore $c_u = q_u/2$ [e.g., Spangler and Handy (1982), page 461]. The bank vegetation was characterization as either G, in which the banks have a covering of grass of light vegetation, or T, in which the banks are protected with trees or vegetation whose root system restricts bank erosion (Charlton et al. 1978). Because of the presence of bank vegetation, no allowance has been made for tension cracks.

The value of τ_{crit} is not known for any of the reaches, and there is no basis to assume representative values. Initially, the bank stability will be assessed only with respect to mass failure. The primary purpose of this analysis is to differentiate

between the bank-height constrained ($FS_H = 1.0$) and bank-shear constrained ($FS_\tau = 1.0$) channels. It will then be demonstrated that the optimization model can be calibrated to the observed channel geometry, and used to estimate reach-averaged values of τ_{crit} for the bank-shear constrained channels.

Estimation of Critical Height

The first stage of the analysis is to calculate the critical bank height, H_{crit}, and to compare this value to the observed bank height, H_{obs}. H_{crit} has been calculated using (3) and (4). Values of θ were not given in Charlton et al. (1978); therefore, a range from about 30° to 90° will be considered. There is also some uncertainty associated with the values of c_u. A single "average" value of the unconfined compressive strength, q_u, was given by Charlton et al. (1978); however, few details were given as to how this value was obtained. It will be assumed that the "true" value of c_u lies within the range of ±25% of the value of c_u from Table 1.

To reflect this uncertainty in c_u and θ, the "most probable" value of H_{crit} has been calculated using the value of c_u from Table 1, together with $\theta = 60°$. The maximum likely value of H_{crit} has been calculated using 1.25 c_u together with $\theta \approx 30°$; and the minimum likely value with 0.75 c_u together with $\theta = 90°$. Results are summarized in Table 2. Values of H_{obs} for reaches 5, 10, and 12 fall within the range between the calculated minimum and maximum values of H_{crit}. For reaches 1–4, 6–9, 11, and 14, the values of H_{obs} are less than the minimum calculated value of H_{crit}. For reach 13, H_{obs} is greater than the maximum H_{crit}.

These results are interpreted as follows. Two basic channel types are identified on the basis of the active bank stability constraint; bank-height and bank-shear constrained. For reaches 5, 10, and 12, values of H_{obs} fall within the range calculated for H_{crit}; therefore, these channels are designated as bank-height constrained. This indicates that the stable channel width and depth are limited by the mass failure stability of the banks. For reaches 1–4, 6–9, 11, and 14, H_{obs} values are less than the minimum calculated H_{crit}. These channels are not constrained by mass failure processes, and are assumed, therefore, to be bank-shear constrained. This means that the banks of these channels would have developed at the limiting stability with respect to fluvial erosion; that is, $\tau_{bank} \approx \tau_{crit}$. Reach 13 is anomalous in that H_{obs} is greater than the maximum calculated H_{crit}. It appears that the value of c_u is not representative of the actual strength of the bank material; therefore, reach 13 will be excluded from any further analyses.

TABLE 2. Comparison of Observed Bank Height, H_{obs}, with Calculated Critical Bank Height, H_{crit}

Reach number (1)	H_{obs} (m) (2)	Calculated H_{crit} (m)			Constraint (6)
		Minimum (3)	Probable (4)	Maximum (5)	
1	1.78	2.84	5.23	8.13	BS
2	0.73	1.84	3.39	5.27	BS
3	0.73	1.67	3.07	4.78	BS
4	1.34	3.69	6.81	10.59	BS
5	1.79	1.67	3.09	4.80	BH
6	1.36	5.09	9.39	14.60	BS
7	1.77	1.87	3.46	5.37	BS
8	1.63	2.16	3.99	6.20	BS
9	0.69	1.85	3.42	5.31	BS
10	2.47	1.13	2.08	3.23	BH
11	0.65	2.64	4.86	7.56	BS
12	2.64	1.53	2.82	4.39	BH
13	4.19	1.15	2.12	3.30	BH
14	1.67	2.87	5.29	8.22	BS

Note: The assigned active bank stability constraint is shown in column 6. BS = bank-shear constrained; BH = bank-height constrained.

Analysis Excluding Bank-Shear Constraint

Data from Table 1 (excluding reach 13) were used as input into the optimization model. Because no reasonable estimate of τ_{crit} was available, the bank-shear constraint has not been included in the initial analysis, and the stability of the rivers has been assessed only with respect to mass failure. The three designated bank-height constrained reaches (5, 10, and 12) scatter about the line of perfect agreement for both the channel width and the mean depth [Figs. 6(a) and 6(b)]. Because there are only three data points, it is not possible to comment on whether the scatter is due to uncertainty in the adopted soil parameters, or whether this represents a limitation of the model or the bank stability analysis. Additional field data are needed to fully test the model.

The more interesting observation is that the calculated geometries for those reaches designated as bank-shear constrained are all narrower and deeper than those of the observed river channels [Figs. 6(a) and 6(b)]. Because these channels are not constrained by the bank height, their stable width must have developed at the limiting stability with respect to fluvial erosion; that is, when $FS_r = 1.0$ or $\tau_{bank} = \tau_{crit}$. On this basis,
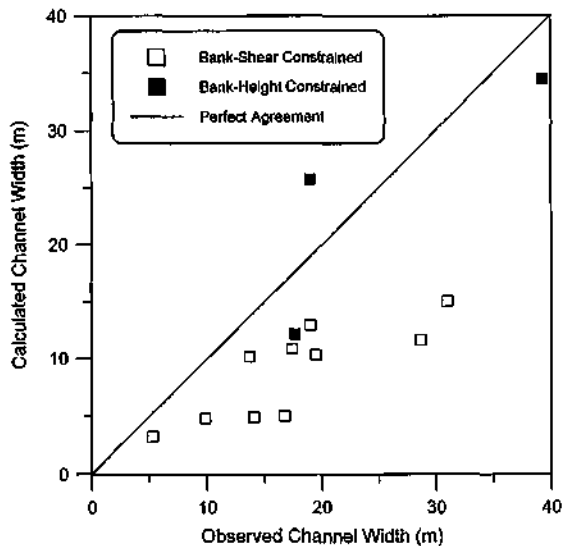

FIG. 6(a). Comparison of Calculated and Observed Channel Dimensions; Analysis Excluding Bank-Shear Constraint: Channel Width
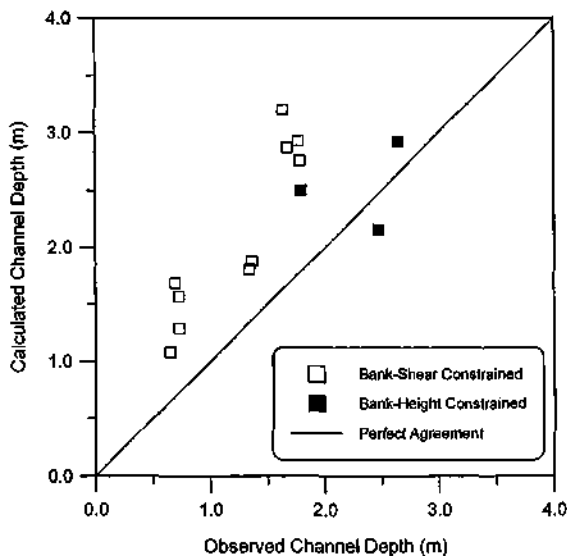

FIG. 6(b). Comparison of Calculated and Observed Channel Dimensions; Analysis Excluding Bank-Shear Constraint: Channel Depth

TABLE 3. Calculated Values of τ_{crit} for Designated Bank-Shear Constrained Channels

Reach number (1)	τ_{crit} (Pa) (2)	FS_H (3)	Vegetation type (4)
1	54.1	2.0	T
2	28.2	3.2	G
3	63.2	2.8	T
4	41.7	3.3	T
6	92.7	4.8	T
7	19.6	1.4	G
8	13.8	1.7	T
9	12.4	3.4	G
11	10.7	4.8	G
14	22.5	2.1	G

Note: Bank vegetation types are indicated in column 4. T indicates banks with trees and vegetation that restricts bank erosion; G indicates weakly vegetated or grass-covered banks.

the optimization model can be calibrated against the field data to provide estimates of τ_{crit}.

Estimation of τ_{crit}

For each of the 10 channels identified as being bank-shear constrained, a series of trial values of τ_{crit} were input until agreement was forced between calculated and observed channel widths. This effectively yields calibrated estimates of τ_{crit} (Table 3). The computed values of FS_r for these channels are all equal to 1.0. The computed values of FS_H are all significantly greater than 1.0 (Table 3), indicating that the stable channel geometry of these bank-shear constrained channels is not influenced by the mass failure properties of the banks. Therefore, any error in the adopted values of c_u will have no influence on the estimates of τ_{crit} obtained from the model calibration.

Not surprisingly, bank vegetation appears to exert influence on the calculated reach-averaged value of τ_{crit}. The channel reaches described as having grass-covered or lightly vegetated banks ($n = 5$) returned an average value and standard deviation for τ_{crit} of 18.7 Pa and 7.2 Pa, respectively. For the tree-covered or more densely vegetated channel banks ($n = 5$), the average and standard deviation are 53.1 Pa and 28.9 Pa, respectively. These results indicate a significant increase in the reach-averaged value of τ_{crit} for the more densely vegetated channel banks.

The optimization model could potentially be used to assess the effect of revegetation of the channel banks on the stable channel width. For example, planting of the trees along the banks of reach 2 might result in an increase in τ_{crit} from 28.2 Pa to, say, 50 Pa. The effect would be a reduction in the stable channel width by over 50%, from the current 14.0 m to about 6.7 m.

ANALYSIS

A mass failure stability analysis [based on the $\phi = 0$ total stress analysis developed by Taylor (1948)] has been tested using data from Hotophia Creek (Thorne et al. 1981), and appears to provide a reasonable estimate of the stability of the banks of this degrading stream. This analysis assumes saturated, undrained conditions at the time of failure, and complete drawdown of the water level in the channel. This assumption is probably reasonable when applied to poorly drained banks, and/or to rivers and streams with "flashy" runoff.

The proposed analysis can be used where a routine estimate of the mass failure stability of a length of channel is required. Rather than a detailed slope-stability analysis at a single location, which is the goal of many geotechnical investigations, the objective is to determine the average stability of a river

reach, and whether the reach is bank-height or bank-shear constrained. Estimates of FS_H obtained using (3) and (4) should be viewed as an approximation only. As a rule of thumb, values of $FS_H < 1.25$ can probably be assumed to indicate that the bank is at or near the limiting mass failure stability, and therefore the channel is probably bank-height constrained. For values of $FS_H > 1.25$, the channel can probably be assumed to be bank-shear constrained. Evidence of toe scour and mass failure from field observation should be used to support the calculated bank stability.

A major limitation is defining a representative or "average" value of c_u for the reach. Depending upon the soil type, c_u could be estimated in situ using low-cost methods such as the vane shear or penetrometer method, or from laboratory tests such as an unconfined compression test or the "quick" undrained unconsolidated triaxial test (Spangler and Handy 1982). The main advantage of the total stress analysis compared to an effective stress analysis is the significantly lower cost of soil testing. This allows more samples to be tested, and therefore a more representative value of c_u for the entire reach can be obtained. The effect of vegetation on the mass failure stability, such as that being investigated in Abernethy and Rutherfurd (1998), can be incorporated into the existing bank stability constraint by modifying the value of c_u to reflect the effect of bank vegetation. Site-specific stability curves could be developed using other mass failure mechanisms and could be used in place of (4). These curves could possibly account for the effects of nonhomogeneous soil and bank vegetation in a more rigorous manner than by simply adjusting the bulk value of c_u.

The proposed division of channel types into bank-height and bank-shear constrained is consistent with recent conceptual models and field observations by Lawler (1992) and Abernethy and Rutherfurd (1998). Lawler (1992) developed a conceptual model whereby the dominant erosion process changes in a downstream direction from fluvial erosion to mass failure. Fluvial erosion dominates in the small, steep headwater streams, while mass failure dominates in the large, low-gradient lowland rivers. Abernethy and Rutherfurd (1998) provide field evidence that generally supports Lawler's model. (Lawler also considered an additional erosion process, subaerial preparation, but this has not been considered in the present paper.)

It is generally accepted that bank vegetation exerts a significant effect on the bank stability, and hence the stable channel width. The effect of the bank vegetation on the stability of the banks with respect to fluvial erosion is probably twofold, in that it decreases the erodibility of the soil through reinforcement and binding of the soil matrix by the roots, and reduces the near-bank velocity and τ_{bank}. The value of τ_{crit} obtained indirectly through the calibration procedure is a gross value that includes both aforementioned effects. Revegetation is being more widely adopted as a softer, environmentally friendly approach to streambank stabilization. However, as yet there is no widely accepted approach to quantifying the effect of revegetation on either the bank stability or the stable channel width, and few quantitative design guidelines are available. It is suggested that the optimization model developed in the present paper, as well as the formulation in Millar and Quick (1993) for noncohesive channels, can be used as a basis for quantifying the effect of bank vegetation in terms of τ_{crit}, and can be used to assess the effect of bank stabilization programs on the stable channel geometry.

For bank-shear constrained channels, the optimization model can be used to obtain calibrated estimates of τ_{crit}, which are otherwise difficult to measure directly. With further study, it may be possible to relate the values of τ_{crit} obtained through model calibration to soil and vegetation type, or other features. In this way, the model could be used to develop site-specific or local values of τ_{crit} that could then be used for channel design or river restoration activities.

CONCLUSIONS

The following conclusions have been reached. They remain tentative until additional field data can be obtained to further verify the model.

The limiting mass failure stability of cohesive riverbanks can be estimated using Taylor's (1948) $\phi = 0$ stability analysis. The limiting stability is presumed to occur during drawdown when the banks are saturated, and assumes that undrained conditions occur at the time of failure. Taylor's analysis represents a simple approach that appears to provide a reasonable estimate of the factor of safety with respect to mass failure.

It is proposed that the stable channel width corresponds to an optimum condition, and develops when the riverbanks are at their limiting stability with respect to either mass failure or fluvial erosion. Two fundamental channel types can then be identified on the basis of the active bank stability constraint: (1) bank-height; or (2) bank-shear constrained. Bank-height constrained channels develop banks at the critical bank height, and are subject to erosion by mass failure. Bank-shear constrained channels develop at the critical bank shear stress, and are subject to fluvial erosion and toe scour.

Because the stable geometry is thought to develop at the limiting bank stability, bank stability parameters can be estimated indirectly through calibration of the model to the observed channel geometry. This approach has been applied to field data from Charlton et al. (1978). Those riverbanks that were described as having a coverage of vegetation that restricts bank erosion returned values of τ_{crit} that were approximately three times greater than those with weakly vegetated, grass-covered banks, so the effect of the bank vegetation on the value of τ_{crit} has a large influence on the stable channel width. Bank vegetation may also have a significant effect on the mass failure stability of riverbanks; however, at present, there are insufficient data to demonstrate this.

ACKNOWLEDGMENTS

APPENDIX I.   REFERENCES

Abernethy, B., and Rutherford, I. D. (1998). "Where along a river's length will vegetation most effectively stabilize stream banks?" *Geomorphology*, 23, 55–75.

Arulanandan, K., Gillogley, E., and Tully, R. (1980). "Development of a quantitative method to predict critical shear stress and rate of erosion of natural undisturbed cohesive soils." *Tech. Rep. GL-80-5*, U.S. Army Engrg. Wtrwy. Experiment Station, Vicksburg, Miss.

Atkinson, J. (1993). *An introduction to the mechanics of soils and foundations through critical state soil mechanics*. McGraw-Hill Book Co., Inc., London.

Bishop, A. W. (1955). "The use of the slip circle in the stability analysis of slopes." *Geotechnique*, 5(1), 7–17.

Bray, D. I. (1980). "Evaluation of effective boundary roughness for gravel-bed rivers." *Can. J. Civ. Engrg.*, 7, 392–397.

Chang, H. H. (1980). "Geometry of gravel streams." *J. Hydr. Div.*, ASCE, 106(9), 1443–1456.

Chapuis, R. P., and Gatien, T. (1986). "An improved rotation cylinder technique for quantitative measurements of the scour resistance of clays." *Can. Geotech. J.*, 23(1), 83–87.

Charlton, F. G., Brown, P. M., and Benson, R. W. (1978). "The hydraulic geometry of some gravel rivers in Britain." *Rep. IT 180*, Hydr. Res. Station, Wallingford, England.

Darby, S. E., and Thorne, C. R. (1996a). "Development and testing of riverbank-stability analysis." *J. Hydr. Engrg.*, ASCE, 122(8), 443–454.

Darby, S. E., and Thorne, C. R. (1996b). "Numerical simulation of wid-

ening and bed deformation of straight, sand-bed rivers. I: Model development." *J. Hydr. Engrg.*, ASCE, 122(4), 184–193.

Flintham, T. P., and Carling, P. A. (1988). "The prediction of mean bed and wall boundary shear in uniform and compositely roughened channels." *International conference on river regime*, W. P. White, ed., John Wiley & Sons, Inc., Chichester, England, 267–287.

Grissinger, E. H. (1982). "Bank erosion of cohesive materials." *Gravel-bed rivers*, R. D. Hey, J. C. Bathurst, and C. R. Thorne, eds., John Wiley & Sons, Inc., Chichester, England, 273–287.

Hagerty, D. J. (1991). "Piping/sapping erosion. I: Basic considerations." *J. Hydr. Engrg.*, ASCE, 117(8), 991–1008.

Hey, R. D. (1979). "Flow resistance in gravel-bed rivers." *J. Hydr. Div.*, ASCE, 105(4), 356–379.

Ikeda, S., and Izumi, N. (1990). "Width and depth of self-formed straight gravel rivers with bank vegetation." *Water Resour. Res.*, 26(10), 2353–2364.

Knight, D. W. (1981). "Boundary shear in smooth and rough channels." *J. Hydr. Div.*, ASCE, 107(7), 839–851.

Knight, D. W., Demetrious, J. D., and Hamed, M. E. (1984). "Boundary shear in smooth rectangular channels." *J. Hydr. Div.*, ASCE, 110(4), 405–422.

Lane, E. W. (1955). "The design of stable channels." *Trans., ASCE*, Reston, Va., 120, 1234–1279.

Lawler, D. M. (1992). "Process dominance in bank erosion." *Lowland floodplain rivers*, P. A. Carling and G. E. Petts, eds., John Wiley & Sons, Inc., Chichester, England.

Lohnes, R., and Handy, R. L. (1968). "Slope angles in friable loess." *J. Geol.*, 76(3), 247–258.

Millar, R. G., and Quick, M. C. (1993). "Effect of bank stability on geometry of gravel rivers." *J. Hydr. Engrg.*, ASCE, 119(12), 1343–1363.

Moore, W. L., and Masch, F. D. (1962). "Experiments on the scour resistance of cohesive sediments." *J. Geophys. Res.*, 67(4), 1437–1449.

Osman, A. K., and Thorne, C. R. (1988). "Riverbank stability analysis. I Theory." *J. Hydr. Div.*, ASCE, 114(2), 134–150.

Parker, G. (1978). "Self-formed rivers with equilibrium banks and mobile bed. Part 2. The gravel river." *J. Fluid Mech.*, 89(1), 127–146.

Pizzuto, J. E. (1990). "Numerical simulation of gravel river widening." *Water Resour. Res.*, 26(9), 1971–1980.

Raudkivi, A. J. (1990). *Loose boundary hydraulics*, 3rd Ed., Pergamon Press, Inc., Tarrytown, N.Y.

Spangler, M. G., and Handy, R. L. (1982). *Soil engineering*, 4th Ed., Harper & Row, Publishers, Inc., New York.

Stevens, M. A. (1989). "Width of straight alluvial channels." *J. Hydr. Engrg.*, ASCE, 115(3), 309–326.

Taylor, D. W. (1948). *Fundamentals of soil mechanics*. John Wiley & Sons, Inc., New York.

Terzaghi, K. (1943). *Theoretical soil mechanics*. John Wiley & Sons, Inc., New York.

Thorne, C. R. (1982). "Processes and mechanisms of riverbank erosion." *Gravel-bed rivers*, R. D. Hey, J. C. Bathurst, and C. R. Thorne, eds., John Wiley & Sons, Inc., Chichester, England, 227–271.

Thorne, C. R., Murphey, J. B., and Little, W. C. (1981). "Stream channel stability appendix D: Bank stability and bank material properties in the bluffline streams of northwestern Mississippi." *Rep. Prepared for U.S. Army Corps of Engrs.*, Vicksburg District, Vicksburg, Miss.

Ullrich, C. R., Hagery, D. G., and Holmberg, R. W. (1986). "Surficial failures of alluvial stream banks." *Can. Geotech. J.*, 23(3), 304–316.

Vanoni, V. A. (1975). *Sedimentation engineering*. ASCE Manuals and Rep. on Engrg. Pract., 54, ASCE, Reston, Va.

Vigilar, G. G., and Diplas, P. (1997). "Stable channels with mobile bed: Formulation and numerical solution." *J. Hydr. Engrg.*, ASCE, 123(3), 189–199.

White, W. R., Bettess, R., and Paris, E. (1982). "An analytical approach to river regime." *J. Hydr. Div.*, ASCE, 108(10), 1179–1193.

APPENDIX II.   NOTATION

The following symbols are used in this paper:

A = cross-sectional area of flow (m^2);

bank = subscript indicating bank component;

bed = subscript indicating bed component;

c = soil cohesion in terms of total stress (kPa);

c' = soil cohesion in terms of effective stress (kPa);

c_m = modified soil cohesion to account for tension cracking (kPa);

D_{50} = median grain diameter of pavement sediment (m);

D_{84} = grain diameter where 84% of sample is finer (m);

FS_H = factor of safety with respect to height;

FS_τ = factor of safety with respect to bank shear;

F_1 = parameter related to fall velocity of bed load sediment (≈ 0.82);

f = friction factor;

G = indicates weakly vegetated or grass-covered banks;

G_b = bed load transporting capacity (kg/s);

g = gravitational acceleration (9.8 m/s^2);

g_b = bed load transporting capacity of channel per unit bed width (kg/s/m);

g_b^* = dimensionless bed load transport rate per unit width;

H = vertical bank height (m);

H_{crit} = critical bank height corresponding to factor of safety equal to 1.0 (m);

H_{obs} = observed vertical bank height (m);

k_s = equivalent roughness (m);

N_s = dimensionless stability number;

P = total channel perimeter (m);

P_{bank} = bank perimeter (m);

P_{bed} = bed perimeter (m);

Q_{bf} = bank-full discharge (m^3/s);

R_h = hydraulic radius (m);

S = channel slope;

SF_{bank} = proportion of shear force acting on banks;

s = specific gravity of gravel sediment on bed (2.65);

T = indicates banks with trees and vegetation that restricts bank erosion;

U = mean velocity (m/s);

W = surface width (m);

Y = flow depth (m);

$\bar{Y}$ = average flow depth (m);

γ = unit weight of water (9,810 N/m^3);

γ_s = saturated unit weight of soil (kN/m^3);

θ = bank angle (°);

ρ = density of water (1,000 kg/m^3);

σ = total stress (kPa);

σ' = effective stress (kPa);

τ = mean channel shear stress (Pa);

τ_{bank} = average bank shear stress (Pa);

τ_{bed} = average bed shear stress (Pa);

τ_{crit} = critical shear stress for fluvial erosion of bank sediment (Pa);

$\tau_{b_{50}}^*$ = dimensionless bed shear stress for median bed load–grain diameter;

ϕ = friction angle of bank soil in terms of total stress (°); and

ϕ' = friction angle of bank soil in terms of effective stress (°).

STREAMBANK EROSION DUE TO BED DEGRADATION — A MODEL CONCEPT

C. V. Alonso, S. T. Combs

ABSTRACT

Processes of fluvial erosion which operate on the banks of alluvial streams are examined by considering mechanisms of bed and bank erosion and mass failure of drained, homogeneous, cohesive banks. These concepts are used to formulate a mathematical model to evaluate bed degradation for the case in which bed lowering causes bank instability. Application of the model to a laboratory experiment verifies the behavior of the bed degradation submodel. Analysis of a more complex scenario demonstrates the importance of considering streambank erosion in streambed degradation analyses.

INTRODUCTION

Erosion of channel banks causes severe damage to land and adjoining property. This is a common occurrence along many miles of streams throughout the United States. In many sections of the country, this problem has reached acute stages. Channel erosion is very costly; removing sediment from chocked streams and reservoirs in the United States is estimated to exceed $250 million a year. In addition, the loss of prime agricultural land and adjacent property is valued at millions of dollars annually (Bowie, 1982). There is a continuing need for criteria that can be effectively used to estimate the effectiveness of channel planning and design.

In this article, the processes of erosion and mass failure which operate on the banks of alluvial channels are briefly outlined in order to illustrate the way in which a stream erodes its banks. A mathematical model of these processes is presented in the second part of this article. The model is used to illustrate the balance between rates of supply and removal, and its effect on rates of bank retreat and bed degradation.

MECHANISMS OF BANK DESTABILIZATION

Channel bank erosion usually occurs as direct erosion by flood water or the washing away of detached material after massive bank failure by sloughing or sliding. The sloughing or sliding process is usually triggered by reduction of the bank's internal strength which can be caused by saturation, foundation deterioration caused by seepage, piping, or undermining of the toe of the channel bank, or a combination of these processes.

Hydraulic scour of the bed and bank toe increases the bank's height and slope angle, decreasing its stability with respect to gravity induced mass failure. Overheightening and oversteepening of the bank continues until the forces tending to cause failure exceed those opposing failure. At this point, failure takes place delivering bank material to the basal area. Removal of bank debris from this area depends entirely on the capacity of the streamflow to breakup and entrain debris and transport it downstream. As long as flow is able to remove the debris and also scour the basal area, bank retreat will continue. When the flow can no longer remove all of the debris, basal accumulation will begin, thus protecting the base against erosion, making the banks less steep and more stable (Alonso and Combs, 1986).

Principal factors affecting the stability of stream banks are streamflow characteristics, physical properties of bed and bank material, geometry and stratigraphy of the banks, seepage forces, climatic conditions, and vegetative protection. A thorough discussion of all of these factors is beyond the scope of this report, but a fairly comprehensive treatment is presented by Thorne (1982). Our discussion is limited to processes of erosion by flow and failure mechanisms of drained, homogeneous, cohesive banks. Extensive discussions of fluvial erosion of non-cohesive banks can be found in Vanoni (1975), and Simons and Senturk (1976). Stability of undrained and stratified cohesive banks is discussed by Carson and Kirby (1972), and Thorne and Tovey (1981).

BANK EROSION BY FLOW

Flow in a channel generates shear stress on the bed and banks, causing bank retreat in two ways. First, material may be eroded directly from the bank and carried downstream by the flow. Second, if the shear stress acting on the streambed exceeds the critical shear stress, the bed material will be set in motion. If the potential transport capacity of the flow exceeds the inflow of sediment from upstream, bed degradation will occur with a concomitant increase in bank angle and height. However, the rate of entrainment of bank and bed material is controlled by the size, geometry, and structure of those materials.

The actual distribution of shear stresses on the banks of natural channels can be quite irregular and difficult to evaluate (Bathurst, 1979). In channels exhibiting a nearly trapezoidal cross-sectional shape, the shear stress on the banks can be determined from the classical work of Olsen and Florey (1952). Contemporary investigations based on advanced turbulent flow models hold promise as boundary-shear predictors for generalized geometries (Pizzuto, 1987).

The mechanics of cohesive bank material entrainment by flow is still poorly understood. Most of the available research is reviewed in the ASCE Task Committee Report (1968) and the texts by Graf (1971) and Raudkivi (1976). More recently, Arulanandan et al. (1980) developed a method to calculate the rate of erosion of cohesive materials based on laboratory measurements. In these experiments, they tested undisturbed soils using distilled water as the eroding fluid. This is perhaps the most promising of the available methods, because it takes into account the electrochemical properties of the soil, pore water, and eroding fluid. Cohesive bank materials often consist of large aggregates of strongly bonded conglomerates of clay, silt, and sand particles. As a result, fluvial erosion of cohesive soil often takes place by the entrainment of aggregates rather than primary particles. Furthermore, the susceptibility of cohesive banks to erosion by flow entrainment depends on their moisture content and degree of weathering. Hard, dry banks are very resistant, while wet banks are easily eroded.

Streambed degradation can proceed downstream as well as upstream depending upon the type of degradation. In contrast to "scour", which usually refers to local and often temporary lowering of bed levels over a short distance, "degradation" implies an extensive and often progressive lowering of the streambed over fairly long distances. Downstream progressing degradation is generally the result of changes in discharge, upstream sediment supply, or sediment size. Upstream progressing degradation is generally the result of an imposed increase in bed slope which can be caused by lowering the base level, decreasing the stream length (meander cutoff), or removing a control point. Examples of these and other problems of degradation are frequently found in the technical literature; a comprehensive account is presented by Galay (1983).

The preceding discussion applies to streams with little or no sinuosity. To extend the analysis to meandering streams, it is necessary to take into account the increased shear stress acting on the outer bank of a stream bend, and the additional lowering of the outer bank toe due to transverse scour of the bed. Analysis of flow and sedimentation processes in stream meanders is still a major research topic (Falcon and Kennedy, 1983; Odgaard and Bergs, 1988; Ikeda and Parker, 1989). Nevertheless, this topic is well beyond the scope of this article which is restricted to the analysis of bank stability in nearly straight stream reaches.

MASS FAILURE OF HOMOGENEOUS, COHESIVE BANKS

There are two common types of slope failure. One is progressive, continuous failure by creep movement over long periods of time. The other is catastrophic shear failure of the bank. The latter is the most frequent mode of failure in cohesive banks. Rapid movement usually occurs when the shear strength along a slip surface within the slope is exceeded, either because of a reduction in the shear strength of the bank material or an increase in the stress due to saturation or human activities. In contrast to non-cohesive banks maintained at the natural angle of repose, where stability is independent of height, the stability of cohesive banks is strongly dependent on both the bank slope angle and height. Most often failure occurs by a deep-seated slip, although shallow slips also occur. The

types of failure mechanisms most frequently associated with cohesive stream banks are rotational slip, plane slip, and cantilever failure. An extensive account of these and other types of slope failure is presented by Thorne (1982).

In rotational slips, failure takes place along a circular surface [fig. 1 (a)]. The slip may be a base, toe, or slope failure depending on where the slip arc intersects the soil surface. Non-circular slips are associated with highly fissured materials, non-homogeneous banks, and certain types of soil drainage. Rotational failures are critical in cohesive banks of great height and comparatively low slope. This is the case because in sloping cohesive banks the orientation of the principal stresses changes with depth, which changes the orientation of the slip surface. Rotational failure has been reported in field and laboratory studies (Turnbull et al., 1966; Sullivan, 1972; Frydman and Beasley, 1976).

Plane slip failure is frequently observed in steep bank slopes [fig. 1 (b)]. In nearly vertical cohesive banks there is little change in the orientation of the principal stresses with depth, and the failure surface is almost planar (Carson and Kirby, 1972). Behind steep banks, significant tensile stress can be generated adjacent to the upper part of the bank. This leads to the development of vertical tension cracks [fig. 1 (b)] which results in slab failure of the banks by tension cracking and plane slip. Mass failure and retreat of nearly vertical stream banks has been reported by Lohnes and Handy (1968), Bradford and Piest (1977) and by Little et al. (1982).

When a streambank is subject to undercutting as the result of seepage, wave action, or basal erosion an overhang or cantilever can develop in the upper bank [fig. 1 (c)]. This cantilever remains in place until a state of
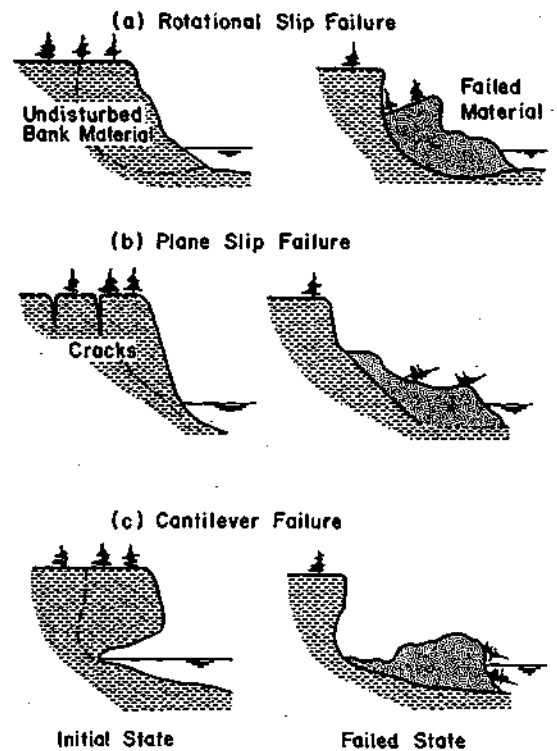

Figure 1—Stream-bank failure mechanisms.

limiting equilibrium as a result of further undercutting or weakening by wetting or cracking is reached. It then fails by shear, beam or tensile failure depending on its shape. The analysis of cantilever failure was undertaken by Thorne and Tovey (1981). They concluded that this mechanism of failure depends on cantilever geometry rather than on soil strength.

The stability of cohesive banks subject to rotational and plane failures may be analyzed by considering the balance between disturbing and restoring forces acting on the slip surface. The most simple approach is the Culmann method, which assumes a plane slip surface passing through the bank toe (Lohnes and Handy, 1968). This method is only applicable to low, near-vertical banks. Deep-seated failures of high banks with low slope angles are treated assuming circular arcs or logarithmic spirals for the slip surfaces.

A Modeling Approach To Stream Bank Stability Analysis

This section outlines a mathematical model designed to simulate streambank erosion and instability resulting from bed degradation. A shorter description of this model was presented by the authors in an earlier report which also considered bank accretion processes (Alonso and Combs, 1986). Recently, a similar analysis of bank retreat incorporating the effect of tension cracks was reported by Osman and Thorne (1988).

It has been recognized for quite some time that, in spite of the many factors which affect bank erosion, the width and other geometric properties of a stream are strongly correlated with flow characteristics. This concept lends validity to the present analysis in which streams are considered to widen until the critical shear stresses on the banks are no longer exceeded and erosion of the toe of the banks stops. Consequently, bank retreat and changes in streambed profile are considered closely interrelated. The analysis is restricted to streams confined between steep, cohesive banks and streambeds deforming within well-sorted, non-cohesive alluvial material. The model incorporates components for water and sediment routing, changes in longitudinal bed profile, and variations in channel width due to bank failure and retreat.

The stream reach is divided into sub-reaches, and the computations for each sub-reach are performed for successive, discrete time intervals. In each time interval, the model solves the governing equations in three steps:

1. The equations governing water and sediment movement are solved in the first step to obtain water surface elevation, flow depth, velocity, and sediment discharge at each computational point.
2. Bank-toe scour by fluvial erosion is computed, and the bed-material continuity equation is solved to yield depths of bed degradation or aggradation.
3. The streambank is tested for stability. If it is not stable, the mass of failed bank material is used to satisfy the transport capacity of flow during the basal clean-out phase.

Further approximations incorporated in the model, as well as the initial and boundary conditions required for the solution of the governing equations are presented in the following sections.

Streamflow and Sediment Routing

Water Routing. Water routing provides temporal and spatial variations of the stage, discharge, energy gradient, and other hydraulic parameters in the channel. The channel is assumed sufficiently straight and uniform within the reach of interest for the streamflow to be adequately characterized by a one-dimensional model. In this case, the equations governing gradually varied, unsteady flows in an erodible channel are (Chen, 1973):

$$\frac{1}{gA}\frac{\delta Q}{\delta t} + \frac{1}{gA}\frac{\delta}{\delta x}\left(\frac{\beta}{A}Q^2\right) +$$

$$\frac{\delta h}{\delta x} + \frac{\delta z}{\delta x} + S_f = 0 \tag{1}$$

$$\frac{\delta Q}{\delta x} + \frac{\delta A}{\delta t} + B\frac{\delta z}{\delta t} = q_L \tag{2}$$

where
Q = water discharge,
A = flow area,
β = momentum flux correction,
h = flow depth,
z = elevation of channel bottom,
S_f = friction slope,
g = acceleration of gravity,
B = active-bed width,
q_L = lateral water inflow per unit length of channel,
x = distance along the channel, and
t = time.

In the present analysis the discharge hydrograph is considered to vary sufficiently slowly for it to be treated as a sequence of discrete steady events, each with a specified duration Δt. Changes in the bed layer within each period Δt are assumed to remain negligible in comparison with changes in the flow area. Furthermore, lateral inflows are restricted to point contributions from tributaries. Under these assumptions, equations 1 and 2 can be approximated as:

$$\frac{\delta}{\delta x}\left(\frac{1}{2g}V^2 + h + z\right) + S_f = 0 \tag{3}$$

$$Q(x + \delta x) = Q(x) + Q^t(x) \tag{4}$$

where
Q^t = the water discharge at a tributary mouth, and
V = the average flow velocity.

It is shown below that at moderate Froude numbers, small bed perturbations propagate at a rate much smaller than surface waves. These waves, in turn, are not affected by the bed disturbances and propagate as if the bed were fixed. Consequently, when these conditions are present, the solution can be simplified by uncoupling the equations governing water motion from those governing bed deformation. In order to take advantage of this property, the

analysis is limited to situations involving low-flow regimes. Thus, starting from a known or specified water-surface elevation at the downstream end of the reach, the calculation scheme solves equations 3 and 4 by an iterative scheme analogous to the standard step method for backwater calculations. Because of the interdependence between water surface profile, flow resistance and sediment transport capacity, computation of these hydraulic variables proceeds simultaneously. Thus, the model calculates depth, velocity, energy slope, and sediment discharge at successive cross sections in a single computational sweep, in the upstream direction, for each time interval Δt.

Friction-Slope Predictor. The friction slope, S_f, or longitudinal energy gradient, can be computed using any valid flow resistance relationship. It is common practice to use the Manning formula to express S_f as an explicit function of the flow and average streambed characteristics:

$$S_f = n^2 Q^2 R_h^{-4/3} A^{-2} \qquad (5)$$

in which

n = Manning roughness coefficient, and
R_h = hydraulic radius.

We know, however, that for alluvial streams, friction losses should include bed form resistance. In that case the simple equation 5 should be replaced by an implicit relationship between S_f and flow and streambed characteristics. In fact, such an implicit relationship turns out to be a system of one or more non-linear algebraic equations (Brownlie, 1981) from which it is impossible to extract the friction slope as an explicit function of other hydraulic parameters. In that case, the friction slope relationship(s) must be added to equations 3-4 and solved iteratively. This iterative requirement is avoided in this study for the sake of computational expediency, and the friction slope is obtained from equation 5 assuming a constant roughness coefficient.

Sediment Discharge Predictor. The Yang formula was selected to compute total bed material discharge. This formula yields results that compare quite well with measurements in the sand-size range (Alonso et al., 1980; Brownlie, 1981). Yang (1973) based his formula on the premise that total load is dominated by the rate of potential energy expenditure per unit weight of water. He used this concept and dimensional analysis to derive his formula, the coefficients of which were determined from a large set of laboratory data. Yang's formula can be expressed in dimensionless form (Alonso et al., 1980) as:

$$\Phi = \Theta_{50}^{1/2} Z_{50} \left(V/u_* \right) \left(10^{\sigma-6} / S_g \right) \qquad (6)$$

in which

S_g = specific gravity of bed material,
u_* = bed shear velocity,
Z_{50} = h/D_{50}
= relative grain roughness based on D_{50} bed material size
Θ_{50} = $(u_*)/[(S_g-1)gD_{50}]$
= mobility number,

Φ = $q_s / [(S_g-1)g(D_{50})^3]^{1/2}$
= Einstein's transport function, and
$\tilde{\sigma}$ = non-linear function of grain Reynolds number and specific stream power.

CHANGES IN LONGITUDINAL BED PROFILE

The depth of bed degradation or aggradation in a subreach of length Δx during a time interval Δt is calculated by applying the sediment continuity equation between the cross sections bounding the sub-reach. In its most general form sediment continuity is given by (Chen. 1973):

$$\frac{\delta Q_s}{\delta x} + \frac{\delta}{\delta t}\left(AC_s \right) + (1 - \lambda)\frac{\delta}{\delta t}(Bz) = 0 \qquad (7)$$

where

Q_s = the total sediment discharge, in units of volume per unit time;
C = volumetric concentration of suspended sediment in the water per unit length of channel, and
λ = the effective porosity of the sediment material stored in the active bed layer.

In most cases of practical interest the second term in equation 7 is negligible in relation to the other terms. Introducing $q_s = Q_s / [B(1-\lambda)]$, expanding the differential terms, and rearranging yields:

$$\frac{\delta z}{\delta t} + \frac{\delta^{q_s}}{\delta x} + \frac{z}{B}\frac{\delta B}{\delta t} + \frac{q_s}{B(1-\lambda)}\frac{\delta B}{\delta x} = 0 \qquad (8)$$

Introducing a further assumption that channel width adjustment proceeds slowly in time and space, equation 8 reduces to the form commonly used in one-dimensional sediment routing:

$$\frac{\delta x}{\delta t} + \frac{\delta^{q_s}}{\delta x} = 0 \qquad (9)$$

Obviously, the use of equation 9 requires the use of small time intervals during the integration process. Using large time steps could result in rapid retreat of the banks between consecutive time steps. This would not only violate the condition of slow width variations implicit in equation 9, but might also lead to missing the exact time when the stream banks reach an unstable condition. On the other hand, the need to restrict time steps to small values enables the use of explicit numerical schemes to integrate equation 9. Accordingly, the following solution follows from the modified Lax-scheme developed by deVries (1971).

Introducing the notation $x_j = j\Delta x$, $t^n = n\Delta t$, equation 9 is solved using the following forward, central, finite-difference scheme:

$$z_j^{n+1} = \frac{\alpha}{2}\left(z_{j-1}^n + z_{j+1}^n \right) - (1-\alpha)z_j^n +$$

$$\frac{\Delta t}{2\Delta x}\left(q_{s,j-1}^n - q_{s,j+1}^n \right) \qquad (10)$$

where α is a time-dependent coefficient which is constant for every x. deVries (1971) has shown that equation 10

leads to the following second-order approximation of equation 9:

$$\frac{\delta z}{\delta t} + \frac{\delta q_s}{\delta x} = \frac{(\Delta x)^2}{2\Delta t}\left[\alpha - C_R^2\right]\frac{\delta^2 z}{\delta x^2} \quad (11)$$

in which

$C_R^2 = c_b \Delta t / \Delta x$
  = the local grid Courant number, and

c_b = celerity of bed perturbations.

The above scheme is consistent with equation 9 because as $\Delta x \to 0$ (leaving $\Delta x/\Delta t$ constant) the differential equation is obtained from the difference equation. Following the procedure of von Neumann, the condition for numerical stability of deVries' scheme is shown to be:

$$C_R^2 < \alpha \leq 1 \quad (12)$$

The right-hand side of equation 11 introduces numerical dispersion. This can be avoided by making the term within brackets as small as possible.

An important corollary of deVries' work follows from the fact that in many instances of practical interest the sediment transport relation can be proximated by the functional form $q_s = f(V)$. In this case, deVries showed that the system of equations 3-5, 9, 11 yields:

$$\frac{c_b}{V} = \frac{1}{b}\frac{df}{dV}\frac{1}{1-F_r^2} \quad (13)$$

where F_r is the flow Froude number. In many U.S. sand-bed rivers (Vanoni, 1975) f can be approximated by aV^b with $a \ll 1$ and $3 < b < 5$. Hence, it readily follows from equation 13 that in subcritical flows with small Froude numbers, the propagation of bed deformations is small in relation to the propagation of flood waves. This conclusion enables the uncoupled approach adopted in the present study.

STREAMBANK EROSION RELATIONS

Processes of bank retreat due to lateral erosion and bed degradation are analyzed in this section. As discussed earlier in the article lateral erosion increases the active bed width resulting in steepening of the banks. Bed degradation also increases the bank height, which further decreases the stability of the banks. Lateral erosion and mass failure processes depend on bank material properties, bank geometry, bed material characteristics, and flow conditions. This section first discusses relationships used to simulate the rate of lateral erosion of stream banks. Bank stability relationships are then presented to compute the height at which a cohesive bank becomes unstable, and the expected angle between the failure plane and the horizontal.

Figure 2(a) shows the geometry of a steep streambank before failure. The contour ACDEF is the bank profile present before lateral erosion and bed degradation. H is the initial bank height above the active bed, B is the initial active bed width, and i is the bank angle prior to failure. Figure 2(b) depicts the bank profile after failure in which H' is the bank height after failure, and β is the angle of the plane of failure.

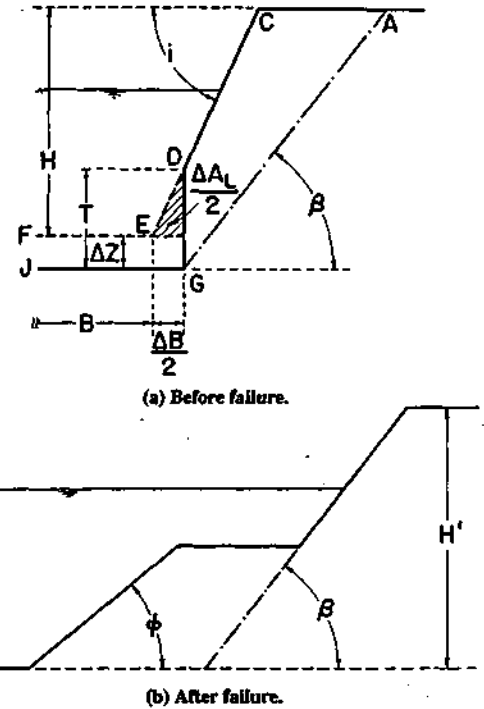

(a) Before failure.

(b) After failure.

Figure 2–Definition sketch of streambank configuration.

The amount of lateral bank erosion in any given cross-section is determined by comparing the maximum tractive force exerted by the flow on the bank, τ_{max}, to the critical shear stress, τ_c, at which the bank material begins to move. Once this threshold is exceeded, the bank toe is assumed to retreat at a constant rate resulting in an increase ΔB of the active bed width [fig. 2 (a)]. The maximum tractive force acting on the bank is estimated from:

$$\tau_{max} = C_\tau \gamma_w R_h S_f, \quad (14)$$

in which the coefficient C_τ is determined following Olsen and Florey (1952), and γ_w = the specific weight of water. The volumetric rate at which bank material is depleted by lateral erosion is determined from:

$$\frac{\delta A_L}{\delta t} = \frac{E_L}{\gamma_s}\delta(\tau_{max}, \tau_c; 0) \quad (15)$$

where

A_L = unit cross-sectional area, in m³,

γ_s = the bulk specific weight of bank material, in kN/m³,

δ = the Kronecker delta such that
  $\delta = 1$ when $\tau_{max} > \tau_c$, and $\delta = 0$, otherwise,

E_L = a coefficient of bank erodibility, expressed in kN min/m², which can be either treated as a calibrating parameter or estimated from the relations proposed by Arulanandan et al. (1980).

Similarly, τ_c can be either specified or evaluated from the database compiled by Arulanandan et al. (1980).

According to Arulanandan et al., τ_c can range from very small values to about 100 dynes/cm^2 depending on soil and pore fluid properties. Assuming that both banks erode at the same rate, the change in active bed width is:

$$\Delta B = \left(4\Delta A_L \Big/ \tan i \right)^{1/2} . \qquad (16)$$

in which

$$\Delta A_L = \frac{\delta A_L}{\delta t} \Delta t . \qquad (17)$$

The volume of eroded toe material is deducted from the potential degradation depth predicted by equation 10 to yield the effective degradation depth:

$$\Delta Z = \frac{\left[B^n \left(z^{n+1} - z^n \right) - 0.25 \left(\Delta B \right)^2 \tan i \right]}{\left(B^n + \Delta B \right)} \qquad (18)$$

in which B^n and z^n are the bed width and elevation at the time level $t = n\Delta t$. The bank height at the new time level is:

$$H^n = H + \Delta z \qquad (19)$$

and as a result of lateral erosion and bed degradation, the bank takes a steeper profile as shown by the contour ACDGJ in figure 2(a). Bank stability relations for this specific bank geometry are presented below. The height T of the vertical cut created by lateral erosion and bed degradation follows from the geometry of the bank toe after failure [fig. 2 (a)]:

$$T - \Delta z = \frac{\Delta B}{2} \tan i , \qquad (20)$$

and using equation 17:

$$T = \Delta z + \left(\Delta A_L \tan i \right)^{1/2} \qquad (21)$$

where ΔA_L and Δz are obtained from equations 17 and 18, respectively. For the sake of computational efficiency, two additional simplifying hypotheses are introduced:

- Since most eroding stream banks are very steep, it is assumed that the bank fails along an almost planar slip surface through the bank toe [plane AG, fig. 2 (a)].
- Factors such as plant roots, soil saturation, and seepage are not considered explicitly in the analysis, although they may be incorporated implicitly into the parameters used to represent the bank material characteristics.

The approximation of the failure surface by a plane is acceptable for steep banks. As mentioned above, the Culmann method can be used to analyze plane shear failure and predict maximum (critical) bank height for steep bank slopes. Although this method is approximate in that it is a

total stress analysis that does not takes into account pore water pressure in the case of poorly drained soils, it gave reasonable results when applied to steep eroding stream banks in loessial material (Little, Thorne and Murphy, 1982).

Here, the Culmann method is applied to the analysis of the failure geometry shown in figure 2(a). Resolving the equilibrium between the driving and resisting forces acting on the failure plane leads to equations for the critical bank height, the angle the failure plane makes with the horizontal, and the mass of the failure block. The tangential driving force acting on the failure plane is:

$$T_D = W \sin \beta \qquad (22)$$

where W is the weight of the failure block given by:

$$W = \frac{\gamma_s}{2} \left[\frac{H^2}{\tan \beta} - \frac{(H-T)^2}{\tan i} \right] \qquad (23)$$

The tangential resisting force acting on the failure plane is:

$$T_R = c\,AG + N \tan \phi \qquad (24)$$

where

c = soil cohesion,
AG = $H/\sin\beta$ is the length of the failure surface,
N = $W\cos\beta$ is the component of the failure-block weight normal to the failure surface, and
ϕ = angle of internal friction. Hence,

$$T_R = \frac{c\,H}{\sin \beta} + W \cos \beta \tan \phi . \qquad (25)$$

Within the framework of limit equilibrium analysis, bank failure is reached when $T_D = T_R$. Equating equations 22 and 25, using equation 23, and rearranging terms leads to the following quadratic equation:

$$C_2 H_c^2 + C_1 H_c + C_0 = 0 \qquad (26)$$

in which

$$C_2 = \qquad (27a)$$
$$\frac{\gamma_s}{2} \left(\cos \beta - \frac{\cos^2 \beta \tan \phi}{\sin \beta} + \frac{\cos \beta \tan \phi}{\tan i} - \frac{\sin \beta}{\tan i} \right),$$

$$C_1 = \gamma_s T \left(\frac{\sin \beta}{\tan i} - \frac{\cos \beta \tan \phi}{\tan i} - \frac{c}{\sin \beta} \right), \qquad (27b)$$

$$C_0 = \frac{\gamma_s T^2}{2} \left(\frac{\cos \beta \tan \phi}{\tan i} - \frac{\sin \beta}{\tan i} \right), \qquad (27c)$$

and H_c is the critical bank height, that is, the bank height at failure. H_c is obtained by selecting the smallest positive root of equation 26. Solution of this equation requires

knowledge of the angle of the failure plane when the critical configuration is reached. Taylor (1948) and Spangler and Handy (1973) have shown that the critical angle, β_c, corresponds to the plane of fully developed cohesion on which the ratio $c/(\gamma_s H_c)$ is a maximum. Hence, β_c is determined as follows. Multiplying equation 26 by (2 $\sin \beta/\gamma_s H_c^2$), putting $m = T/H_c$, and rearranging terms yields:

$$2 \tan i \left(\frac{c}{\gamma_s H_c} \right) =$$

$$(1 - m)^2 \left(\cos \beta \sin \beta \tan \phi - \sin^2 \beta \right) + \quad (28)$$

$$\cos \beta \sin \beta \tan i - \cos^2 \beta \tan \phi \tan i$$

Differentiating equation 28 and equating the result to zero gives:

$$\frac{\partial}{\partial \beta} \left(\frac{c}{\gamma_s H_c} \right) =$$

$$(1 - m)^2 \left(\cos 2\beta \tan \phi - \sin 2\beta \right) + \quad (29)$$

$$\cos 2\beta \tan i + \sin 2\beta \tan i \tan \phi = 0$$

Solving this expression for β yields the following expression for the critical failure angle:

$$\tan 2 \beta_c = \frac{(1-m)^2 \tan \phi + \tan i}{(1-m)^2 - \tan \phi \tan i} \quad (30)$$

It can be shown that equations 26 and 30 reduce to the expressions obtained by Lohnes and Handy (1968) for the case of non-eroded bank toes (i.e., $m = 0$).

COMPUTATIONAL PROCEDURE

The model presented above is implemented using the following sequence:

1. At each time level $t = n\Delta t$ the longitudinal stage profile and potential bed degradation are computed by solving the system of equations 3-6 and 10;

2. The effective bed degradation, the new bank height, and the height of the vertical cut created by lateral erosion are computed at each cross-section using equations 15-19 and 21;

3. In those cross-sections where $H' < H_c$ (equations 26-30) degradation calculations proceed to the next time level without incorporating bank caving;

4. When H' exceeds H_c the bank is unstable and bank failure must be taken into account. Equation 23 is used to compute the mass of failed bank material. This fallen mass comes to rest at the foot of the bank standing at the angle of repose ϕ [fig. 2 (b)].

5. The fallen bank material is removed by flow entrainment during subsequent time steps. During this phase of basal removal, sediment transport capacity is satisfied by the fallen material and bed degradation is not

assumed to take place.

6. After the fallen material is depleted by basal erosion, the bank stands at the new slope given by equation 30, having retreated on each side the distance $\Delta B/2$ at the toe. Subsequent bed degradation profiles and bank failures are computed by repeating steps (1)-(5).

MODEL APPLICATIONS

The model developed above is applied herein and it is demonstrated using two specific cases. The first application is to the simulation of degradation data collected in a laboratory flume with fixed walls. The second application is a study of the influence of streambank instability on the propagation of bed degradation.

BED DEGRADATION STUDY

This section describes a computer simulation of streambed degradation measurements carried out at Colorado State University. Suryanarayana (1969) conducted a series of degradation experiments in a 0.61-meter wide, 18-meter long, rectangular flume using fairly uniform sands. Dry sand was fed by an upstream feeder, and a collecting tank was installed at the end of the flume to trap the effluent sediment. Water and sediment were supplied at a constant rate, and the flow was continuously recirculated until the average bed and water surface slopes approached equilibrium. After attaining initial equilibrium, the sediment feeder was switched off, marking the beginning of the bed degradation process. Subsequent changes in bed and water surface elevations were measured at 0.60-meter longitudinal intervals, and at gradually increasing time intervals as the degradation rate decreased. The degradation run conducted at a flow rate of 0.0116 m^3/sec, an initial flow depth of 0.039 m, and a uniform sand bed with a $D_{50} = 0.45$ mm was selected for the present verification test. The weight of the sediment mass accumulated in the receiving tank was continuously monitored and from these readings the sediment transport rate was computed. The measured sediment discharge was found to vary as a power-law function of the average flow velocity as:

$$q_s = 0.000585 \, V^{3.88} \quad (31)$$

with q_s in m^3/sec/m, and V in m/sec. The longitudinal water surface and bed profiles measured at the onset of the run and at 1.33, 3.75, 6, and 10 hours into the run are displayed in figure 3.

The degradation experiment was simulated assuming vertical, non-erodible channel walls. The Manning roughness for the initial uniform, equilibrium flow condition was estimated at $n = 0.014$. This value was used throughout the simulation. The measured sediment discharge relationship (eq. 31) was used in lieu of Yang's transport formula. Using equation 31 in equation 13 we find that the ratio c_b/V is equal to 0.011. This confirms the validity of the uncoupled approach to sediment routing. The selected computational-grid sizes are $\Delta x = 0.508$ m and $\Delta t = 30$ seconds, which yield a grid Courant number $C_r = 0.64 < 1$. The longitudinal stage and bed profiles predicted by the model are shown in figure 4. The shape of
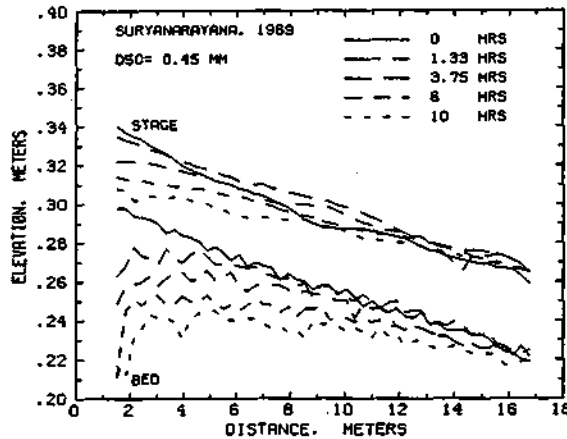
Figure 3–Longitudinal stage and bed profiles measured during degradation experiment (Suryanarayana, 1969).

the computed profiles are in good agreement with the measured profiles over most of the channel length. The differences observed near the upstream end are attributed to three-dimensional flow disturbances induced by the channel inlet in the laboratory flume. It is apparent from these results that at any given time the degradation decreases with distance. As bed material is scoured and entrained by the flow, the sediment demand decreases resulting in decreasing entrainment at subsequent points down the channel.

The model tends to overestimate degradation rates, particularly at longer times. It is speculated that this is the result of differences between the actual local transport capacity of the flow and sediment discharge rate predicted by the rating formula. The bed profiles shown in figure 3 suggest that a considerable portion of the energy available for transport was being dissipated on form drag of the sand bed dunes. This effect is less noticeable near the end of the flume where the sediment discharge was measured. Moreover, the use of a constant Manning coefficient in the simulations is not an adequate representation of the obvious increase in roughness with time exhibited by the measured bed profiles. These observations suggest that
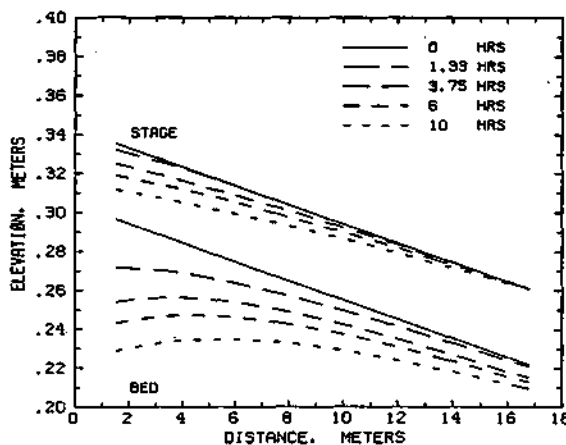

Figure 4–Simulated longitudinal stage and bed profiles.

predicted transport rates exceed actual local transport capacities, particularly in the upper reaches of the flume.

STREAM DEGRADATION WITH BANK RETREAT

In this section the model is applied to study the effect of streambed degradation on the stability of stream banks, and the impact of bank-sediment yield and channel widening on the degradation rate. Realistic hypothetical data are used in the simulations because real data of sufficient detail are not available to the authors. A hypothetical alluvial stream with cohesive banks and an erodible sand bed was selected to demonstrate the capabilities of the model.

The channel is 1500 meter long with an initial bed slope of 0.001. The initial cross-sectional shape is trapezoidal with a 25-meter wide bottom and a bank height of 2.70 meters. The right bank (looking downstream) has a 75-degree slope, while the left bank has a less steep slope of 28 degrees. Bed material is coarse sand with a $D_{50} = 0.45$ mm, and characteristics of the bank material are: $\gamma_s = 20$ kN/m^3, c= 7 kN/m^2, $\phi = 20$, and $\tau_c = 50$ dynes/cm^2. Clear water is assumed to enter the channel at a steady rate of 25 m^3/sec. The initial channel geometry and bank material properties were selected to ensure failure of the right bank shortly after the onset of the simulation run. In this experiment channel roughness was selected to attain a bankful stage at the specified discharge. Similarly, the erodibility coefficient was adjusted to yield an average rate of lateral erosion of about 20 cm/day. This small value of erosion by flow was selected to avoid masking the display of retreat by bank failure.

Cell sizes $\Delta x = 50$ meters and $\Delta t = 10$ minutes were used for the computational grid. In this test the average friction slope and flow depth remain of the order of 10^{-3} and 2.5 meters, respectively, and Yang's formula can be approximated by:
Introducing this relationship in equation 13 yields a bed

$$q_s = 0.00004 \, V^{2.40} \qquad (32)$$

celerity and grid Courant number of 7×10^{-5} m/sec and 8.4×10^{-4}, respectively. These values confirm that test parameters satisfy the conditions for numerical stability and hydraulic uncoupling. The computations were carried out for a period of three days and two cases were considered: (a) the active-bed width is constant and the banks are assumed stable and non- erodible; and (b) the channel width varies due to bank erosion and failure.

Figure 5 shows the effect of bank retreat on bed degradation. The final bed profile for the case when the banks are erodible is compared to the profile resulting when the channel is assumed to have constant width. After three days the upstream bed level decreased 2.19 meters when the channel width was constant, compared to 2.03 meters when the channel had erodible banks; a difference of 8% over the three-day period. A simple extrapolation of this result to longer periods serves to highlight the need to take into consideration the effect of bank retreat in bed degradation predictions. This reduction in bed degradation is explained by the sediment contributed by the banks partially satisfying the sediment-starved stream, thereby reducing the amount of sediment taken from the bed. It is to be noted, however, that the ability of the streambed to adjust to the upstream and lateral sediment supply is a
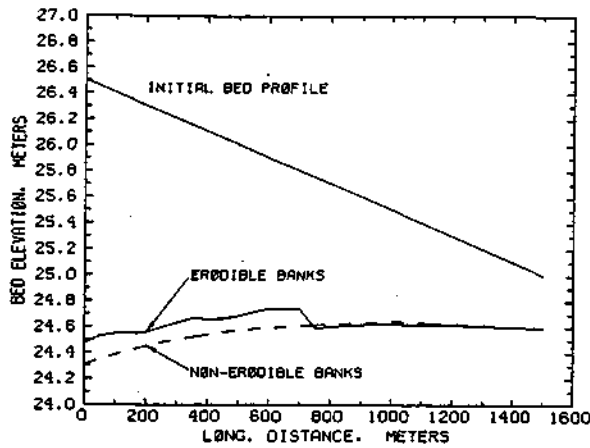
Figure 5–Bed degradation profiles with and without erodible banks.

consequence of the unrestrained supply of disturbed material. Whenever bank erosion takes place along a degrading stream carrying non-uniform bed material, the coarse fractions would move as bed load leading to either partial or total armoring. This condition may operate to further limit bed degradation.

The impact of bed degradation on channel widening is illustrated in figure 6, which shows the evolution of a cross-section located 150 meters from the channel entrance. In this figure, the left bank profiles computed for
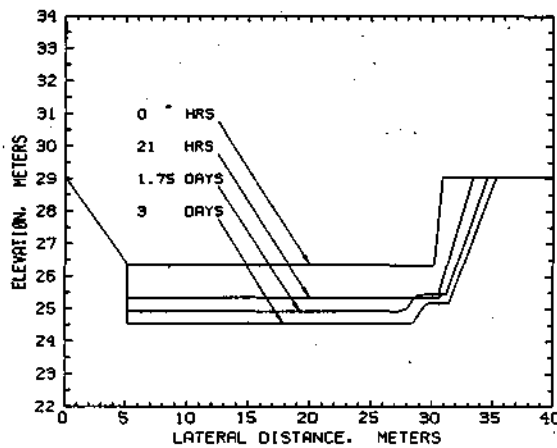

Figure 6–Evolution of channel cross-section at x = 150 meters.

different times are overlapped to facilitate graphical comparison. Bed degradation is very active initially, resulting in significant right bank retreat after only 21 hours. As the channel widens, the rate of bank retreat tends to diminish, and by the end of the simulation the top width has reached 35.3 meters, an increase of 14% over the original width. During the same period the left bank remains stable and is only affected by lateral erosion. The bank debris not removed by the flow are seen left standing at the base of the right bank.

Figure 7 is a three-dimensional view of the channel as seen by an observer located upstream, after three days of continuous eroding flow. Several interesting points can be noted in this figure. In spite of a limited graphical resolution, the small but noticeable erosion of the left bank is apparent. Right-bank debris left standing by the flow can be observed at several cross-sections. As expected, the rate of bank retreat decreases downstream as the amount of bed degradation decreases. The failure front is seen to have moved half the downstream distance during the three-day period. This rapid rate of advance might stem from two characteristics of the present scheme. One is the assumption of homogeneous bank material over the entire channel length. Another is the inability of the method of limit equilibrium to recognize that real bank material may fail slowly along the streambank rather than simultaneously at all points once critical conditions are reached. Assessing the severity of this behavior must wait until the model can be field tested.

SUMMARY AND CONCLUSIONS

Streambank retreat is the result of erosion by flow and mass failure. In this article, the physical processes of erosion and mass failure which operate on alluvial streams have been discussed. A known-discharge, one-dimensional model of stream morphology which takes into consideration coupling of bed and bank processes has been presented. The analysis is restricted to straight channels. Steep, drained, homogeneous cohesive banks are considered, and the streambed is assumed to degrade within a uniform cohesiveless alluvium. Other important factors such as roots and saturated soil conditions are not included, although they can be readily incorporated in the proposed framework of the model. Bank stability is computed using a limiting-equilibrium analysis of plane-slip failure, which is the prevalent failure mode for steep, cohesive banks. This analysis is coupled to changes in streambank geometry resulting from lateral erosion and

Figure 7–Channel shape after three days of continuous eroding flow.

near-bank bed degradation.

Application of the model to a laboratory experiment shows that the model tends to somewhat overestimate degradation rates. It is concluded that these deviations stem from simplifications introduced for computational expediency, which can be readily relaxed when needed. In spite of the observed differences, it is apparent that the test verifies the behavior of the bed degradation submodel.

Analysis of a more complex scenario incorporating bed degradation in the presence of bank retreat demonstrates the importance of considering streambank erosion when predicting the extent of bed degradation. This example clearly illustrates the potential usefulness of the model as a tool for analysis of bank instability due to lateral erosion and/or bed degradation.

REFERENCES

Alonso, C.V., Neibling, W.H. and G.R. Foster. 1981. Estimating sediment transport capacity in watershed modeling. *Transactions of ASAE* 24(5): 1211-1220, 1226.

Alonso, C.V. and S.T. Combs. 1986. Channel width adjustment in straight alluvial channels. In *Proceedings of the Fourth Federal Interagency Sedimentation Conference* II:5-31 to 5-40.

Arulanandan, K., E. Gillogley and R. Tully. 1980. Development of a quantitative method to predict critical shear stress and rate of erosion of natural undisturbed cohesive soils. Tech. Report GL-80-5. U.S. Army Engineers, Waterways Experimentation Station, Vicksburg, MS.

ASCE Task Committee on Sedimentation. 1968. Erosion of cohesive sediments. *J. Hydraul. Div. ASCE* 94(HY4): 1017-1047.

Bathurst, J.C. 1979. Distribution of boundary shear stresses in rivers. In *Adjustments of the Fluvial System*, eds. D.D. Rhodes and G.P. Williams, 95-116. Dubuque, IA: Kendall/Hunt Publishing Co.

Bowie, A.J. 1982. Investigations of vegetation for stabilizing eroding stream banks. *Transactions of ASAE* 25(6): 1601-1611.

Brownlie, W.R. 1981. Prediction of flow depth and sediment discharge in open channels. Report KH-R-43A, W.M. Keck Laboratory of Hydraulics and Water Resources, Calif. Inst. of Tech., Pasadena.

Carson, M.A. and M.J. Kirby. 1972. *Hillslope Form and Processes*. London: Cambridge University Press.

Chen, Y.H. 1973. Mathematical modeling of water and sediment routing in natural channels. Ph.D. diss., Department of Civil Engineering, Colorado State University, Fort Collins.

Falcon, M.A. and J.F. Kennedy. 1983. Flow in alluvial-river curves. *J. Fluid Mech.* 133: 1-16.

Frydman, S. and D.H. Beasley. 1976. Centrifugal modeling of river bank failure. *J. Geotech. Engr. Div. ASCE* 102(GT5): 395-409.

Galay, V.J. 1983. Causes of river bed degradation. *Water Resources Research* 19(5): 1057-1090.

Graf, W.H. 1971. *Hydraulics of Sediment Transport*. London: McGraw-Hill Book Co.

Ikeda, S. and G. Parker. *River Meandering*. Water Resources Monograph No. 12, American Geophysical Union.

Little, W.C., C.R. Thorne and J.B. Murphey. 1982. Mass bank failure analysis of selected Yazoo basin streams. *Transactions of ASAE* 25(5): 1321-1328.

Lohnes, R.A. and R.L. Handy. 1968. Slope angles in friable loess. *J. of Geology* 76: 247-258.

Odgaard, A.J. and M.A. Bergs. 1988. Flow processes in a curved alluvial channel. *Water Resources Research* 24(1): 45-56.

Olsen, O.J. and Q.L. Florey. 1952. Sedimentation studies in open channels: Boundary shear and velocity distribution by membrane analogy, analytical and finite-difference methods. Laboratory Report Sp-34, U.S. Bureau of Reclamation.

Osman, A.M. and C.R. Thorne. 1988. Riverbank stability analysis. I: Theory. *J. Hydraul. Eng. ASCE* 114(2): 134-150.

Pizzuto, J.E. 1987. A k-ε turbulence model for straight alluvial channels with laterally varying cross-sections. *EOS Trans. AGU* 69: 1268.

Raudkivi, A.J. 1976. *Loose Boundary Hydraulics*, 2nd ed. London: Pergamon Press.

Simons, D.B. and F. Senturk. 1976. *Sediment Transport Technology*. Colorado: Water Resources Publications.

Spangler, M.G. and R.L. Handy. 1973. *Soil Engineering*, 3rd ed. New York: Intext Educational Publishers.

Sullivan, R.A. 1972. Behaviour of a wharf affected by river fluctuations. *J. Soil Mech. and Found. Div. ASCE* 98(SM9): 939-954.

Suryanarayana, B. 1969. Mechanics of degradation and aggradation in a laboratory flume. Ph.D. diss., Dept. of Civil Engineering, Colorado State University, Fort Collins.

Taylor, D.W. 1948. *Fundamental of Soil Mechanics*. New York: John Wiley & Sons.

Thorne, C.R. 1982. Processes and mechanisms of river bank erosion. In *Gravel-bed Rivers*, ed. R.D. Hey, J.C. Bathurst, and C.R. Thorne, 227-259. New York: John Wiley & Sons Ltd.

Thorne, C.R. and N.K. Tovey. 1981. Stability of composite river banks. *Earth Surface Processes and Landforms* 6:469-484.

Turnbull, U.J., M. Krinitzsky and F.J. Weaver. 1966. Bank erosion in soils of the Lower Mississippi Valley. *J. Soil Mech. and Engr. Div. ASCE* 92: 121-136.

Vanoni, V.A., ed. 1975. *Sedimentation Engineering*. ASCE Manual No. 54. New York: American Society of Civil Engineers.

Vries, M. de. 1971. Solving river problems by hydraulic and mathematical models. Publication No. 76II, Delft Hydraulics Laboratory.

Yang, C.T. 1973. Incipient motion and sediment transport. *J. Hydraul. Div. ASCE* 99(HY10): 1679-1704.

Food and Process Engineering Institute Section

Riverbank Stability Analysis. I: Theory

By Akode M. Osman[1] and Colin R. Thorne,[2] Affiliate Member, ASCE

Abstract: In this paper, a slope stability analysis for steep banks is used in conjunction with a method to calculate lateral erosion distance, to predict bank stability response to lateral erosion or bed degradation. The failure plane angle, failure block width, and volume of failed material per unit channel length may be calculated for the critical case. These parameters define the bank geometry following failure and form the starting point for subsequent analyses. The calculation procedure is illustrated by a worked example. Following mass failure slump, debris accumulates at the bank toe. The debris is removed by lateral erosion prior to further oversteepening or degradation generating further mass failures. Any process-based model for channel width adjustment must account for the combined effects of lateral erosion and mass instability in producing bank instability. The approach adopted here represents a marked improvement over earlier work, which does not account for changes in bank geometry due to lateral erosion prior to mass failure. The engineering applications are presented in a companion paper.

Introduction

Instability of cohesive riverbanks due to bed degradation and lateral erosion is analyzed herein. These are the two processes that most commonly cause bank instability. The process of lateral erosion increases the bed width of the channel and results in steepening of the bank, which reduces its stability. Bed lowering increases the bank height, which also decreases stability. The relative amounts of vertical and lateral erosion are a function of bank material properties, bank geometry, type of bed material, and the flow characteristics.

The stability of the bank with respect to mass failure depends on soil properties and bank geometry. Soil shear strength is proportional to cohesion c' and angle of friction ϕ' (Taylor 1948; Lamb and Whittman 1969). The stability of the banks increases with an increase in c' and ϕ'. An increase in the specific weight γ, bank height H, or the slope angle i, results in decreasing stability of the bank since the driving force that causes bank failure is directly proportional to γ, H, and i. The stability relations developed here on the basis of these parameters can be used to predict the height and the bank geometry at which the banks become unstable due to bed degradation, lateral erosion, or a combination of both these processes.

First, we present a method of using the results of experiments on the erosion of cohesive soils to estimate the rate of lateral erosion of riverbanks and the change in the channel bed width. Second, bank stability relations are derived to predict the critical height, the angle between the

[1]Lect., Dept. of Civ. Engrg., Univ. of Khartoum, Khartoum, Sudan.

[2]Visiting Sci., Hydr. Lab., U.S. Army Wtrwys. Exper. Sta., Vicksburg, MS 39180; on leave from, Dept. of Geography and Earth Sci., Queen Mary Coll., Univ. of London, London E14NS, U.K.

failure surface and the horizontal, and the width and volume of the failure block for steep cohesive riverbanks. Third, the computation sequence and a worked example of the method are presented. The implications of the analysis are briefly discussed and the main conclusions are summarized.

In the companion paper to this one, a modeling technique based on these processes and mechanisms of width adjustment is developed to study the following: (1) The effects of channel widening and bank-sediment contribution on flow energy, stream power, and the rate and extent of bed lowering during degradation; and (2) the influence of outer bank stability on bed topography in a bendway.

Estimating Lateral Erosion of Cohesive Riverbanks

For a given fluid shear stress, the rate of lateral erosion has been shown to depend largely on the physical and chemical makeup of the soil, and the types and amounts of salts in the pore and eroding fluids (Arulanandan et al. 1980). Increasing the clay content or decreasing sodium ions in the soil increases the soil's shear resistance to erosion. Conversely, reducing the clay content or the level of salt in the eroding water decreases the shear resistance of the soil to erosion. If the fluid shear stress, τ, does not exceed the critical shear stress, τ_c, at which the soil particles are entrained, the soil remains stable.

A method to calculate the rate and amount of lateral erosion of a cohesive bank material was developed during laboratory work at the Waterways Experiment Station, at Vicksburg, Mississippi (Arulanandan et al. 1980). The first step is to determine the critical shear stress for the undisturbed soil as a function of sodium adsorption ratio (SAR), pore fluid salt concentration (CONC), and the dielectric dispersion $\Delta\varepsilon$, as shown in Fig. 1. The rate of change of erosion with shear stress $\dot{R}$, can be determined as a function of the critical shear stress, τ_c, as shown in Fig. 2. $\dot{R}$ is defined as the slope of the curve of the rate of erosion, R, versus the critical shear stress, τ_c. Assuming a linear relationship between R and τ once the critical soil shear stress to erosion is surpassed, lateral erosion distance is determined as follows:

1. Determine the average shear stress, $\tau = \gamma_w R_h S$, where γ_w = specific weight of water, R_h = hydraulic radius, and S = energy slope. To be comparable to τ_c, τ should be expressed in dynes/cm^2.

2. For an undisturbed soil sample, determine the sodium adsorption ratio (SAR), pore fluid salt concentration (CONC), the dielectric dispersion, $\Delta\varepsilon$, and the soil unit weight, γ.

3. From Fig. 1, determine the critical shear stress, τ_c (dynes/cm^2).

4. Check whether the flow shear $\tau \geq \tau_c$. If not, no soil erosion will take place. If so, proceed to step 5.

5. Determine the initial rate of soil erosion R from

$$R = \tau_c * \dot{R} = 223 \times 10^{-4} \, \tau_c e^{-0.13\tau_c} \, (\text{gm/cm}^2 \cdot \text{min}) \quad \cdots \cdots \cdots (1)$$

6. The initial lateral bank erosion rate is given by

$$dB = \frac{R}{\gamma} \, (\text{m/min}) \text{ per unit area} \quad \cdots \cdots \cdots (2)$$
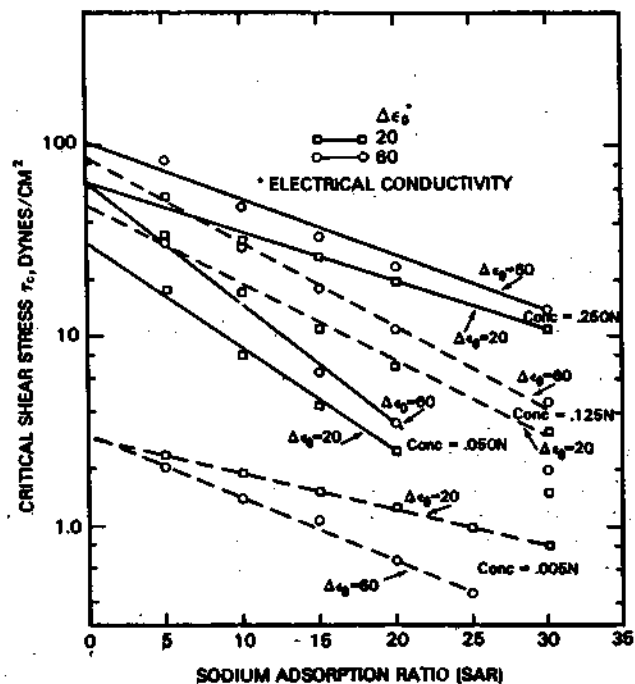
FIG. 1. Critical Shear Stress τ_c versus SAR for Different Soil Salt Concentrations and Different Dielectric Dispersion $\Delta\epsilon_c$ Values (after Arulanandan et al. 1980)

where γ = the soil unit weight.

7. The rate of soil erosion, R, is assumed to have an approximately linear increase with shear stress once the critical shear stress is surpassed. Consequently, the actual erosion rate, dW, is

$$dW = dB * \left(\frac{\tau - \tau_c}{\tau_c}\right) \text{ (m/min)} \quad \dots \dots \dots \dots \dots \dots \dots \dots \dots \text{(3)}$$

and if the duration of the flow shear, τ, is $\Delta\tau$ (min), then the lateral erosion distance during this time is

$$\Delta W = dW * \Delta\tau(\text{m}) \quad \dots \dots \dots \dots \dots \dots \dots \dots \dots \dots \dots \dots \dots \text{(4)}$$

If only one bank is being eroded, then the change in bed width is given by Eq. 4. For a reach with both banks eroding, the change in the bed width is twice the value of Eq. 4.

The critical shear stress, τ_c, estimated in step 3 from Fig. 1, represents a lower bound for the tested soil sample because it is based on distilled water as the eroding fluid. If the eroding fluid actually contains dissolved salts, as is normal for rivers, the critical shear stress may be higher. If the lateral erosion distance ΔW turns out to be unrealistic and does not agree with field observations, then a calibration factor can be used to adjust the predicted value. Such a factor can be estimated using historical maps or

136
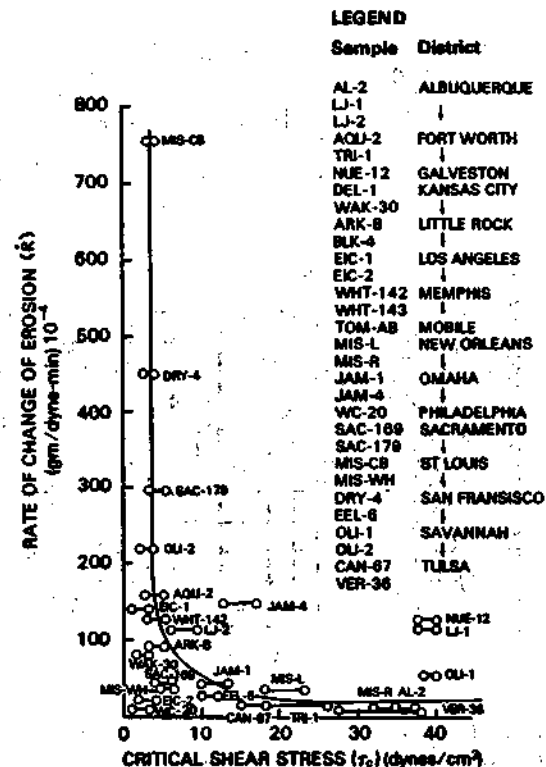
FIG. 2. Rate of Change of Erosion Rate, R versus Critical Shear Stress τ_c, for Undisturbed Soils Tested in Flume Using Distilled Water as Eroding Fluid (after Arulanandan et al. 1960)

field data collected using the methods described by Wolman (1959), Hooke (1979), and Thorne (1981).

Explanation of Step 5

Fig. 2 shows that when the soil shear resistance to erosion τ_c is less than 20 dynes/cm^2, the decrease in the rate of change of erosion R with the increase of τ_c is given by the following negative exponential relation:

$$\dot{R} = 223 \times 10^{-4} e^{-0.13\tau_c} \text{ gm/dyne} \cdot \text{min} \quad \text{(for } \tau_c > 6 \text{ dynes/cm}^2\text{)} \quad \dots \dots \text{(5)}$$

where τ_c is in dynes/cm^2. When τ_c is greater than 20 dynes/cm^2, $\dot{R}$ is a constant equal to 28 (gm/dyne · min). This indicates that even when the bank is stiff and resistive to erosion, $\dot{R}$ is constant, which seems illogical. The writers suggest that the negative exponential curve be extended beyond the point $\tau_c = 20$ dynes/cm^2, so that the negative exponential relation between $\dot{R}$ and τ_c holds true for all values of $\tau_c > 6$ dynes/cm^2. This is justified because, as the value of τ_c increases, $\dot{R}$ has to decrease, and for very large values of τ_c, $\dot{R} \to 0$. Hence the rate of erosion, R, is given by

137

FIG. 3. (a) Variation of τ in Trapezoidal Cross Section; (b) Maximum Unit Tractive Forces versus b/d (after Simons and Sentürk 1976)

$$R = \tau_c \cdot \dot{R} \quad \dots\dots\dots\dots\dots\dots\dots\dots\dots\dots\dots\dots\dots\dots\dots\dots \quad (5a)$$

and $R = 223 * 10^{-4} \times \tau_c e^{-0.13\tau_c}$ (gm/cm^2 · min) $\dots\dots\dots\dots\dots\dots$ (5b)
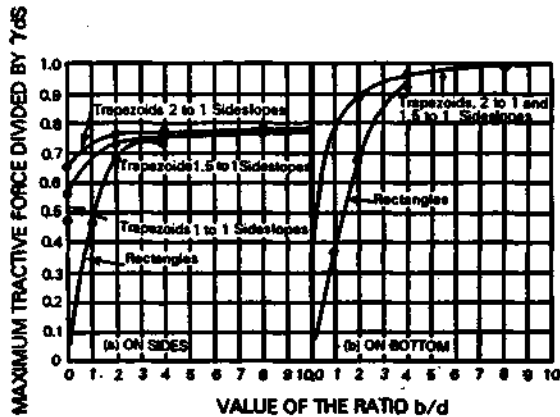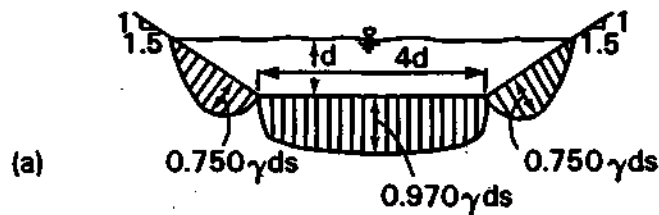
The method presented here is for cohesive banks. A lower bound for its application is $\tau_c = 6$ dynes/cm^2. Soils with lower critical shear stresses are only weakly cohesive and will generally behave as cohesionless materials.

The fluid shear stress, τ, on the channel boundaries is assumed to be constant so long as the hydraulic characteristics of the flow and the channel geometry remain constant. The cross-sectional distribution of boundary shear stress is usually assumed to be as shown in Figs. 3(a–b), but unfortunately, channel widening due to bank erosion and bed elevation changes, alters the geometry of the cross section. Therefore, the shear stress distribution of Figs. 3(a–b) can no longer be used for cross-sectional geometries like that shown later in Fig. 4(b). Unless a better estimate of bank shear stress is available, the average flow shear stress can be used, as in step 1.

The following example shows how to apply these steps to predict the soil critical shear stress, τ_c, the rate of erosion of the soil, R, and the lateral erosion distance, ΔW.

A soil sample taken from an erosive bank is found to have the following properties: SAR = 10; $\Delta\varepsilon = 20$; CONC = 0.250 N; and $\gamma = 17.28$ KN/m^3. Over the period considered, the average flow shear τ is found to be 9.8

138

N/m^2 or 98 dynes/cm^2. From Fig. 1 with SAR = 10, $\Delta\varepsilon = 20$, and CONC = 0.25 N, $\tau_c = 37$ dynes/cm^2. Since $\tau > \tau_c$, soil erosion will take place. From Eq. 1, it is seen that

$$R = 223 \times 10^{-4} \tau_c e^{-0.13\tau_c} = 6.7228 \times 10^{-3} \text{ (gm/cm}^2 \cdot \text{min)} \dots\dots\dots (6a)$$

and converting to SI units yields

$$R = 6.59278 \times 10^{-4} \text{ KN/m}^2 \cdot \text{min} \dots\dots\dots\dots\dots\dots\dots\dots\dots (6b)$$

The initial lateral erosion rate on each riverbank, dB, is

$$dB = \frac{R}{\gamma} = 3.81526 \times 10^{-5} \text{ m/min} \dots\dots\dots\dots\dots\dots\dots\dots\dots\dots (7)$$

Since the rate of erosion, R, is assumed to have an approximately linear increase with flow shear stress once the soil critical shear stress is surpassed, the actual erosion rate, dW, at one of the banks is

$$dW = dB \times \left(\frac{\tau - \tau_c}{\tau_c}\right) = 6.2900 \times 10^{-5} \text{ m/min} \dots\dots\dots\dots\dots\dots (8)$$

If the duration of the flow shear stress, $\Delta\tau$, is one day, then the lateral erosion distance, ΔW, during this period is

$$\Delta W = dW \times \Delta\tau = 0.091 \text{ m} \dots\dots\dots\dots\dots\dots\dots\dots\dots\dots\dots\dots (9)$$

RIVERBANK STABILITY RELATIONS

In studying the stability of the riverbanks, Ponce (1978) and Thorne et al. (1981) assumed that the bank geometry is as shown in Fig. 4(a). Stability relations developed in soil mechanics were then applied directly to the bank as represented by Fig. 4(a). This approach is not exact because in natural rivers, lateral erosion and bed degradation act to steepen the bank, characteristically forming an almost vertical cut, as shown in Fig. 4(b). In this paper, stability relations for this specific, characteristic bank geometry are developed. They can be used to predict the critical bank height H, the width of failure block BW, and volume of the failure mass, VB, per unit channel length.

Certain assumptions are essential to the analysis. These are:

1. The soil is cohesive and relatively homogeneous, so that average soil properties can be applied.

2. The failure surface passes through the toe of the bank. Other types of failure are not considered in the analysis since toe failures are most commonly observed.

3. Other factors, such as vegetation density and type, water table, surface runoff, and seepage need not be considered directly in the general analysis, although these factors may be important at particular locations and might be accounted for by modifying the analysis.

4. Depending on the bank slope angle i, riverbanks can be classified using the schemes of Taylor (1948) and Lohnes and Handy (1968) as: (1) Banks with steep slopes $i > 60°$; and (2) banks with gentle slopes $i \leq 60°$.
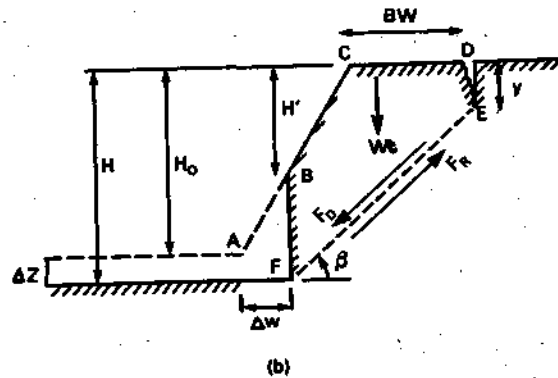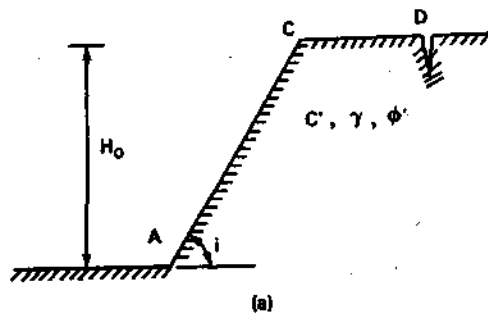
139

FIG. 4. (a) Right Riverbank before Erosion; (b) Right Riverbank after Erosion to Point of Failure

5. It is assumed that steep slopes fail along an almost planar failure surface, while a gentle slope exhibits a curved failure surface. Most eroding riverbanks are very steep. Often bank angles are close to 90°, especially at the outer bank in bends. Consequently, stability relations are developed herein only for steep banks. A similar treatment for gentle banks may be found in Osman (1985).

Initial Bank Failure

Fig. 4(a) shows the geometry of a steep riverbank (right bank) prior to lateral erosion and bed degradation. Fig. 4(b) shows the geometry after erosion. ΔW defines the change in the riverbed width due to lateral erosion at the right bank, and ΔZ is the degradation depth over the time period $\Delta\tau$. H_0 is the initial bank height above the bed, and H' is the bank height above point B in Fig. 4(b). The term i is the initial bank angle, β is the angle that the failure plane makes with the horizontal, y is the depth of tension cracking, and H is the bank height above the riverbed. The terms c', γ, and ϕ' are the effective cohesion, specific weight, and the effective angle of friction, respectively.

The factor of safety FS, is defined as

$$FS = \frac{\text{Resisting force}}{\text{Driving force}} = \frac{F_R}{F_D} \quad \dots\dots\dots\dots\dots\dots (10)$$

The resisting force, F_R, is proportional to the effective cohesion c' and angle of friction ϕ', and from Fig. 4(b) is defined as

$$F_R = c'FE + N \tan \phi' \quad \dots\dots\dots\dots\dots\dots\dots (11)$$

where N = component of the weight, Wt, normal to the failure surface = $Wt \cos \beta$; and FE = length of the failure surface = $(H - y)/\sin \beta$.

Hence $\quad F_R = \dfrac{(H - y)c'}{\sin \beta} + Wt \cos \beta \tan \phi' \quad \dots\dots\dots\dots (12)$

The driving force, F_D, is given by

$$F_D = Wt \sin \beta \quad \dots\dots\dots\dots\dots\dots\dots\dots (13)$$

where Wt = weight of the failure block, given by

$$Wt = \frac{\gamma}{2}\left(\frac{H^2 - y^2}{\tan \beta} - \frac{H'^2}{\tan i}\right) \quad \dots\dots\dots\dots (14)$$

Hence $\quad F_D = \dfrac{\gamma}{2}\left(\dfrac{H^2 - y^2}{\tan \beta} - \dfrac{H'^2}{\tan i}\right) \sin \beta \quad \dots\dots\dots (15)$

Substituting in Eq. 10 and rearranging the terms yields

$$(H^2 - y^2)(\sin \beta \cos \beta - \cos^2 \beta \tan \phi) - (H - y)\frac{2c}{\gamma}$$

$$+ (\sin \beta \cos \beta \tan \phi - \sin^2 \beta)\frac{H'^2}{\tan i} = 0 \quad \dots\dots\dots\dots (16)$$

where $\quad c = \dfrac{c'}{FS} \quad \dots\dots\dots\dots\dots\dots\dots\dots\dots\dots (17a)$

$$\tan \phi = \frac{\tan \phi'}{FS} \quad \dots\dots\dots\dots\dots\dots\dots\dots\dots (17b)$$

In deriving the stability relations, it is convenient to incorporate the factor of safety FS, into the cohesion and friction terms so that uncertainties in estimating these parameters can be accounted for by the selection of a factor of safety other than unity. Letting $y = K \cdot H$ ($0 \le K < 1$) and dividing Eq. 16 by H'^2 yields

$$\left(\frac{H}{H'}\right)^2 (1 - K^2)(\sin \beta \cos \beta - \cos^2 \beta \tan \phi) - \left(\frac{H}{H'}\right)(1 - k)\frac{2c}{\gamma H'}$$

$$+ (\sin \beta \cos \beta \tan \phi - \sin^2 \beta)\frac{1}{\tan i} = 0 \quad \dots\dots\dots\dots (18)$$

or
$$\lambda_1 \left(\frac{H}{H'}\right)^2 - \lambda_2 \left(\frac{H}{H'}\right) + \lambda_3 = 0 \quad \dots \dots \dots \dots \dots \dots (19)$$

which is a quadratic equation in (H/H'). The solution is given by

$$\frac{H}{H'} = \frac{\left[\frac{\lambda_2}{\lambda_1} \pm \sqrt{\left(\frac{\lambda_2}{\lambda_1}\right)^2 - 4\left(\frac{\lambda_3}{\lambda_1}\right)}\right]}{2} \quad \dots \dots \dots \dots (20a)$$

where $\lambda_1 = (1 - K^2)(\sin \beta \cos \beta - \cos^2 \beta \tan \phi) \quad \dots \dots \dots (20b)$

$$\lambda_2 = 2(1 - K) \frac{c}{\gamma H'} \quad \dots \dots \dots \dots \dots \dots \dots \dots \dots (20c)$$

$$\lambda_3 = \frac{(\sin \beta \cos \beta \tan \phi - \sin^2 \beta)}{\tan i} \quad \dots \dots \dots \dots (20d)$$

For a vertical bank

$$\beta \cong \frac{(90 + \phi)}{2} \quad \dots \dots \dots \dots \dots \dots \dots \dots \dots (20e)$$

The exact expression for β is derived later, and it can be shown that $\lambda_3 \leqq 0$. Since for most cohesive riverbanks the angle of friction is less than 40°, $\beta > \phi$ and hence

$$\lambda_1 = (1 - K^2) \cos^2 \beta (\tan \beta - \tan \phi) \geqq 0 \quad \dots \dots \dots (21)$$

Consequently, the expression within the square root of Eq. 20a must be positive and greater than λ_2/λ_1, i.e.

$$\sqrt{\left(\frac{\lambda_2}{\lambda_1}\right)^2 - 4\left(\frac{\lambda_3}{\lambda_1}\right)} \geqq \frac{\lambda_2}{\lambda_1} \quad \dots \dots \dots \dots \dots \dots (22)$$

Therefore

$$\frac{H}{H'} = \frac{\left[\frac{\lambda_2}{\lambda_1} + \sqrt{\left(\frac{\lambda_2}{\lambda_1}\right)^2 - 4\left(\frac{\lambda_3}{\lambda_1}\right)}\right]}{2} \quad \dots \dots \dots \dots (23)$$

In Eq. 23, $H/H' \geqq 1$ [Fig. 4(b)]. If $H/H' = 1$, this means that the initial slope geometry of Fig. 4(a) is unstable and the problem reduces to that considered by Taylor (1948) and Lohnes and Handy (1968).

From Fig. 4(b), the width of the failure block, at CD, is given by

$$BW = \left(\frac{H - y}{\tan \beta} - \frac{H'}{\tan i}\right) \quad \dots \dots \dots \dots \dots \dots (24)$$

and the volume of the failure block per unit length of channel is defined by

$$VB = \frac{1}{2}\left(\frac{H^2 - y^2}{\tan \beta} - \frac{H'^2}{\tan i}\right) \quad \dots \dots \dots \dots (25)$$

Failure Plane Angle

Taylor (1948) and Spangler and Handy (1973) indicated that the angle, β, between the failure plane and the horizontal corresponds to the plane of fully developed cohesion on which the stability number, $N_s = c/\gamma H'$, is a maximum. Hence, the angle β can be found by equating the first derivative of c, or $c/\gamma H'$, with respect to β in Eq. 11, to zero. Using this approach it can be shown that

$$\tan 2\beta = \frac{\left(\frac{H}{H'}\right)^2 (1 - K^2) \tan i + \tan \phi}{1 - \left(\frac{H}{H'}\right)^2 (1 - K^2) \tan i \tan \phi} \quad \dots \dots \dots (26a)$$

or $\tan 2\beta = \tan \left\{ \tan^{-1}\left[\left(\frac{H}{H'}\right)^2 (1 - K^2) \tan i\right] + \phi \right\} \quad \dots \dots (26b)$

Therefore

$$\beta = \frac{1}{2}\left\{ \tan^{-1}\left[\left(\frac{H}{H'}\right)^2 (1 - K^2) \tan i\right] + \phi \right\} \quad \dots \dots \dots (27)$$

For the special case where lateral erosion and bed degradation are negligible, $H = H'$, and where there is no tension crack $K = 0$, then Eq. 27 reduces to

$$\beta = \frac{1}{2}(i + \phi) \quad \dots \dots \dots \dots \dots \dots \dots \dots \dots \dots (28)$$

as given by Taylor (1948) and Spangler and Handy (1973).

Parallel Bank Retreat

Parallel bank retreat is often displayed by eroding banks in the field. After the initial bank failure [Fig. 4(b)], the new bank geometry is that shown in Fig. 5(a). Fig. 5(b) shows the geometry of the bank at the next failure with the variables as previously defined for Figs. 4(a–b). Note that the bank angle is now β and not i.

From Fig. 5(b), it is seen that

$$Wt = \frac{\gamma}{2}\left(\frac{H^2 - H'^2}{\tan \beta}\right) \quad \dots \dots \dots \dots \dots \dots \dots (29)$$

Therefore

$$F_D = \frac{\gamma}{2}\left(\frac{H^2 - H'^2}{\tan \beta}\right) \sin \beta \quad \dots \dots \dots \dots \dots \dots (30)$$

Substituting for F_R in Eqs. 30, 12, and 17a–b into Eq. 10 and letting $y = K \cdot H$, with $(0 \leq K < 1)$, yields

$$(H^2 - H'^2)(\cos \beta \sin \beta - \cos^2 \beta \tan \phi) - H(1 - K)2\frac{c}{\gamma} = 0 \quad \dots \dots (31)$$
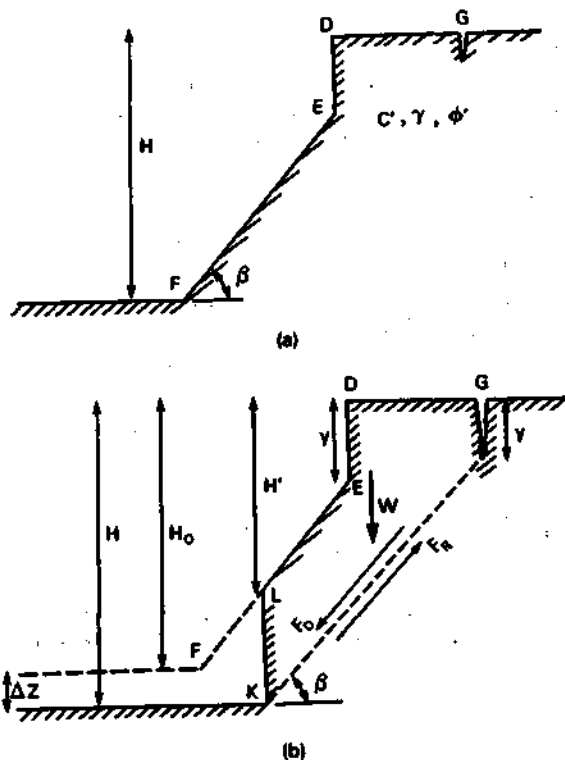
FIG. 5. Parallel Bank Retreat: (a) Right Riverbank after Initial Failure [Fig. 4(b)]. (b) Right Riverbank after Erosion to Point of Failure

dividing by H'^2 and rearranging produces

$$\omega_1\left(\frac{H}{H'}\right)^2 - \omega_2\left(\frac{H}{H'}\right) - \omega_1 = 0 \quad \dots \dots \dots \dots \dots \dots \dots \dots \quad (32)$$

which is a quadratic equation in (H/H'). The solution is given by

$$\frac{H}{H'} = \frac{\left[\dfrac{\omega_2}{\omega_1} \pm \sqrt{\left(\dfrac{\omega_2}{\omega_1}\right)^2 + 4}\right]}{2} \quad \dots \dots \dots \dots \dots \dots \dots \quad (33)$$

Since $H/H' \geqq 1$

$$\frac{H}{H'} = \frac{\left[\dfrac{\omega_2}{\omega_1} + \sqrt{\left(\dfrac{\omega_2}{\omega_1}\right)^2 + 4}\right]}{2} \quad \dots \dots \dots \dots \dots \dots \quad (34a)$$

where $\quad \omega_1 = \cos\beta \sin\beta - \cos^2\beta \tan\phi \quad \dots \dots \dots \dots \quad (34b)$

and $\quad \omega_2 = 2(1 - K)\dfrac{c}{\gamma H'} \quad \dots \dots \dots \dots \dots \dots \dots \dots \quad (34c)$

From Fig. 5(b), the failure block width is given by

$$BW = \frac{(H - H')}{\tan\beta} \quad \dots \dots \dots \dots \dots \dots \dots \dots \dots \dots \dots \dots \quad (35)$$

and the volume of the failure block per unit channel length is

$$VB = \frac{(H^2 - H'^2)}{2\tan\beta} \quad \dots \dots \dots \dots \dots \dots \dots \dots \dots \dots \quad (36)$$

In Eqs. 23 and 34a, the terms λ_1, λ_3, and ω_1 reflect the effects of the bank geometry and tension cracks on the critical bank height, while the terms λ_2 and ω_2 show how much the stability number, $c/\gamma H'$, is reduced by the presence of tension cracks.

The critical bank height has been derived as an explicit function of the bank soil properties and bank geometry. In fact, the critical bank height is also a time-dependent variable because lateral erosion and bed degradation act through time to alter bank geometry.

From Figs. 4(b) and 5(b), the critical height H is geometrically defined by

$$H = H' + \Delta W \tan i + \Delta Z \quad \dots \dots \dots \dots \dots \dots \dots \dots \dots \quad (37)$$

where ΔW and ΔZ = the change in bed width and bed degradation distances necessary to bring the bank to failure, respectively. Clearly, the erosion responsible for ΔW and ΔZ does not occur instantaneously, but is a function of time, where

$$\Delta W = \Delta W(\tau_f, \tau_c) \quad \dots \dots \dots \dots \dots \dots \dots \dots \dots \dots \dots \dots \quad (38)$$

$$\tau_c = \tau_c(SAR, CONC, \Delta\varepsilon) \quad \dots \dots \dots \dots \dots \dots \dots \dots \dots \quad (39)$$

$$\tau = \tau(Q, R_h, S, \rho_w, g) \quad \dots \dots \dots \dots \dots \dots \dots \dots \dots \dots \dots \quad (40)$$

Therefore

$$\Delta W = \Delta W(Q, R_h, S, \rho_w, SAR, CONC, \Delta\varepsilon, g) \quad \dots \dots \dots \dots \quad (41)$$

and $\quad \Delta Z = \Delta Z(Q, R_h, S, \rho_w, \rho_s, D_s, g) \quad \dots \dots \dots \dots \dots \dots \quad (42)$

Hence $\quad H = H(Q, R_h, S, \rho_w, SAR, CONC,$

$$\Delta\varepsilon, \rho_s, D_s, c', \gamma, \phi', H_0, y, g) \quad \dots \dots \dots \dots \dots \dots \dots \dots \quad (43)$$

where Q = flow discharge; R_h = hydraulic radius; S = energy slope; ρ_w = water density; and D_s = bed material size.

Time is accounted for using an aggradation/degradation model based on solving the sediment continuity equation, sediment transport equation, and the rate of lateral erosion. This approach is presented in the companion paper to this one.

The solution of Eqs. 23 and 34a for the ratio H/H' at any time requires the angle β to be known. Eq. 27 is the relation that determines angle β in terms of the slope angle i and the ratio H/H' computed from the values of H and H'. This is demonstrated later. In general, both bank heights H above the riverbed and H' above point B [Fig. 4(b)] vary with time. H

varies in proportion to the rate at which the channel bed is lowered, while H' varies in proportion to the rate of lateral erosion. In other words, the H/H' changes according to the flow and bed material characteristics and the stiffness of the bank soil. The solution of Eqs. 23 and 34a is shown later. The approach is to compare the ratio $(H/H')_m$ obtained from measured values of H and H', to the analytical ratio $(H/H')_c$ obtained from Eq. 23 or 30.

COMPUTATIONAL SEQUENCE

1. After any time, use the known degradation depth, ΔZ, and lateral erosion distance, ΔW, to determine the bank heights H above the riverbed and H' above point B [Fig. 4(b)] as

$$H = H_0 + \Delta Z \dots \dots \dots \dots \dots \dots \dots \dots (44)$$

$$H' = H_0 - \Delta W \tan i \dots \dots \dots \dots \dots \dots (45)$$

where H_0 = the initial bank height [Fig. 4(a)]; and $H' = H_0$ initially.

2. Next, find the measured bank height ratio $(H/H')_m$ using these values.

3. Use this measured ratio of $(H/H')_m$ to find angle β from Eq. 27, as follows:

$$\beta = \frac{1}{2}\left\{ \tan^{-1}\left[\left(\frac{H}{H'}\right)_m^2 (1 - K^2) \tan i \right] + \phi \right\} \dots \dots \dots (46)$$

4. Compute the values of λ_1, λ_2, and λ_3, which appear in Eq. 23, using Eqs. 13b–d, respectively.

5. Substitute the values of λ_1, λ_2, and λ_3 in Eq. 23 to find the analytical bank height rate $(H/H')_c$:

$$\left(\frac{H}{H'}\right)_c = \frac{\left[\frac{\lambda_2}{\lambda_1} + \sqrt{\left(\frac{\lambda_2}{\lambda_1}\right)^2 - 4\left(\frac{\lambda_3}{\lambda_1}\right)}\right]}{2} \dots \dots \dots \dots (47)$$

6. If $(H/H')_m$ computed in step 2 is less than $(H/H')_c$ computed from Eq. 23, then the slope is stable and H is not the critical height.

7. As there is no failure, degradation continues during the next time step. Therefore, increase the time, compute the new ΔZ and ΔW, and return to step 2, with $H = H + \Delta Z$ and $H' = H' - \Delta W \tan i$.

8. If $(H/H')_m \approx (H/H')_c$, then $(H/H')_c$ is the solution of Eq. 23 and H is the critical bank height.

9. Use Eqs. 24 and 25 to compute the failure block width (BW) and volume (VB) per unit length of channel.

10. If $(H/H')_m > (H/H')_c$, then the bank is unstable and bank failure must already have taken place. In this case, ΔZ and ΔW are unrealistically large and must be reduced.

After the bank has failed, the new slope angle $= \beta$ (parallel bank retreat). For subsequent failures, use steps 1 and 2 to compute $(H/H')_m$. Step 3 is redundant, because angle β is known at any time (parallel bank retreat). In step 4, use Eqs. 34b and 34c to compute ω_1 and ω_2. The term ω_1 is a constant because it is only a function of β and ϕ. Use Eq. 34a in step 5 to calculate $(H/H')_c$ as follows:

$$\left(\frac{H}{H'}\right)_c = \frac{\left[\frac{\omega_2}{\omega_1} + \sqrt{\left(\frac{\omega_2}{\omega_1}\right)^2 + 4}\right]}{2} \dots \dots \dots \dots (48)$$

Use steps 6–8 to find the critical bank height. In step 9, use Eqs. 35 and 36 to find the block width and the failure block volume.

To demonstrate this procedure, hypothetical data may be used in a numerical example, as follows. The initial riverbank height, $H_0 = 1.5$ m, $i = 80°$, $\gamma = 15.1$ KN/m³, $\phi' = 7.0°$, and $c' = 13.0$ KN/m². Bed degradation occurs with no lateral erosion.

The factor of safety FS = 1.0, and at failure $K = y/H_c = 0.50$, where y = the depth of tension cracking.

From Eqs. 17a–b, $c = c'/FS = 13.0$ KN/m² and $\tan \phi = \tan \phi'/FS$ so that $\phi = 7.0°$. The computations are shown in Table 1. For this bank, 1.3 m of degradation was necessary to trigger failure. From Eq. 24, the block width was 1.06 m, and from Eq. 25 the volume of failed bank material was 2.59 m³ per meter of channel length. Note that in Table 1 the size of the degradation increment is reduced as failure is approached to better define the critical height.

Subsequent failures occur due to lateral erosion. Further degradation is unlikely once the banks reach critical height. The critical lateral erosion distance is 1.19 m, generating a failure block width of 1.19 m and a failure volume of 2.58 m³/m. The bank will then recede by parallel retreat with a height of 2.80 m, with failure occurring when basal clean out of slump debris brings the bank back to the critical condition. The case of both bed degradation and lateral erosion is more complex and is best handled using a computer program, which is described in the companion paper to this one.

TABLE 1. Bank Stability Calculations

ΔZ (m) (1)	H (m) (2)	H' (m) (3)	(H/H') (m) (4)	β (°) (5)	γ_1 (6)	γ_2 (7)	γ_3 (8)	$(H/H')_c$ (9)
0.000	1.500	1.50	1.000	41.88	0.3217	0.5740	-0.0678	1.895
0.172	1.672	1.50	1.115	43.14	0.3252	0.5740	-0.0716	1.882
0.160	1.832	1.50	1.221	44.02	0.3272	0.5740	-0.0743	1.875
0.147	1.979	1.50	1.319	44.65	0.3284	0.5740	-0.0763	1.872
0.136	2.115	1.50	1.410	45.13	0.3292	0.5740	-0.0777	1.870
0.129	2.244	1.50	1.496	45.50	0.3297	0.5740	-0.0789	1.870
0.120	2.364	1.50	1.576	45.80	0.3301	0.5740	-0.0798	1.869
0.109	2.473	1.50	1.649	46.03	0.3304	0.5740	-0.0805	1.868
0.101	2.574	1.50	1.716	46.22	0.3306	0.5740	-0.0811	1.868
0.090	2.664	1.50	1.776	46.37	0.3307	0.5740	-0.0816	1.867
0.090	2.754	1.50	1.836	46.51	0.3309	0.5740	-0.0820	1.867
0.047	2.801	1.50	1.867	46.57	0.3309	0.5740	-0.0822	1.867

146

147

SUMMARY AND CONCLUSIONS

Riverbank retreat is the product of fluvial erosion and mass instability. A process-based explanation of bank retreat and width response to changes in flow hydraulics or sediment transport must account for the contribution of both factors.

In this paper, the analysis of cohesive soil erosion by flowing water developed at the Waterways Experiment Station in cooperation with the University of California at Davis (Arulanandan et al. 1980) is applied to calculate the lateral bank erosion due to fluvial entrainment of bank material. While this approach is by no means the last word on the difficult topic of the erosion of cohesive soils, it does perhaps represent one of the most promising of the currently available methods of analysis, because calculation of the critical shear stress for erosion is based on the electro-chemical properties of the soil, pore water, and eroding fluid. The erosion rate is computed from the excess shear stress over the critical value, as it is in most other methods. The mass stability of the bank is calculated using a static equilibrium analysis of slab-type failure, which is the most common failure mechanism for steep, cohesive riverbanks. Unlike previous analyses, the method used here incorporates changes of bank geometry due to lateral erosion and/or basal lowering through bed degradation. Stability is computed based on the bank geometry (slope, height, and cut bank height) and the soil parameters of effective cohesion, effective friction angle, and bulk unit weight.

The controls of the two causes of retreat are seen to be very different. Lateral erosion depends on the microscale electrochemical properties of the soil, which determine the critical shear stress for entrainment, and on the excess boundary shear stress above this critical value. Conversely, mass stability depends on the macroscale properties of the bank, and the fluid shear stress is not a factor. However, continued retreat through mass failure requires basal cleanout of slumped debris. As this depends entirely on fluvial entrainment, rates of retreat by mass failure are fluvially controlled, even though the mass stability of the bank is not directly related to flow forces (Thorne 1982).

Inevitably, the processes and mechanisms of bank erosion and retreat have been greatly simplified in order to make them amenable to analysis. For example, soil properties are assumed to be homogeneous, failure is taken to be catastrophic rather than progressive, and fluvial erosion is treated separately in time to mass failure. Perhaps the most serious shortcoming is that vegetation effects are not accounted for explicitly. It is evident from theoretical and experimental evidence that vegetation does have a significant impact on bank stability and channel width, both through its effects on near-bank flow hydraulics and on bank material properties (Hey and Thorne 1986). While it is proposed to develop the analysis to incorporate vegetation in a subsequent version, it is the writers' contention that the approach presented here represents a useful tool in the analysis of bank instability due to lateral erosion or bed degradation.

APPENDIX I. REFERENCES

Arulanandan, K., Gillogley, E., and Tully, R. (1980). "Development of a quantitative method to predict critical shear stress and rate of erosion of natural undisturbed cohesive soils." *Report GL-80-5*, U.S. Army Engineers, Waterways Experiment Station, Vicksburg, Miss.

Hey, R. D., and Thorne, C. R. (1986). "Stable channels with mobile gravel beds." *J. Hydr. Engrg.*, ASCE, 112(8), 671–689.

Hooke, J. M. (1979). "An analysis of the processes of river bank erosion." *J. Hydrol.*, 42, 39–62.

Lamb, T. W., and Whittman, R. V. (1969). *Soil mechanics*. John Wiley and Sons, Inc., New York, N.Y.

Lohnes, R., and Handy, R. L. (1968). "Slope angles in friable loess." *J. Geol.*, 76, 247–258.

Osman, A. M. (1985). "Channel width response to changes in flow hydraulics and sediment load." thesis presented to Colorado State University, at Fort Collins, Colo., in partial fulfillment of the requirements of the degree of Doctor of Philosophy.

Ponce, V. M. (1978). "Generalized stability analysis of channel banks." *J. Irrig. Drainage Div.*, ASCE, 104(4), 343–350.

Simons, D. B., and Sentürk, F. (1976). *Sediment transport technology*. Water Resources Publications, Fort Collins, Colo.

Spangler, M. G., and Handy, R. L. (1973). *Soil engineering*. 3rd Ed., Intext Educational, New York, N.Y.

Taylor, D. W. (1948). *Fundamentals of soil mechanics*. John Wiley and Sons, New York, N.Y.

Thorne, C. R. (1981). "Field measurements of rate of bank erosion and bank material strength." *Erosion and sediment transport measurement. Proc., Florence Symp.*, International Association for Hydraulic Science Publ. No. 133, Florence, Italy.

Thorne, C. R. (1982). "Process and mechanisms of river bank erosion." *Gravel-bed rivers*, R. D. Hey, J. C. Bathurst, and C. R. Thorne, eds., John Wiley and Sons, Ltd., Chichester, U.K., 227–271.

Thorne, C. R., Murphey, J. B., and Little, W. C. (1981). "Bank stability and bank material properties in the bluffline streams of northwest Mississippi." *Stream channel stability*, Appendix D, Section 32 Program, Work Unit 7, U.S. Army Corps of Engineers, Vicksburg District, Vicksburg, Miss.

Wolman, M. G. (1959). "Factors influencing the erosion of cohesive river banks." *Amer. J. Sci.*, 257, 204–216.

APPENDIX II. NOTATION

The following symbols are used in this paper:

BW	=	block width;
$CONC$	=	pore fluid salt concentration in bank material;
c'	=	effective cohesion;
D_s	=	bed material size;
dB	=	initial lateral erosion rate;
dW	=	lateral erosion rate;

F_D	=	driving force;
F_R	=	resisting force;
FS	=	factor of safety;
g	=	gravitational acceleration;
H	=	bank height;
H'	=	bank height above zone of lateral erosion;
H_0	=	initial bank height;
$(H/H')_c$	=	calculated (critical) bank-height ratio;
$(H/H')_m$	=	measured (observed) bank-height ratio;
i	=	bank angle;
K	=	ratio of crack depth to bank height;
N	=	weight component normal to failure surface;
N_s	=	stability number;
Q	=	discharge;
R	=	rate of soil erosion;
$\dot{R}$	=	rate of change of erosion with shear stress;
R_h	=	hydraulic radius;
S	=	energy slope;
SAR	=	sodium adsorption ratio of bank material;
VB	=	volume of failure block per unit channel length;
Wt	=	weight of failure block;
y	=	depth of tension cracking;
γ	=	specific weight of bank material;
γ_w	=	specific weight of water;
ϕ'	=	effective angle of internal friction;
τ	=	fluid shear stress;
τ_c	=	critical fluid shear stress;
$\Delta\epsilon$	=	dielectric dispersion of bank material;
$\Delta\tau$	=	duration of flow shear on bank;
ΔW	=	actual lateral erosion distance;
ΔZ	=	degradation distance;
β	=	failure plane angle and bank angle during parallel retreat;
$\lambda_1,\lambda_2,\lambda_3$	=	factors in slope stability equations;
ω_1,ω_2	=	factors in slope stability equations for parallel retreat; and
ρ_w	=	density of water.

RIVERBANK STABILITY ANALYSIS. II: APPLICATIONS

By Colin R. Thorne,[1] Affiliate Member, ASCE, and Akode M. Osman[2]

Abstract: Bank retreat occurs by a combination of lateral erosion by the flow and mass failure under gravity. A new analysis of bank erosion and failure is developed, using a critical shear-stress concept to account for lateral erosion and a slope stability criterion for mass failure. In this paper, we apply the analysis to two problems of bank retreat often encountered by practicing engineers dealing with alluvial channels. The first application is to the prediction of degradation downstream of a dam, for the case in which bed lowering causes bank instability. We show that rapid bank retreat can occur once the threshold height for mass failure of the banks is reached. This supplies sediment to the flow, tends to limit the depth of degradation, and drives complex response downstream. The second application is to the modeling of flow in channel bends and the prediction of the equilibrium cross section. We show that scour depth at the outer bank may be limited by the critical bank height. If scouring causes the outer bank to fail, then the channel will migrate laterally rather than scour down vertically. The analysis presented here can be used to predict the equilibrium cross section and migration rate incorporating bank stability considerations. It could also be used to predict the likely increase in scour depth resulting from outer bank stabilization in a bendway.

INTRODUCTION

The theories developed in a companion paper to study the stability of riverbanks are applied herein. As discussed in the first paper, most eroding cohesive riverbanks have steep slopes, and so the applications are limited to steep riverbanks ($i > 60°$). Procedures to incorporate the riverbank stability relations into engineering analyses are demonstrated using two particular cases: (1) Channel degradation downstream of a hydraulic structure; and (2) erosion of the outer bank in a channel bendway. These two cases represent the two most commonly occurring situations for severe bank erosion and instability encountered by practicing engineers.

RIVERBANK EROSION DUE TO BED DEGRADATION

In this section, the effect of degradation in producing channel widening due to bank erosion and instability is considered. This is achieved by incorporating the stability analysis outlined in the first paper into a model to estimate degradation depth downstream of a dam. The lateral erosion rate, R, is estimated using equation (1) from the first paper, and the solution of Eq. 23 or 34a from the companion paper determines the critical

ratio of (H/H'), where H = the total bank height and H' = the height above the zone of lateral erosion [see Fig. 4(b) in the first paper]. The impacts of widening on the flow hydraulics, sediment transport, sediment sources, and channel evolution are examined.

Degradation Model

Most existing degradation models assume that the riverbanks are stable and nonerodible, and hence that the channel width remains constant. This assumption is not always true because even if the banks are nonerodible, bed lowering results in decreasing stability of the bank with respect to mass failure. One of the few models that does take into account width adjustment is that of Chang (1982). His model incorporates bank stability and width changes by maintaining the bank angle at the angle of friction. This is appropriate for rivers with noncohesive banks, but in degrading channels with cohesive banks, most angles are much steeper than this.

A degradation model based on small time steps is essential when considering a channel with erodible banks. This is because the ratio (H/H') increases very rapidly as the channel erodes laterally (H' decreases) and the bed degrades (H increases), so that large time steps may give such large increases in the ratio of (H/H') that the value at which the riverbanks reach the critical state may be missed.

The approach described by Gessler (1971) for solving an uncoupled degradation model for nonerodible stable riverbanks is modified in this study to incorporate lateral channel bank erosion and the bank material contribution to the sediment load. The model uses a backwater analysis to obtain the water-surface profile, together with the solution of the sediment continuity equation and a relevant sediment transport equation to predict the degradation depth and the corresponding bed elevation.

The sediment continuity equation

$$\frac{\partial Z}{\partial t} + \frac{1}{1 - \lambda} \frac{\partial q_s}{\partial x} = 0 \quad \cdots \cdots \cdots \cdots \cdots \cdots \cdots \quad (1)$$

can be written in finite difference form as follows:

$$\Delta Z = \frac{-1}{1 - \lambda} \Delta t \frac{\Delta q_s}{\Delta x} \quad \cdots \cdots \cdots \cdots \cdots \cdots \cdots \quad (2)$$

where $\quad \dfrac{\Delta q_s}{\Delta x} = \dfrac{1}{2} \left(\dfrac{q_{s_{j-1}}^t - q_{s_j}^t}{\Delta x_j} + \dfrac{q_{s_j}^t - q_{s_{j+1}}^t}{\Delta x_{j+1}} \right) \quad \cdots \cdots \cdots \cdots \quad (3a)$

$$\Delta x_j = X_{j-1} - X_j \quad \cdots \cdots \cdots \cdots \cdots \cdots \cdots \quad (3b)$$

$$\Delta x_{j+1} = X_{j+1} - X_j \quad \cdots \cdots \cdots \cdots \cdots \cdots \quad (3c)$$

If $\Delta x = \Delta x_1 = \Delta x_2 = \ldots = \Delta x_j = \ldots = \Delta x_n$, then

$$\frac{\Delta q_s}{\Delta x} = \frac{q_{s_{j-1}}^t - q_{s_{j+1}}^t}{2\Delta x} \quad \text{(Central difference)} \quad \cdots \cdots \cdots \cdots \quad (3d)$$

152

where q_s = unit sediment load; X = distance from known position; Z = bed elevation; λ = bed material porosity; t = time; and j = cross section number.

The term ΔZ can be expressed as

$$\Delta Z = Z_j^t - Z_j^{t + \Delta t} + \frac{1}{2} [(Z_{j-1}^t + Z_{j+1}^t) - 2Z_j^t] \quad \cdots \cdots \cdots \cdots \quad (4)$$

Substituting for ΔZ and Δq_s in the sediment continuity equation produces

$$Z_j^{t + \Delta t} = Z_j^t + \frac{1}{2} (Z_{j-1}^t - 2Z_j^t + Z_{j+1}^t) + \frac{1}{1 - \lambda} \cdot \Delta t$$

$$\cdot \frac{1}{2} \left(\frac{q_{s_{j-1}}^t - q_{s_j}^t}{\Delta x_j} + \frac{q_{s_j}^t - q_{s_{j+1}}^t}{\Delta x_{j+1}} \right) \quad \cdots \cdots \cdots \cdots \quad (5)$$

The bed material porosity, λ, is determined from

$$\lambda = 0.245 + \frac{0.0864}{D_s^{0.21}} \quad \cdots \cdots \cdots \cdots \cdots \cdots \cdots \quad (6)$$

where D_s = median fall diameter in centimeters (Komura and Simons 1967).

In the present study, the Engelund-Hansen (1967) sediment transport equation, which is based on Bagnold's (1966) energy approach and similarity principles, is used as follows:

$$\frac{q_s}{\sqrt{(SG - 1) g D_{50}^3}} = 0.1 \left(\frac{U^2}{2gdS} \right) \cdot \left[\frac{\tau_0}{(\gamma_s - \gamma_w) D_{50}} \right]^{5/2} \quad \cdots \cdots \cdots \quad (7)$$

which can be simplified to the form

$$q_s = \frac{q^2 S^{1.5}}{20\sqrt{g} \sqrt{d} (SG - 1)^2 D_{50}} \quad \cdots \cdots \cdots \cdots \cdots \quad (8)$$

The variables are: d = average flow depth; D_{50} = median diameter of bed sediment; g = gravitational acceleration; q = discharge per unit width; q_s = sediment discharge per unit width; S = energy slope; and SG = specific gravity of bed material.

The following steps present a model of degradation downstream of a dam, with the channel width varying with time as a result of lateral erosion and mass failure of the riverbanks. The computational flow chart is shown in Fig. 1.

1. Assemble the data:
a. Bank soil properties and geometry: Unit weight, γ; effective cohesion, c'; effective angle of friction, ϕ'; sodium adsorption ratio, SAR; dielectric dispersion, $\Delta \varepsilon$; pore fluid concentration, CONC; initial bank height, H_0; and initial bank slope, i_0.
b. Flow and bed material characteristics: Discharge, Q; channel bed width, W; bed slope, S_0; bed profile, $Z_1 \ldots Z_N$; bed material
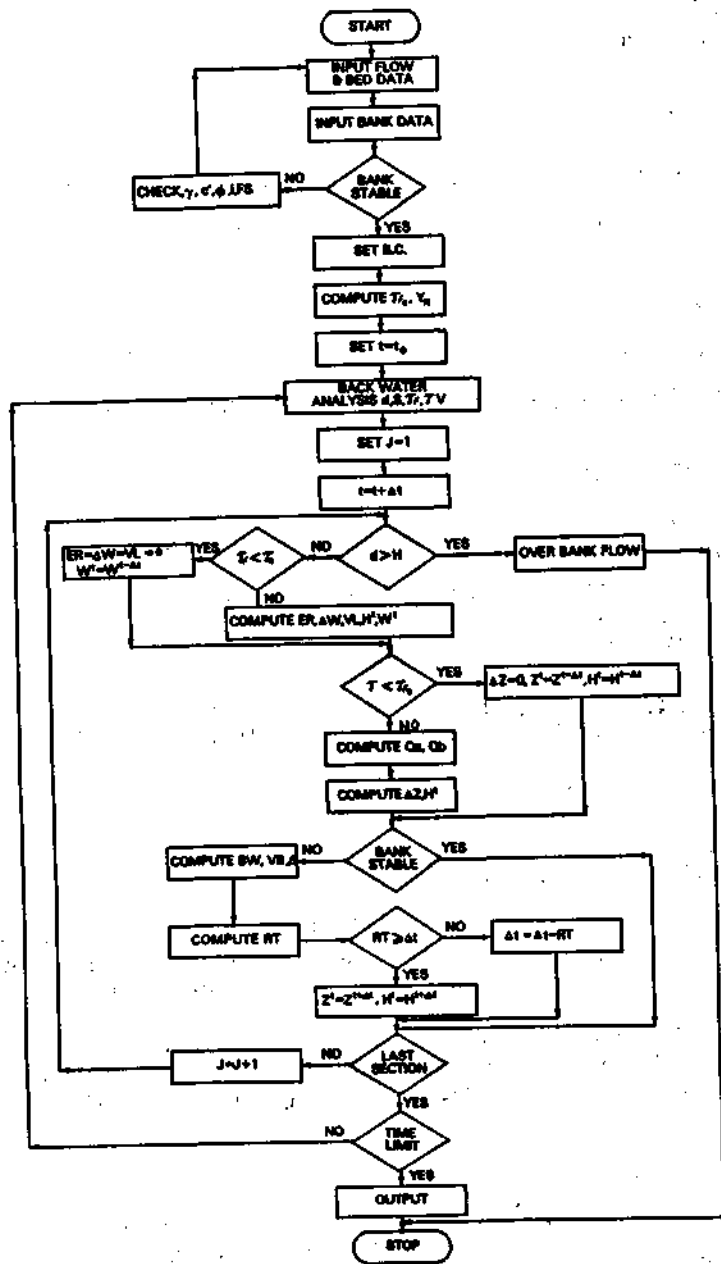
153

FIG. 1. Flow Chart of Computations

median fall diameter, D_s; largest bed material particle diameter, D_L; and Manning's coefficient, n.

2. Select a suitable value for the factor of safety, FS, and use Eqs. 17a–b in the first paper to find the new cohesion, c, and friction angle, ϕ.

3. Check whether the riverbanks are stable initially using steps 4–6 in the computation sequence in the first paper. If not, check the realism of the soil properties or the value of FS. If these are definitely correct, proceed.

4. Use Figs. 1 and 2 in the first paper to determine the critical shear stress for of the banks, τ_c.

5. Select a point downstream of the dam where degradation is insignificant, say a geological control, then divide the channel downstream of the dam into finite reaches up to this selected point. Decide on a suitable time step to be used in the computation.

6. Compute flow depth, d, energy slope, S, and boundary stress, τ, at each cross section starting the computation from the selected point with the water-surface profile determined by the standard step method.

7. Compute the lateral erosion rate, R, using Eq. 1 in the first paper.

8. Find the lateral erosion distance, ΔW, using Eq. 4 in the first paper. Then determine the volume of bank material eroded per unit channel length, VL, and the height H' from

$$VL = \Delta W \times d \qquad (9)$$

$$H'^{t + \Delta t} = H'^t - \Delta W \tan i \qquad (10)$$

where H' = bank height above zone of lateral erosion.

9. Compute new width $W^{t+\Delta t} = W^t + \Delta W$.

10. Compute sediment discharge, Q_s, at each cross section, using the Engelund-Hansen sediment transport equation.

11. Find the volume of bed material, Q_b, scoured from the riverbed from

$$Q_b = Q_s - VL \qquad (11)$$

12. Use Eq. 5 from this paper to compute the bed profile, and find the degradation depth, ΔZ, and bank height, H, from

$$\Delta Z = Z^t - Z^{t + \Delta t} \qquad (12)$$

$$H^{t + \Delta t} = H^t + \Delta Z \qquad (13)$$

13. Check the stability of the bank using Eq. 23 or 34a from the companion paper as appropriate. If it is stable, go to step 18.

14. If it is not stable, compute the failure block width, BW, the failure mass volume, VB, and the new bank slope, $i = \beta$, using Eqs. 24, 25, and 27.

15. Check the length of time needed by the flow to remove the failed bank material, assuming that the block was disturbed and loosened in the failure, from

$$RT = \frac{VB}{Q_s} \qquad (14)$$

where RT = removal time.

16. If RT is greater than Δt, then for the next computation step, assume no bed degradation, with the flow transport capacity being satisfied from the failed bank material. This is the basal clean-out phase characteristic of banks that fail due to bed degradation or undercutting (Thorne 1982).

17. If RT is less than Δt, then in the next computation step, bed degradation takes place only during the period $= \Delta t - RT$, i.e., after basal clean-out is completed.

18. Increase the time by Δt and repeat the procedure from step 6.

Numerical Example

This procedure is applied to study the effects of degradation downstream of a proposed dam on the stability of the riverbanks and the effect of bank-sediment yield and channel widening on the degradation rate, channel response downstream, flow energy, and the stream power of the flow. Realistic hypothetical data are used in the computations because real data of sufficient detail are unavailable.

1. Channel data are: $Q = 15.575$ m³/s; $S_0 = 0.0015$; $W = 12$ m; $D_{50} = 0.65$ mm; $D_L = 1.5$ mm; $n = 0.020$; and SG $= 2.65$.

2. Bank data are: $\gamma = 18.85$ KN/m³; $c' = 17.25$ KN/m²; $\phi' = 14.0°$; $i = 78°$; $H_0 = 2.4$ m; SAR $= 3.5$; $\Delta\varepsilon = 60$; and CONC $= 0.05$ N.

The dam is to be constructed 5.4 km upstream from a rocky site that acts as a geologic control. The distance downstream between the dam and the control is divided into nine reaches ($\Delta X = 600$ m) producing 10 cross sections. The flow is uniform prior to the construction of the dam.

At failure the factor of safety FS $= 1.0$, and so the values of cohesion and friction angle in Eqs. 17a–b are unchanged. Using Fig. 1 in the first paper (with SAR $= 3.5$, $\Delta\varepsilon = 60$, and CONC $= 0.050$ N), the critical shear stress $\tau_c = 40$ dyne/cm² $= 4.0$ N/m².

The computations are carried out for two cases: (1) the channel width is constant, i.e., assuming nonerodible stable banks; and (2) the channel width varies due to bank erosion and failure. The river sections close to the control at section 10 are excluded from the discussion because they are affected by the geologically constrained width.

Results from Example

Fig. 2 is a plan view of the river reach showing the variation of the channel width downstream of the dam 60, 120, and 180 days after closure. Fig. 3 shows cross section number 1 after these periods. As Figs. 2 and 3 indicate, lateral erosion was very active initially and decreased with time. This is because the erosion rate depends on the flow shear stress. As the cross-sectional area increased due to degradation and channel widening, the boundary shear stress decreased and the lateral erosion rate was reduced.

The effect of channel widening on bed degradation is clearly shown in Fig. 3. The shape of cross section number 1 for the case when the banks are erodible is compared to that when the channel is assumed to have a constant width. After 180 days, the bed degraded 4.13 m when the channel width was constant, compared to only 3.16 m when the channel had erodible banks. That is a difference of nearly one meter, or 24%, over 6 months, illustrating the importance of taking into consideration the erod-
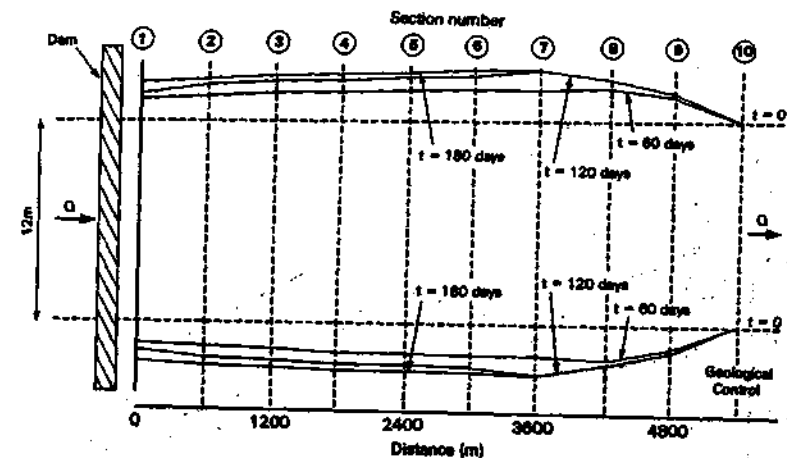

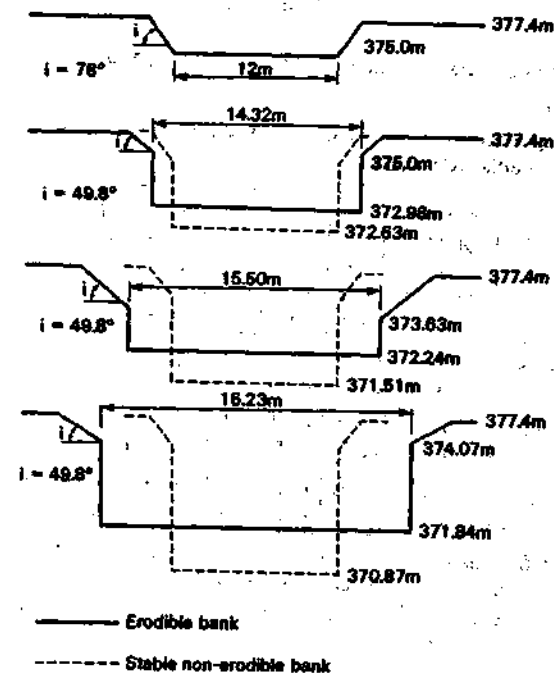FIG. 2. Channel Width Variation over 180 Days after Dam Closure

FIG. 3. Degradation at Section Number 1; from Top to Bottom: after 0, 60, 120, and 180 Days

ibility of the riverbanks when predicting the rate and amount of bed degradation.

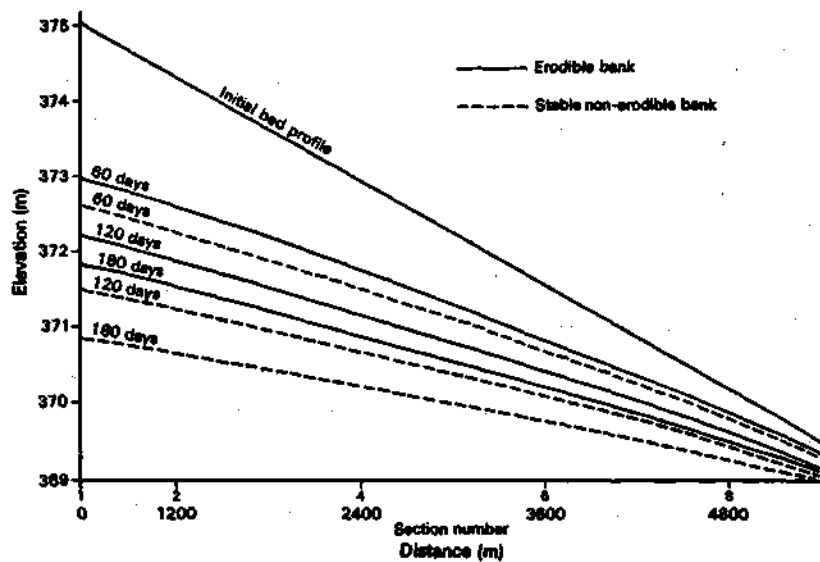In addition to Fig. 3, consideration of Fig. 4 and Table 1 supports this

156

157

FIG. 4. Channel Bed Profile Initially and after 60, 120, and 180 Days

FIG. 5. Energy Line and Bed Profile Initially and after 180 Days

TABLE 1. Comparison between Output of Degradation Model with Erodible Banks and with Stable Nonerodible Banks

Type of riverbank (1)	Number of days since dam closure (2)	ΔZ (m) (3)	W (m) (4)	V_{bed} (m³/m) (5)	V_{bank} (m³/m) (6)	V_{TOT} (m³/m) (7)	V_{bank}/V_{bed} (%) (8)	V_{bank}/V_{TOT} (%) (9)
Stable nonerodible	60	2.37	12.00	28.44	0	28.44	0	0
erodible	60	2.02	14.32	24.24	12	36.24	20.2	33
Stable nonerodible	120	3.49	12.00	41.88	0	41.88	0	0
erodible	120	2.76	15.50	33.12	29.19	62.31	88	46.9
Stable nonerodible	180	4.13	12.00	49.56	0	49.56	0	0
erodible	180	3.16	16.23	37.92	33.39	71.31	88	47.3

Note: V_{bed} = Bed material volume eroded. V_{bank} = Bank material volume eroded. V_{TOT} = Total material volume eroded from bed and banks.

conclusion. In detail, the reduction in the rate at which the bed is lowered due to the increased channel width is explained by two major factors. First, as the channel's cross-sectional area increases due to widening, boundary shear stress on the bed decreases to a low level. The decreasing shear stress is only capable of very slow rates of erosion and more rapidly approaches the critical value for bed material entrainment than in the fixed width case. Second, sediment contributed by the bank partially satisfies the flow's transport capacity, thereby reducing the amount of sediment
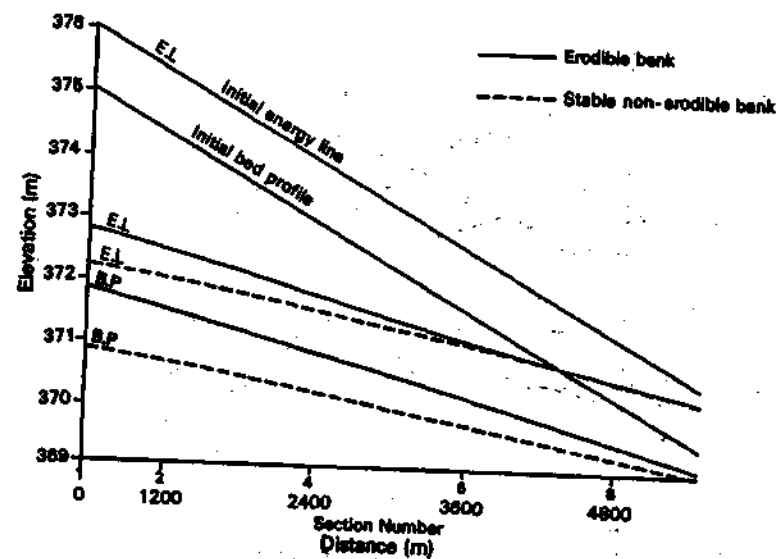
taken from the bed. In particular field examples, other factors, such as armoring, may operate to limit degradation depth.

As shown in Table 1, the amount of sediment contributed by the riverbank at cross section 1 after 60 days was 33% of the total material scoured from the cross section. After 120 days, this figure had risen to 47%, and after 180 days it was still the same. Nearly half of the sediment load was derived from the banks rather than the bed. In addition, the total amount of material scoured from cross section 1 and delivered to the reach downstream when the channel banks were erodible was greater than the amount delivered when the channel width was constant. This resulted in the downstream reaches widening to accommodate the larger sediment-load input from the upstream reaches, as shown in Fig. 2.

The energy line is plotted in Fig. 5, and the stream power of the flow at cross sections 1-9 is plotted in Fig. 6. Fig. 5 shows that as the channel widens, the corresponding energy line remains above that for the case when the channel width was constant. Similarly, Fig. 6 shows that the rate at which the stream power of the flow decreased as the channel widened was lower than that when the channel width was constant. That is, as the bed degraded at a lower rate, the flow energy and stream power remained higher than when the bed degraded faster. Furthermore, at 180 days the sum of the stream power of the cross sections (39.72 N/m·s), i.e., total stream power of the widening channel, is greater than that for when the channel width was constant (37.85 N/m·s). This gives the impression that as the river increased its width, the amount of work done was minimized so that more energy was available to transport the large amount of sediment delivered from upstream reaches or from bank instability at the same cross section.

The conclusions drawn from Figs. 5-6 support the theory of minimum stream power proposed by Chang and Hill (1977). However, the expla-

90 days

180 days

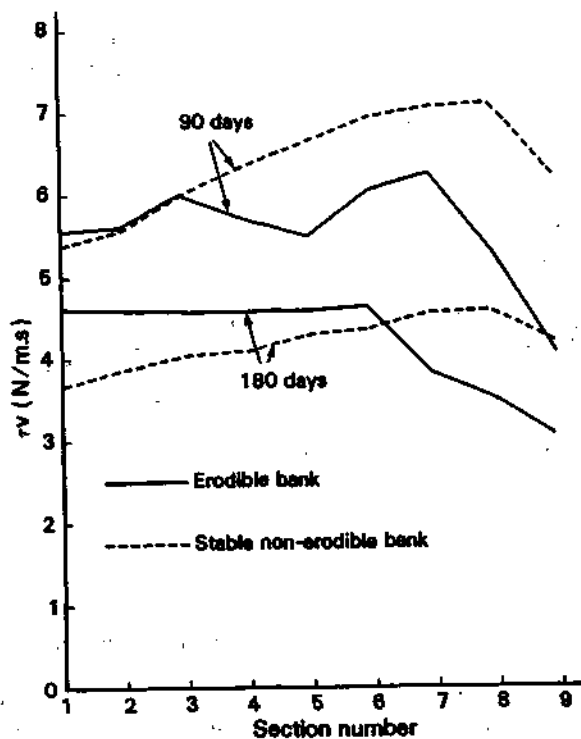——— Erodible bank

------ Stable non-erodible bank

FIG. 6. Stream Power of Flow along Channel

nations and conclusions based on the theory of minimum stream power are questionable because, in fact, as the channel widens more work has to be done to erode the bank laterally in addition to the work needed if the channel width is assumed constant. That is, the energy expenditure is greater as the channel widens than when the channel width remains constant. This appears to contradict what is shown by Figs. 5 and 6. In fact, there is no contradiction between what the figures show and the high energy expenditure entailed in widening. The paradox is resolved by considering the theory of complex response proposed by Schumm (1973).

It has been observed that sediment output from large valleys and watersheds is delivered at a normal rate over a period of time, and then, suddenly, there is a drastic increase in sediment output for a short period of time, after which sediment output is delivered at the normal rate again. The theory explains that this is due to steepening of the bed slope by sediment deposition at the outlet of the catchment area, such that after a while the slope reaches the threshold value for incision. Incision starts, causing the increase in the amount of sediment output. At the same time, incision flattens the bed slope and the deposition starts again, reducing sediment output so that the cycle is repeated.

This phenomenon occurs in watersheds over relatively large time spans, but it also occurs in rivers over relatively short periods. That is, the frequency of the cycle of deposition and scour in rivers is higher than in

160

watersheds. Also, it is possible for complex response to occur in different reaches of a river simultaneously.

In a degrading river with erodible banks, a large amount of sediment is delivered to the downstream reaches as a result of upstream bank failures that occur when bank height reaches the critical or threshold height for mass instability. Consequently, in the downstream reaches, degradation is replaced by aggradation due to the excess of sediment input over local transport capacity. This increases the bed elevation and tends to increase the bed slope downstream of the zone of maximum deposition, so that more energy is available to the flow. The flow uses this additional energy to remove the deposited sediment, thus scouring the bed, decreasing slope, and possibly causing local bank instability, so that the cycle is repeated. The frequency and magnitude of the cycle decreases with a decrease in sediment coming from upstream reaches, producing damped oscillations in sediment output, bed elevation, and stream energy. The cycle of deposition and removal of sediment may operate over a very short time span and may easily pass unobserved.

Hence, in light of the complex response theory, the work done is not minimized, but appears to be small only because part of the energy loss is compensated for by the additional energy input to the flow when the bed slope is increased.

Bank instability leading to channel widening drives this complex response and it is, therefore, not only a function of flow characteristics. The chemical and geotechnical properties of the bank material are the major factors that govern riverbank erosion, as previously discussed. In their present forms, the theories of minimum stream power and of complex response do not take this into consideration explicitly. It is interesting to speculate that the critical bank height for mass failure may represent a geomorphic threshold of equal importance to that of critical bed slope for incision.

RIVERBANK EROSION DUE TO SCOUR IN BENDS

This section shows, using a simple example, that it is important to take into consideration the stability of the outer bank when predicting the transverse bed topography at a channel bend. Existing models predict the equilibrium radial bed profile without considering whether the outer bank height and geometry could be stable with respect to mass failure. In fact, in most rivers, the outer bank fails before the channel bed reaches this equilibrium condition. The channel bend then migrates laterally, with retreat of the outer bank due to lateral erosion and mass failure being balanced by point bar deposition at the inner bank to produce dynamic equilibrium. If point bar deposition does not keep up with outer bank erosion, gradual widening of the channel tends to decrease the outer bank shear stresses until migration slows. Conversely, if bank erosion rates are very slow, inner bank deposition narrows the channel to the point where increased velocities prohibit further deposition. Thus, bank retreat and point bar growth are controlled by both bank erodibility and the quantity of sediment in transport (Howard and Knutson 1984). It is beyond the scope of this study to consider bend distributions of shear stress, velocity, and sediment transport. Consequently, the study is limited to a simple case

161

of outer bank erosion where all other flow parameters are assumed to be known.

Bend Topography Model

Falcon and Kennedy (1983) investigated uniform flow in a curved, wide, erodible-bed channel on the basis of the conservation of flux of moment of momentum, to obtain relations for the vertical distribution of radial plane velocity and radial shear stress. The expression for the radial stress exerted on the bed is used in a force-equilibrium analysis of the moving bed layer to obtain relations for the average transverse slope of the bed and the radial bed profile. The expression for the transverse depth distribution is

$$\left(\frac{d_r}{d_c}\right)^{1/2} = 1 - \left[1 - \left(\frac{r}{r_c}\right)^{1/2}\right] \frac{(8\theta)^{1/2}}{1-\lambda} \frac{1+f^{1/2}}{1+2f^{1/2}} \bar{F} \quad \dots \dots (15)$$

and the average flow depth is found by integrating Eq. 15 over the width to produce

$$\left(\frac{d}{d_c}\right) = 1 - 2\alpha + 2\alpha^2 + \frac{4}{3}(\alpha - \alpha^2) \frac{(r_0^{3/2} - r_i^{3/2})}{r_i^{1/2}(r_0 - r_i)} \quad \dots \dots (16)$$

where

$$\alpha = \bar{F} \frac{(8\theta)^{1/2}}{1-\lambda} \cdot \frac{1+f^{1/2}}{1+2f^{1/2}} \quad \dots \dots (17)$$

$$\bar{F} = \frac{V}{[g(SG-1)D_{50}]^{1/2}} \quad \dots \dots (18)$$

and d_r = flow depth at radial distance r; d_c = central flow depth ($r = r_c$); d = average flow depth; D_{50} = median diameter of bed material; f = Darcy-Weisbach friction factor; g = gravitational acceleration; λ = bed material porosity; r = the radius at which the depth d_r is found; r_c = radius distance to centerline of bend; r_i = inner bank radius; r_0 = outer bank radius; SG = specific gravity of bed material; V = average flow velocity; and θ = Sheilds parameter.

Numerical Example

In the following example, the equilibrium transverse bed profile is predicted using Eq. 15 and then the stability of the bank is checked to determine if such a bed profile is consistent with the stability of the outer bank. Realistic hypothetical data are used in the computations because real data of sufficient detail are unavailable.

1. Channel data are: $Q = 1,000$ m^3/s; $n = 0.023$; $S = 0.00252$; $D_{50} = 0.45$ mm; SG = 2.65; $r_i = 2,100$ m; $r_0 = 2,400$ m; $W = 300$ m; water-surface elevation WL = 150.0 m; and bank elevation BE = 151.51 m.

2. Bank data are: initial bank height $H_0 = 2.8$ m; $i = 83°$; SAR = 1.5; $\Delta\varepsilon = 20$; CONC = 0.250 N; $\gamma = 18.06$ KN/m^3; $c = 11.25$ KN/m^2; and $\phi = 15°$.

162

Flow Computations

$$r_c = \frac{(r_i - r_0)}{2} = 2,250 \text{ m} \quad \dots \dots (19)$$

Compute average shear stress, τ, and uniform flow depth, y_n, for a straight channel reach before the bend, assuming uniform flow as follows:

$$\frac{Q}{W} = \frac{1}{n} y_n^{5/3} S_0^{1/2} \quad \dots \dots (20)$$

$$y_n = \left[\frac{1,000}{300} \times 0.023 \times \frac{1}{(0.00252)^{1/2}}\right]^{3/5} \quad \dots \dots (21)$$

$$y_n = 1.29 \text{ m} \quad \dots \dots (22)$$

$$\tau = \gamma_w y_n S \quad \dots \dots (23a)$$

$$\tau = 1,000 \times 1.29 \times 0.00252 = 3.251 \text{ kg/m}^2 \quad \dots \dots (23b)$$

$$\tau = 31.88 \text{ N/m}^2 \quad \dots \dots (24)$$

$$\frac{r_c}{W} = \frac{2,250}{300} = 7.5 \quad \dots \dots (25)$$

From Fig. 7, with $r_c/W = 7.5$ and $\tau_b/\tau = 1.25$, and the shear stress on the outer bank is found to be:

$$\tau_b = 1.25\tau \quad \dots \dots (26a)$$

$$\tau_b = 39.85 \text{ N/m}^2 \quad \dots \dots (26b)$$

where τ_b = the boundary shear stress on the outer bank. Average flow velocity $V = Q/A = 1,000/300 \times 1.29 = 2.58$ m/s. From the Darcy-Weisbach relation, the friction factor, f, is given by

$$f = \frac{8gRS}{V^2}; \quad R \approx y_n, \quad \text{for wide channel} \quad \dots \dots (27a)$$

$$f = 0.0382 \quad \dots \dots (27b)$$

Compute the porosity using Eq. 6 from this paper:

$$\lambda = 0.245 + \frac{0.0864}{D_{50}^{0.21}}; \quad D_{50} = 0.045 \text{ cm} \quad \dots \dots (28a)$$

$$\lambda = 0.4107 \quad \dots \dots (28b)$$

To compute the flow depth, d_r, at any radius, r, Eq. 15 from this paper is used

$$\left(\frac{d_r}{d_c}\right)^{1/2} = 1 - \left[1 - \left(\frac{r}{r_c}\right)^{1/2}\right] \frac{(8\theta)^{1/2}}{1-\lambda} \frac{1+f^{1/2}}{1+2f^{1/2}} \bar{F} \quad \dots \dots (29)$$
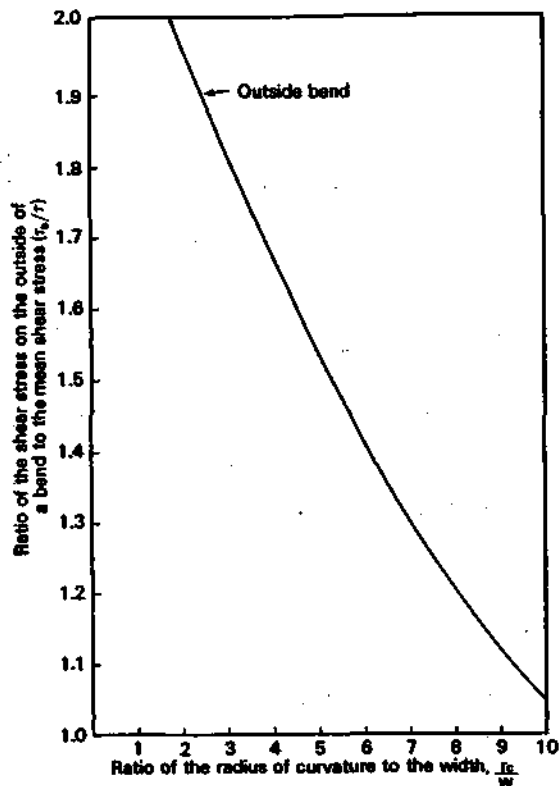
163

FIG. 7. Effect of Bend on Peak Values of Boundary Shear Stress (after Simons et al. 1979)

where

$$\bar{F} = \frac{V}{[g(SG - 1)D_{50}]^{1/2}} \quad \dots \dots \dots \dots \dots \dots \dots \dots \dots \dots \dots (30a)$$

$$\bar{F} = \frac{2.584}{[9.8066(2.65 - 1)0.00045]^{1/2}} \quad \dots \dots \dots \dots \dots \dots \dots (30b)$$

$$\bar{F} = 30.282 \quad \dots \dots \dots \dots \dots \dots \dots \dots \dots \dots \dots \dots \dots \dots (30c)$$

$$\frac{1 + f^{1/2}}{1 + 2f^{1/2}} = 0.86 \quad \dots \dots \dots \dots \dots \dots \dots \dots \dots \dots \dots \dots \dots (31)$$

If Shields parameter $\theta = 0.06$, then

$$\frac{(8\theta)^{1/2}}{1 - \lambda} = 1.1256 \quad \dots \dots \dots \dots \dots \dots \dots \dots \dots \dots \dots \dots (32)$$

164

TABLE 2. Variation in Flow Depth, d_r, and Transverse Bed Elevation, BL, with radial Distance, r, at Bendway

Section number (1)	Variable		
	r (m) (2)	d_r (m) (3)	Bed level (m) (4)
1	2100.00	0.001	149.999
2	2133.29	0.068	149.932
3	2166.59	0.263	149.737
4	2199.89	0.582	149.418
5	2233.19	1.02	148.978
6	2266.48	1.582	148.418
7	2299.78	2.257	147.743
8	2333.08	3.046	146.954
9	2366.37	3.946	146.054
10	2399.67	4.955	145.045

Assuming that d_c can be approximated by the normal flow depth, y_n, then Eq. 15 defined in the present paper becomes

$$d_r = 1.29 \times (0.61762 \, r^{1/2} - 28.30)^2 \quad \dots \dots \dots \dots \dots \dots (33)$$

The bed elevation, BL, at a radius r is given by

$$BL = WL - d_r \quad \dots \dots \dots \dots \dots \dots \dots \dots \dots \dots \dots \dots \dots \dots \dots (34)$$

where WL = the water-surface elevation.

The channel width is divided into 10 sections and the computed values of d_r and BL are shown in Table 2. The corresponding bed level is shown as line AB' in Fig. 8(a).

The outer bank height, H, is given by

$$H = BE - BL = 151.51 - 145.04 = 6.47 \text{ m} \quad \dots \dots \dots \dots \dots \dots (35)$$

Bank Computations

The following computations show that the bank with this height is highly unstable and therefore could not exist. Consequently, the computed equilibrium cross section is unrealistic. In order to find the ratio (H/H') at which the bank becomes unstable, the height H' above point c in Figs. 8(a–b) must be known. According to Figs. 8(a–b), the height H' remains constant since the bank is assumed stable with no lateral erosion when the transverse bed slope is obtained, i.e., $H' = H_0 = 2.8$ m. Eq. 23 from the first paper is applied to obtain the critical ratio (H/H') at which the bank fails. This corresponds to $(H/H') = 1.28$. Hence

$$H = 1.28 \times H' = 1.28 \times 2.8 = 3.57 \text{ m} \quad \dots \dots \dots \dots \dots \dots \dots (36)$$

The outer bank could not ever reach a height of 6.47 m, as this is much greater than the critical height of 3.57 m. Actually, the bank must have
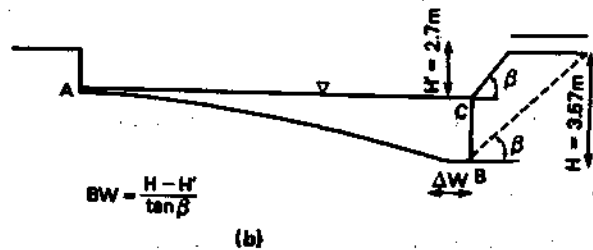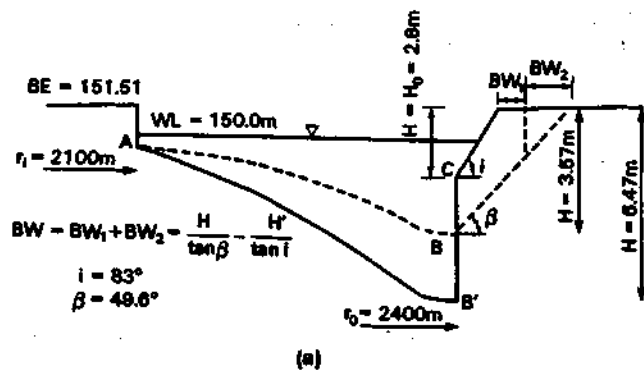
165

FIG. 8. (a) Predicted Equilibrium Transverse Bed Profile in Bendway Ignoring Bank Stability Considerations; (b) Lateral Migration by Parallel Bank Retreat in Bendway with Bank at Point of Failure

collapsed before the bed reached its equilibrium condition [compare bed profiles AB and AB' in Fig. 8(a)].

The new bank angle following the bank failure $i = \beta = 50.3°$. From Eq. 24 from the first paper, the failure block width (no tension cracks) is given by

$$BW = \frac{H}{\tan \beta} - \frac{H'}{\tan i} = \frac{3.57}{\tan 50.3} - \frac{2.80}{\tan 83} \dots \dots \dots \dots \dots \dots \dots (37a)$$

$$BW = 2.62 \text{ m} \dots \dots \dots \dots \dots \dots \dots \dots \dots \dots \dots \dots (37b)$$

Following the initial failure, the reduction in bank angle from i to β makes the bank stable. Assuming that once the bank has failed there will be no further bed lowering, the bend simply migrates laterally as long as the boundary shear stress is greater than the bank material's critical shear stress for entrainment, τ_c. This means that the bank height remains constant at $H = 3.57$ m, and further bank failures are due only to slope steepening by lateral erosion.

Therefore, it is now necessary to find the height, H', at which lateral

erosion again makes the bank unstable. This can be done by rearranging Eq. 23 from the first paper with $i = \beta$ as follows:

$$\left(\frac{H}{H'}\right) = \frac{\left[\frac{\lambda_2}{\lambda_1} + \sqrt{\left(\frac{\lambda_2}{\lambda_1}\right)^2 - 4\left(\frac{\lambda_3}{\lambda_1}\right)}\right]}{2} \dots \dots (38)$$

$$\left(2\frac{H}{H'} - \frac{\lambda_2}{\lambda_1}\right)^2 = \left(\frac{\lambda_2}{\lambda_1}\right)^2 - 4\frac{\lambda_3}{\lambda_1} \dots \dots \dots \dots \dots (39)$$

$$\lambda_1 \frac{H^2}{H'^2} - \frac{H}{H'}\lambda_2 + \lambda_3 = 0 \dots \dots \dots \dots \dots \dots \dots \dots \dots (40)$$

Substitute for $\lambda_2 = 2(1 - K) c/\gamma H'$ from Eq. 20c in the previous paper and rearrange as follows:

$$\frac{1}{H'^2}\left(\lambda_1 H^2 - 2(1 - k)\frac{c}{\gamma}H\right) + \lambda_3 = 0 \dots \dots \dots \dots \dots (41)$$

or

$$H'^2 = \frac{2(1 - K)\frac{c}{\gamma}H - \lambda_1 H^2}{\lambda_3} \dots \dots \dots \dots \dots \dots \dots (42)$$

Now, substituting $K = 0$, $c = 11.25$ KN/m^2, $\gamma = 18.06$ KN/m^3, $\phi = 15°$, $H = 3.57$ m, and $i = \beta = 50.3°$ into equations 20b and 20d from the first paper:

$$\lambda_1 = (1 - K^2)(\cos \beta \sin \beta - \cos^2 \beta \tan \phi) = 0.3821 \dots \dots \dots (43a)$$

$$\lambda_3 = \frac{(\sin \beta \cos \beta \tan \phi - \sin^2 \beta)}{\tan i} = -0.3821 \dots \dots \dots (43b)$$

Substituting into Eq. 42

$$H'^2 = \frac{2(1 - 0)\left(\frac{11.25}{18.06}\right) 3.57 - 0.3821 (3.57)^2}{-0.3821} \dots \dots \dots (44a)$$

$$H'^2 = 1.11 \text{ m}^2 \dots \dots \dots \dots \dots \dots \dots \dots \dots \dots \dots (44b)$$

$$H' = 1.05 \text{ m} \dots \dots \dots \dots \dots \dots \dots \dots \dots \dots \dots (44c)$$

Therefore, the lateral erosion distance, L, required to make the bank unstable is given by

$$L = \frac{H - H'}{\tan \beta} = \frac{3.57 - 1.05}{\tan 50.3} \dots \dots \dots \dots \dots \dots \dots \dots (45a)$$

$$L = 2.08 \text{ m} \dots \dots \dots \dots \dots \dots \dots \dots \dots \dots \dots \dots (45b)$$

and the corresponding failure block width $BW = L = 2.08$ m (parallel bank retreat).

Lateral Erosion Rate

From Fig. 1 in the first paper, if SAR = 1.5, $\Delta\varepsilon$ = 20, and CONC = 0.250 N, then τ_c = 65 dyne/cm^2 = 6.5 N/m^2, and since R = 223× 10^{-4} τ_c $e^{-0.13\tau_c}$ = 0.00031 gm/cm^2-min = 3.04 × 10^{-5} KN/m^2-min, the initial erosion rate, dB (in m/min) = R/γ = 1.68 × 10^{-6} m/min. Since τ_b (=39.85 N/m^2) > τ_c (6.5 N/m^2) the actual erosion rate, dW, is given by

$$dW = 1.683 \times 10^{-6} \left(\frac{\tau_{f_b} - \tau_c}{\tau_c} \right) = 1.683 \times 10^{-6} \left(\frac{39.85 - 6.5}{6.5} \right) \quad \ldots \ldots \text{(46a)}$$

$$dW = 8.64 \times 10^{-6} \text{ m/min} = 0.0124 \text{ m/day} \ldots \ldots \ldots \ldots \ldots \ldots \text{(46b)}$$

The time, T, required for the bank to erode a lateral distance L = 2.08 m, is given by T = 2.08/0.0124 = 167.7 days, or T = 168 days. However, as the channel widens, the shear stress on the outer bank tends to decrease, so that unless point bar deposition matches the bank's erosion rate, the time T needed to erode the bank a lateral distance L increases. Bank erosion ceases when the bank shear, τ_b, is less than τ_c and so would be a discontinuous process in most rivers.

Migration occurs by a cycle of undercutting, which oversteepens and overheightens the bank; mass failure under gravity of blocks about 2 m in width; and basal clean out of slump debris prior to renewed undercutting. The long-term migration rate in the example cited (with a steady discharge) would be about 4.5 m/yr.

Results

At a river bend, it is very important to consider the stability of the outer bank when analyzing the cross-sectional geometry and the migration rate. Many riverbanks fail before the radial profile of the bed reaches an equilibrium condition, and a considerable amount of the flow transport capacity is satisfied from erosion of the outer bank material rather than scouring of the bed. Following mass failure, the more-or-less disturbed failure block comes to rest at the bank toe, but due to the high velocities and high levels of turbulence and boundary shear stress in this area, its residence time there is likely to be short. Even at lower stages (although bed scouring is insignificant) processes of lateral erosion at the outer bank continue to attack slump debris, steepening the lower portion of the bank and leading to mass failures higher up the bank.

The model presented here can be used to explain the commonly observed phenomenon that the depth of scour in a migrating bend increases markedly either when the bend encounters a resistant bank material, or when the bend is stabilized using a revetment. In a migrating bend, the scour pool depth is limited by the critical height of the outer bank and the supply of sediment into the pool by bank erosion and mass failures. The increase in the stability of the bank associated with the increase in bank material strength that occurs when the channel encounters a stiff deposit of clay in the floodplain deposits or bedrock in the valley wall, allows an immediate increase in the scour depth at the outer bank, as the cross section develops towards its equilibrium profile. Similarly, construction of a revetment on an eroding bank in a bendway increases bank stability and reduces the supply of sediment from bank erosion, leading to

the full development of the equilibrium cross section and scouring at the outer bank. In the example used here, stabilization of the outer bank would produce an immediate increase in scour depth from about 3.6 m to about 6.5 m without any pronounced change in bend geometry. This would seem perplexing unless the switch in the control of scour depth from the bank to the stream were recognized. Unless foreseen and accounted for in the initial design, scour of this order could easily result in failure of the revetment by launching. In any given bend, it would be advantageous to know whether the cross-sectional topography and, particularly, the scour pool depth are controlled by bank stability or by flow hydraulics. The model presented here might be useful in this context as it could be used to identify the existing control and to predict the likely increase in scour depth following bank stabilization.

The model presented here is a first step in developing a bend flow model that includes the influence of processes at the outer bank and will allow prediction of meander morphology and its response to changes in either flow hydraulics or bank properties.

Conclusions

As explained in this paper, riverbank retreat is a complicated phenomenon. Simplified assumptions and sometimes severe restrictions have to be imposed on the analysis to produce a practical solution to the problem. In fact, the problem is not only space dependent but also time dependent. Once the bank fails, the decrease of the slope angle and the material deposited at the bank toe increase the stability of the slope. The removal of the failure material depends largely on how stiff and erosion-resistant the bank soil is in its disturbed state and on the magnitude of the discharge. During periods of dry weather and low flows, the bank may remain stable even though it is liable to fail under unfavorable conditions of high moisture content and rapid drawdown. Often, failure takes place during the recession limb of a flow hydrograph due to an increase in the pore water pressure. In such circumstances, the failure material may remain at the bank toe until the next season's high discharge. While in place, the failed material protects the intact bank from the flow and increases the stability by buttressing, but it also restricts the water course in small streams and may increase the erosion rate of the opposite bank due to the diversion of the core of high flow velocity.

The amount of bank sediment contributed to the total load of the river depends not only on the geometry of the cross section and the boundary flow shear, but also on the distribution and types of material in the cross section. Gravel and cobble-bed rivers with noncohesive sand or gravel banks show high rates of lateral erosion compared to bed scouring. In such cases, a large percentage of the total sediment is contributed by the banks. By contrast, in sand-bed rivers with cohesive banks, most of the total load comes from the bed. Although bed scouring reduces the stability of the riverbanks, the input of bank sediment takes place over a longer time span than that for gravel and cobble-bed rivers with noncohesive banks. This is because for noncohesive banks, the erosion process is almost continuous, while for cohesive banks more material comes from failed blocks at the bank foot following mass instability. Gravel and cobble-bed rivers with

stratified or composite banks commonly exhibit bank failure by undermining of cantilevers (Thorne 1982), so that bank retreat proceeds by a combination of almost continuous flow erosion of the lower bank and intermittent basal clean out of slump debris from the upper bank.

Depending on the type of bank material and the processes and mechanisms of erosion, the amount of sediment delivered downstream of the eroded sections can seriously affect the geometry and flow hydraulics of the downstream reaches and may trigger cycles of complex response. When the banks are highly erosive, the large amount of sediment contributed causes the river width downstream to increase in order to accommodate the greater amount of sediment input from the upstream sections. At such reaches, channel widening causes more land losses, as has happened recently in the northern part of Sudan, resulting in serious socioeconomic problems for the floodplain users.

Vegetation may increase or decrease the stability of the riverbank. The roots of plants, small trees, and grasses act as a reinforcement of the bank soil, but big trees are additional weights to the bank that decease the stability of steep slopes. It is extremely difficult to incorporate the effects of vegetation into a bank stability analysis because these effects vary with the seasons and the degree of development of the plants. Also, plants introduce new complications in the form of anisotropic bank material properties and random variations in soil properties that cannot easily be accounted for. In the present analysis, vegetation effects must be accounted for by adjusting the bank material properties γ, c', and ϕ'. Yet, if bank retreat in natural channels is to be better explained, it may be essential to incorporate vegetation effects explicitly, as these seem to play a major role in the control of channel width in stable rivers (Hey and Thorne 1986).

APPENDIX I. REFERENCES

Bagnold, R. A. (1966). "An approach to the sediment transport problem form general physics." *U.S. Geol. Survey Prof. Paper 422-I.* 137 pp.
Chang, H. H. (1982). "Mathematical model for erodible channels." *J. Hydr. Div.*, ASCE, 108(5), 678–689.
Chang, H. H., and Hill, J. C. (1977). "Minimum stream power for rivers and deltas." *J. Hydr. Div.*, ASCE, 103(12), 1375–1389.
Engelund, F., and Hansen, E. (1967). "A monograph on sediment transport in alluvial streams." Teknisk Vorlag, Copenhagen, Denmark.
Falcon, M. A., and Kennedy, J. F. (1983). "Flow in alluvial-river curves." *J. Fluid Mech.*, 133, 1–16.
Gessler, J. (1971). "Aggradation and degradation." *River mechanics*, 1, Chapter 8, H. W. Shen, ed., John Wiley and Sons, New York, N.Y.

Hey, R. D., and Thorne, C. R. (1986). "Stable rivers with mobile gravel beds." *J. Hydr. Engrg.*, ASCE, 12(8), 671–689.
Howard, A. D., and Knutson, T. R. (1984). "Sufficient conditions for river meandering: A simulation approach." *Water Resour. Res.*, 20(11), 1659–1667.
Komura, S., and Simons, D. B. (1967). "River-bed degradation below dams." *J. Hydr. Div.*, ASCE, 93(4), 1–13.
Schumm, S. A. (1973). "Geomorphic thresholds and the complex response of drainage systems." *Fluvial geomorphology*, M. Morisawa, ed., Binghampton Series, George Allen and Unwin, London, U.K.
Simons, D. B., et al. (1979). "Connecticut river streambank erosion study." *Report to U.S. Army Corps of Engineers*, Waltham, Mass.
Thorne, C. R. (1982). "Processes and mechanics of bank erosion." *Gravel-bed rivers, fluvial processes, engineering and management*, R. D. Hey, J. C. Bathurst, and C. R. Thorne, eds., John Wiley and Sons, Chichester, U.K.

APPENDIX II. NOTATION

The following symbols are used in this paper:

B.C.	=	boundary conditions;
BE	=	bank elevation;
BL	=	bed elevation;
BW	=	failure block width;
CONC	=	pore fluid salt concentration in bank material;
c	=	cohesion, incorporating FS;
c'	=	effective cohesion;
D_{50}	=	median diameter of bed material;
D_L	=	largest bed sediment particle diameter;
D_s	=	bed material median fall diameter;
d	=	average flow depth;
dB	=	initial lateral erosion rate;
d_r	=	average flow depth at radial distance, r;
d_c	=	central flow depth;
f	=	friction factor;
ER	=	lateral erosion rate;
FS	=	factor of safety;
g	=	gravitational acceleration;
H	=	bank height above bed;
H'	=	bank height above zone of lateral erosion;
$(H/H')_c$	=	calculated (critical) bank-height ratio;
$(H/H')_m$	=	measured (observed) bank-height ratio;
H_0	=	initial bank height;
i	=	bank angle;
i_0	=	initial bank angle;
j	=	cross section number
K	=	ratio of tension crack depth to bank height;
L	=	lateral erosion distance required to cause mass bank failure;
n	=	Manning's coefficient;
Q	=	volumetric discharge;
Q_b	=	volume of bed material scoured;
Q_s	=	sediment discharge;
q	=	unit discharge;

q_s = unit sediment discharge;
r = radius of curvature at bend;
r_c = radius of curvature of channel centerline at bend;
r_i = radius of inner bank at bend;
r_0 = radius of outer bank at bend;
R = rate of soil erosion;
RT = removal time;
S = energy slope;
S_0 = initial bed slope;
SAR = sodium adsorption ratio of bank material;
SG = specific gravity of bed material;
t = time;
V = average velocity;
VB = volume of failure block per unit channel length;
VL = laterally eroded volume per unit channel length;
W = channel width;
WL = water surface elevation;
X = downstream distance;
y_n = normal flow depth;
Z = bed elevation;
$Z_1 \ldots Z_N$ = initial bed profile;
β = angle that failure surface makes with horizontal;
$\Delta \varepsilon$ = dielectric dispersion of bank material;
Δt = time step;
ΔW = lateral erosion distance;
ΔZ = degradation depth;
γ = unit weight of bank material;
γ_s = unit weight of bed material;
γ_w = unit weight of water;
λ = bed material porosity;
ϕ = angle of internal friction, incorporating FS;
ϕ' = effective angle of internal friction;
τ_b = flow shear stress on outer bank in bendway;
τ_c = critical flow shear stress for entrainment of bank material;
τ = average boundary shear stress;
τ_f = bank shear stress;
τ_{fc} = critical flow shear stress for entrainment of bed material;
τv = stream power per unit bed area; and
θ = Shields parameter.

CATION EXCHANGE IN GROUNDWATER SOLUTE TRANSPORT[a]

By Kenneth A. Rainwater,[1] Associate Member, ASCE

ABSTRACT: The transport and fate of pollutants in groundwater is an important environmental concern. Adsorption processes, such as cation exchange, affect the movement of many contaminants. Accurate modeling of these processes is necessary for the design of efficient aquifer restoration methods. That accuracy depends on both the mathematical description of the transport process and the quantification of the effective adsorption parameters. The objectives of this study were: (1) to formulate a procedure for estimating effective aquifer adsorption parameters in situ, and (2) to test the procedure in controlled laboratory experiments. The parameter estimation procedure used a groundwater contaminant transport model combined with a nonlinear parameter estimation technique. Two- and three-component cation exchange experiments were performed in a two-dimensional injection-production flow apparatus. The parameter estimation procedure computed effective exchange parameters that were consistent for all of the experiments.

INTRODUCTION

The identification and restoration of contaminated groundwater sites is of growing concern today. Pollution sources include accidental spills of toxic materials (Roberts et al. 1982), poorly managed waste disposal projects (Dance and Reardon 1983), and in situ mining techniques (Paul et al. 1983). Once a contaminated area has been identified, three general alternatives are available to prevent further damage. These include physical containment by structural or hydrodynamic barriers, withdrawal and treatment of the contaminated groundwater, and aquifer rehabilitation by in situ treatment to neutralize contaminants. These methods may be employed independently or in combination. In each method, the mobility of the contaminants must be understood. The latter two alternatives also require accurate modeling of the physical and chemical processes that affect groundwater contaminant migration for design of efficient and cost-effective restoration procedures.

The complex nature of groundwater flow and the interaction of contaminant species with heterogeneous porous media have led researchers to develop sophisticated theoretical and numerical models for the general transport problem. These models often include hydraulic parameters, such as hydraulic conductivity and dispersion tensors, which are difficult to establish accurately for a given site with current laboratory and field techniques. The parameters used to describe adsorption processes, such as cation exchange and physical sorption, which affect solute transport in

Attachment 2
RFI Report Section 8.8.1.9

QEA
Quantitative Environmental Analysis, LLC
$\partial c/\partial t$

change at Reach 5B. This statement is further supported by the absence of bed load at the Reach 5B monitoring locations during the EPA May 2002 storm event.

EPA conducted additional bed load sampling at New Lenox Road during a March 2003 storm event (peak 15-minute flow at the USGS gage in Coltsville of 2,100 cfs). This sampling event was limited compared to the May 2002 event in that only a single bed load sample was taken and no water column samples were collected. In contrast to the May 2002 event, bed load transport was observed at New Lenox Road, indicating that, at the much higher flows experienced during this event, bed load transport extends beyond this location. As expected, the materials sampled during the March 2003 event were coarse sediments, with a D-50 of approximately 700 μm. If the bed load rate measured by the single sample (~17 MT/d – see Appendix E.8 for calculation method) is representative of the average during the 2-day elevated flow event, the estimated sediment bed load sums to about 33 MT. This value is difficult to put into perspective because sampling was not conducted in the water column or at the upstream stations during this event. However, it should be noted that this value represents less than one percent of the 4,170 MT annual average suspended sediment load passing this location (Table 8-1). The measured PCB concentration on this sediment bed load sample was 2.4 mg/kg, which is consistent with that of coarse grained sediments from Reach 5B (e.g., Figure 4-16).

8.8.1.9 Bank Erosion

Bank erosion is primarily caused by two processes: fluvial entrainment and subaerial/subaqueous weakening and weathering. Bank retreat occurs as a result of entrainment of material directly from bank scour. Bank failure is caused by weakening and weathering processes that decrease bank stability. The rate of bank erosion at a particular location depends on the forces acting on the bank (e.g., applied shear stress from moving water), the bank properties (e.g., type of sediment, grain size distribution, stratigraphy, type, and density of vegetation), as well as the slope of the bank.

To evaluate bank erosion, EPA installed groups of toe pins on October 5, 2000 in the bank at five locations along an approximately 2,000-foot-long reach of the River near RM 130. The toe pins were used to measure bank elevations at four different times over an approximately 20-month period, with the last data collected on June 21, 2002. For the 20-month period from October 2000 to June 2002, average bank erosion rates for the five groups of toe pins ranged from about -0.3 foot per year (ft/yr) to -0.8 ft/yr,

BLASLAND, BOUCK & LEE, INC.   Quantitative Environmental Analysis, LLC

9/26/03   *engineers & scientists*   8-41
V:\GE_Housatonic_Rest_of_River\Reports and Presentations\RFI Report - Sept Final\70031550 RFI Report.doc

with an overall average rate of -0.7 ft/yr (15 observations). It should be noted that the overall average rate for the reach would be lower because these measurements were taken in areas that were visually identified to be undergoing active bank erosion.

In addition, EPA conducted a study to evaluate the migration of riverbanks at 15 locations in Reaches 5A and 5B, shown on Figure 8-28. Bank location data (i.e., top- and bottom-of-bank) were collected along 15 riverbank stretches that ranged in length from approximately 140 feet to 525 feet. The bank location data were obtained at two different times: November 5, 2001 and June 17, 2002. The top- and bottom-of-bank locations were analyzed to determine average changes in bank location during this seven-month period. Average bank erosion occurred for 10 of the 15 bank sections, with mean erosion rates for individual sections ranging from -0.03 ft/yr to -3.0 ft/yr (Figure 8-28). The overall average erosion rate for these 10 eroding bank sections was -0.7 ft/yr, which is the same average erosion rate determined from the toe pin data. The remaining five bank sections experienced net accretion, on average, with accretion rates of 0.07 ft/yr to 2.9 ft/yr and an overall average accretion rate of 1.0 ft/yr. For all 15 bank sections, average erosion occurred during this seven-month period, at a mean rate of -0.3 ft/yr, which is about a factor of two lower than the average of the toe pin erosion rate data. Again, these values are not necessarily representative of Reaches 5A and 5B as a whole because specific bends where bank erosion is more likely to occur were targeted in these surveys.

Based on previous qualitative observations of the riverbank, EPA produced maps in 1998 depicting approximate locations and extent of active bank erosion along the River channel in Reach 5. These maps were used to develop an estimate of the length of bank that is experiencing active bank erosion between the Confluence and New Lenox Road Bridge, which totaled approximately 13,400 feet. This information was used to estimate the annual sediment mass load to the River from bank erosion based on the equation presented in Appendix E.6. The result of this estimate is a range of about 1,400 MT/yr to 3,200 MT/yr of sediment load to the River from bank erosion.

These approximate bank erosion load estimates, when compared to the estimated sediment loadings entering at the Confluence (~1,500 MT/yr for the West Branch and 2,200 MT/yr in the East Branch – see Table 8.1) and at New Lenox Road Bridge (~4,200 MT/yr), suggest that bank erosion may be a significant source of sediment to the River on an annual basis. Comparison of the suspended load values with the bank erosion load estimates suggests that the average bank erosion rate between the Confluence and New Lenox Road Bridge is likely not consistent with the upper end of the average range measured by

EPA (i.e., 0.7 ft/yr), but could be near the lower end (i.e., 0.3 ft/yr). It should be noted, however, that not all material eroded from the banks will be transported as suspended load, as some portion will remain near where it slumped or eroded into the river. To the extent that this occurs, the range of load estimates discussed above (i.e., 1,400 to 3,200 MT/yr) would be lower.

8.8.1.10 River Meanders

Meandering is caused by bank erosion on the outside of a river bend, where current velocities are relatively high, and deposition on the inside of the bend, where velocities are relatively low. Generally, the extent, rate and type of meandering depend on channel gradient, flow rates in a river, channel bed properties, and soil properties of the bank and floodplain. When viewed on a reach scale, meandering is a stochastic process, with the channel moving within the meander belt between the edges of the floodplain. In many rivers, the cross-sectional area of the River will remain approximately constant at a particular location even though the channel is moving laterally as it meanders. In addition, the lateral migration of the channel is typically a major component of the floodplain aggradation process, with deposition during overbank floods being a minor component of that process.

The River channel between the Confluence and Woods Pond headwaters tends to meander, with the extent of meandering and width of the meander belt being spatially variable between these locations. Past meandering is evident from the existence of abandoned oxbows, connected and disconnected backwaters, and cutoffs in the proximal and distal floodplain. Evaluation of channel width:depth ratios (Section 2) indicates that Reach 5A channel is classified as sinuous (between straight and minimally meandering), Reach 5B is minimally meandering, and Reach 5C has a moderately meandering channel.

As part of a river meandering study, EPA generated digital shorelines from aerial photography in 1952, 1978, and 2000 to supplement aerial photographs generated by GE in 1990. Qualitative comparison of changes in channel location in the study area between 1990 and 2000 suggests that channel migration during this 10-year period was not extensive, with a relatively stable channel existing in most locations. A small number of meanders and channel sections, however, did experience significant movement during this 10-year period. On a longer time scale, a qualitative evaluation of shoreline location change over the 48-year period between 1952 and 2000 is consistent with the 1990-2000 assessment, as shown on Figure 8-29. Overall, it appears that the River channel has been relatively stable during the past 50 years, with significant channel migration (e.g., meander cutoffs) occurring only at a few locations (e.g., see inset map

Attachment 3
RFI Report Figure 9-2

QEA
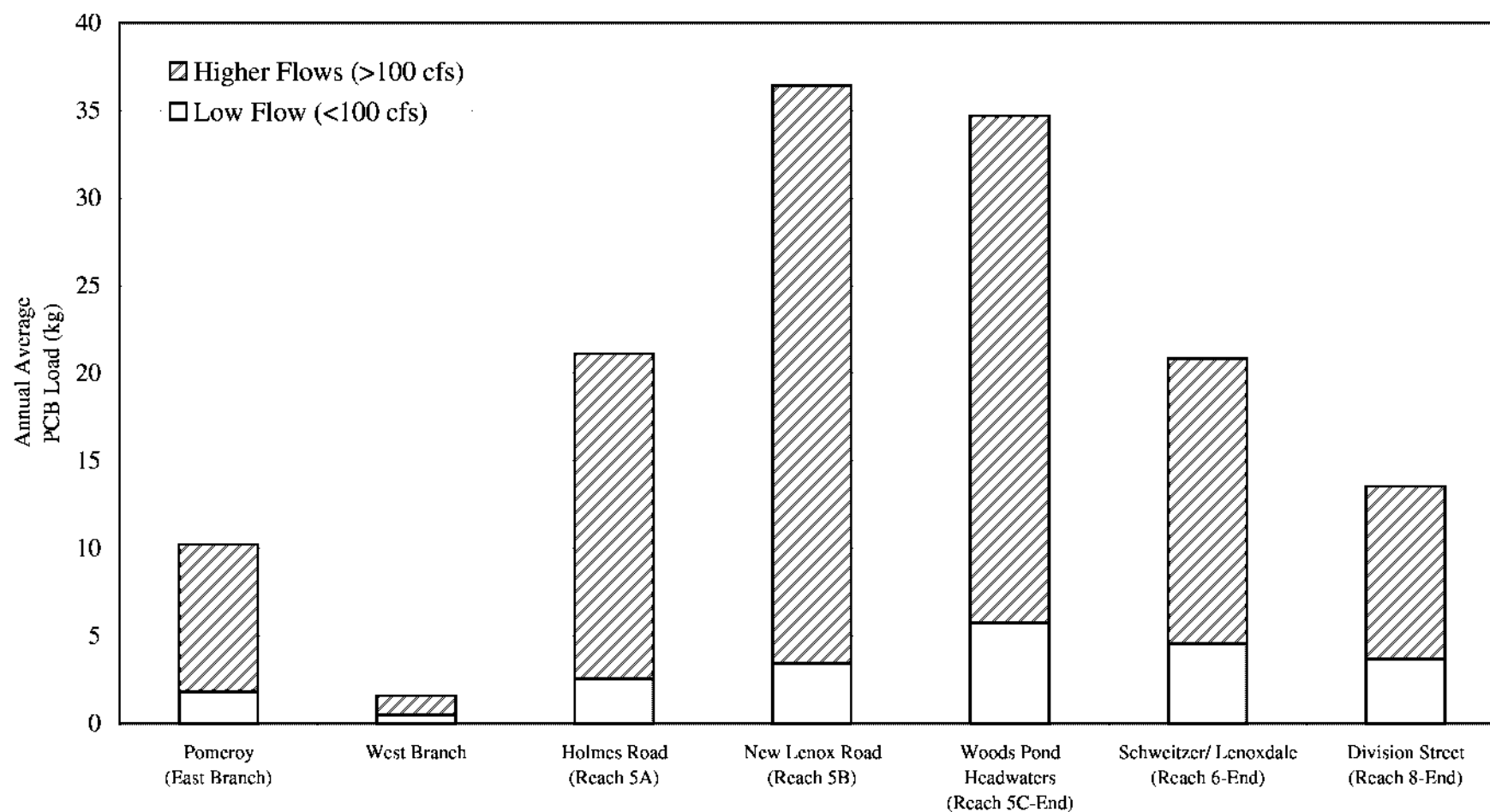Quantitative Environmental Analysis, LLC
∂c/∂t

Figure 9-2. Summary of annual average PCB loadings at various locations along the Housatonic River.

Notes: Loads calculated using non-detects at 1/2 the MDL; high/low flow based on cutoff of 100 cfs at Coltsville.

Attachment 4
RFI Report Section 4.5.4 and
Figures 4-21, 4-22, 4-23, and 4-26

high concentration samples is observed in some of the larger backwaters in the vicinity of Woods Pond Headwaters.

4.5.4 Geochronologic Analysis and Sedimentation

Several cores collected throughout the system were segmented into much finer increments than the 6-inch intervals discussed thus far, and were analyzed for radioisotopes to facilitate the estimation of depositional rates. Since 1995, GE and EPA have collected a total of 32 sediment cores for radioisotope analysis (i.e., Cs-137) in addition to the typical suite of PCB, TOC, and solids analyses. Analysis of Cs-137 allows for the dating of sediment layers and estimation of deposition rates since the 1950s, due to fallout activity from open-air nuclear testing that was initiated in 1955 and peaked around 1963 (Pennington, 1973). Atmospheric Cs-137 fallout was a byproduct of these nuclear tests, and Cs-137 data from finely-sectioned sediment cores reflects the historical fallout chronology and allows for the identification of two distinct chronological markers. The 1954 horizon is indicated by the first (deepest) transition from non-detect to detectable Cs-137 activity and the 1963 horizon is represented by the peak Cs-137 concentration. Identifying the depth of these horizons then allows for the estimation of the average rate of net sediment deposition that has occurred since that time.

In addition to Cs-137, the finely-sectioned sediment cores collected by EPA in 1998 and 1999 were analyzed for two other naturally occurring radioisotopes: Lead-210 (Pb-210) and Beryllium-7 (Be-7). Analysis of Pb-210 (half-life 22.3 years) allows for a reasonably reliable dating of sediment deposited over the last 100-150 years (Krishnaswami et al., 1971). Moreover, if sediment mixing is minor, the Pb-210 dating can provide information on the rate of sedimentation. Be-7 (half-life of 53 days) is generally found only in the top few centimeters of sediment due to its short half-life. Analysis of Be-7 provides information on sediment mixing (i.e., Be-7 in the subsurface would likely indicate mixing) and the integrity of the core collection.

To date, a total of 32 cores have been collected for geochronologic analysis from sediment deposits in Reach 5, the backwater areas, Woods Pond, and three impoundments downstream of Woods Pond. The results of geochronologic analysis of 17 of these sediment cores collected from Reach 5, backwater areas, and Woods Pond in 1995 were reported in the prior RFI Report (BBL, 1996). Due to some minor changes in reported concentrations as a result of data validation in 2002, the results and concentration

BLASLAND, BOUCK & LEE, INC.
9/26/03   engineers & scientists
V:\GE_Housatonic_Rest_of_River\Reports and Presentations\RFI Report - Sept Final\70031550 RFI Report.doc

Quantitative Environmental Analysis, LLC
4-27

profiles are included again in the following section. However, the overall conclusions presented in the 1996 RFI Report did not change, and in fact are further supported by subsequent data. These conclusions are:

- Estimated deposition rates are relatively variable depending on whether the cores were taken from a predominantly depositional area or from an area subject to erosion or little deposition. Cores collected from predominantly depositional areas were more suitable for estimating sediment deposition rates (as opposed to those collected from the channel).

- Overall, in cores with interpretable Cs-137 profiles, the observed peak PCB concentration was generally associated with the peak Cs-137 concentration, indicating a general decline in PCB transport and deposition over time.

The simplest method to interpret sediment core Cs-137 data is to identify the depth of the peak activity and divide that depth by the number of years since that 1963 peak has occurred, to yield an annual average net sedimentation rate. Alternatively, sedimentation rates may also be calculated by dividing the depth of the first detectable Cs-137 concentration by the number of years since the first detect occurred in 1954. While both methods are an adequate approximation of deposition, they do not account for variations in sediment mixing, compaction of deeper sediments, sediment disturbance or anomalous processes caused by hydrologic events (e.g., short-term extreme erosion or deposition), bioturbation, or other factors. Thus, qualitatively, cores collected in areas of consistent deposition will produce the best estimates of sediment chronology; those cores will exhibit a smooth, uninterrupted peak of Cs-137 activity and gradual decline toward the sediment surface. For the Housatonic River geochronologic cores, a majority of the cores collected from Woods Pond and the backwater areas fit this description, while those collected from the channels and terraces (in Reach 5) produced results that are more variable and difficult to interpret. Given the variability in the data, deposition rates for interpretable cores were calculated using both methods discussed above and are summarized in Table 4-9.

BLASLAND, BOUCK & LEE, INC.   Quantitative Environmental Analysis, LLC

9/26/03   engineers & scientists   4-28
V:\GE_Housatonic_Rest_of_River\Reports and Presentations\RFI Report - Sept Final\70031550 RFI Report.doc

Table 4-9. Calculated Deposition Rates for Finely-Sectioned Cores

Source	Location	Core ID	Depth (cm) First Detectable Cs-137	Depth (cm) Peak Cs-137	Deposition Rate (cm/yr) First Detectable Cs-137	Deposition Rate (cm/yr) Peak Cs-137
1995 GE	Reach 5A	4-7F	1	1	*NI*	*NI*
	Reach 5A	5-3A	65	44	1.6	1.4
	Reach 5B	6-1B	70	39	1.7	1.2
	Reach 5B-BW	6-2E	32	6	0.8	0.2
	Reach 5C	6-2G	6	6	0.1	0.2
	Reach 5C-BW	6-2N	37	6	0.9	0.2
	Reach 5C-BW	7-1F	22	17	0.5	0.5
	Reach 5C-BW	7-1J	6	4	0.1	0.1
	Reach 5C-BW	7-1Q	6	4	0.1	0.1
	Reach 5C-BW	7-1U	6	1	*NI*	*NI*
	Reach 5C-BW	7-1X	22	6	0.5	0.2
	Reach 6	WP-1	22	14	0.5	0.4
	Reach 6	WP-2	22	14	0.5	0.4
	Reach 6	WP-3	6	6	0.1	0.2
	Reach 6	WP-5	44	29	1.1	0.9
	Reach 6	WP-6	29	14	0.7	0.4
	Reach 6	WP-7	>70	>70	*NI*	*NI*
1998-99 EPA	Reach 6	H4-SE001004	>50	3	*NI*	*NI*
	Reach 6	H4-SE001007	32	11	0.7	0.3
	Reach 6	H4-SE001008	60	1	*NI*	*NI*
	Reach 6	H4-SE001011	24	5	0.5	0.1
	Reach 6	H4-SE001012	90	20	2.0	0.6
	Reach 6	H4-SE001013	44	16	1.0	0.4
	Reach 6	H4-SE001014	50	5	1.1	0.1
	Reach 6	H4-SE001015	24	9	0.5	0.3
	Reach 6	H4-SE001016	24	1	*NI*	*NI*
1998 GE	Rising Pond	RPD-CS-01	76	36	1.7	1.0
	Rising Pond	RPD-CS-02	60	28	1.4	0.8
	Falls Village	FVD-CS-01	16	1	*NI*	*NI*
	Falls Village	FVD-CS-03	>109	20	*NI*	*NI*
	Bulls Bridge	BBD-CS-01	16	16	*NI*	*NI*
	Bulls Bridge	BBD-CS-02	64	46	1.5	1.3

NI = Deposition rate not calculated because Cs-137 profile difficult to interpret (results are shaded gray in the table)

(>) = indicates that first detectable or peak concentration was somewhere below last core segment collected

It is important to note that the deposition rates listed in Table 4-9 are not necessarily representative of entire reaches because these cores were intentionally collected from depositional areas. This results in an estimated average deposition rate that is likely somewhat higher than the true reach average deposition rate. It should also be noted that for nearly all cores, the deposition rate calculated based on the first detectable concentration in 1954 is higher than that based on the 1963 peak. To simplify the discussion in the remainder of this section, deposition rates calculated based on the 1963 peak method are the only values presented unless otherwise indicated.

BLASLAND, BOUCK & LEE, INC.   Quantitative Environmental Analysis, LLC

9/26/03   *engineers & scientists*   4-29
V:\GE_Housatonic_Rest_of_River\Reports and Presentations\RFI Report - Sept Final\70031550 RFI Report.doc

Cs-137 and PCB results for the geochronologic cores are shown on Figures 4-21 through 4-23. Of the four geochronologic cores collected from the River channel (all in 1995), three produced interpretable results: one from a terrace deposit in Reach 5A (core 5-3A; Figure 4-21a), and one each from sediment deposits in Reaches 5B and 5C (cores 6-1B and 6-2G, respectively; Figure 4-21a). The Reach 5A terrace deposit core produced an average sedimentation rate of 1.4 centimeters per year (cm/yr), and the Reach 5B and 5C sediment deposits exhibited deposition rates of 1.2 cm/yr and 0.20 cm/yr, respectively. In all three cases, the PCB concentration was highest at depths of 15 cm or more, and was substantially lower at the sediment surface than the maximum within the core.

The most thorough geochronologic sampling in the Housatonic River was performed in Woods Pond, from which 15 cores were collected (six by GE in 1995 and nine by EPA in 1999). Of the 15 cores, 11 produced largely undisturbed interpretable Cs-137 profiles (Figures 4-21c and 4-22). One core from 1995 (WP-7) was not interpreted because the highest Cs-137 activity was in the deepest sampling increment, at 70 cm, suggesting that the core did not extend deep enough to capture the whole profile. In the 11 cores with interpretable Cs-137 profiles, the identified 1963 horizon was identified at depths ranging from 5 cm to 29 cm, and resulted in annual net deposition rates of 0.14 to 0.91 cm/yr, with an average of 0.39 cm/yr (Figures 4-21c and 4-22). However, a qualitative assessment of the Cs-137 data reveals that, in general, the profiles from cores collected in 1999 contain much more variability than those collected in 1995 (see Figure 4-22), and hence their interpretation is more questionable. The Cs-137 peaks in the 1999 cores are often near the surface, even though Cs-137 extends well beneath that depth in the core; thus, using the peak Cs-137 only to produce a chronology in those cores may underestimate the true sedimentation rate. The average deposition rate for the 1995 Woods Pond cores based on the peak Cs-137 is 0.49 cm/yr. The average Woods Pond deposition rate calculated based on the 1954 first detection is somewhat higher at a value of 0.60 cm/yr. The average deposition rate from the 1995 cores may be a more accurate estimate of overall net deposition in Woods Pond than the average deposition rate calculated from the 1999 cores because the results are much more consistent between cores in 1995. Of the five interpretable cores collected from Woods Pond in 1995, four exhibit sharp gradients in PCB concentration within the top 15 cm, increasing to a distinct peak between 10 and 50 cm. PCB peak depth is variable in the nine cores collected by EPA in 1999, and is not distinct in three of these cores. Three of the EPA cores have a PCB peak at or near the surface, while the remaining three cores have a peak between 10 and 35 cm.

The nine geochronologic cores collected by EPA from Woods Pond in 1998 and 1999 were also analyzed for Pb-210 and Be-7. These isotope data were generally inconclusive due to the highly variable and sometimes conflicting results. Only three of the Woods Pond cores had Be-7 in the surface samples, suggesting both that these three locations had experienced recent deposition, and that the other cores were either disturbed during collection or were from areas where recent deposition had not occurred. Three cores, including one of the above, contained Be-7 in subsurface samples, which suggests that the integrity of the samples were compromised during collection or handling. The Pb-210 results, on the other hand, were interpretable in 7 of 9 cores. These data results and profiles are presented in the SI Data Report (Weston, 2002). The dating of these cores based on Pb-210 varied greatly among locations, and generally showed faster rates of deposition (between 0.4 cm/yr and 4 cm/yr) than indicated by the Cs-137 results for those cores.

Cores collected from backwater areas consistently show a very low net rate of sediment deposition. Six of the seven cores collected (all collected in 1995) produced interpretable Cs-137 profiles, one from Reach 5B (core 6-2E; Figure 4-21a) and five of six cores collected in Reach 5C (Figures 4-21a and 4-21b). The Cs-137 peak associated with the 1963 horizon was observed between 4 and 17 cm depth in all cases, resulting in average deposition rates ranging between 0.13 and 0.53 cm, with an average of 0.21 cm/yr (or 0.51 cm/yr based on 1954 first detect). Although two of the six cores contain somewhat questionable profiles, the average rate among the four cores with clearly defined Cs-137 profiles is 0.24 cm/yr, about half the rate observed in Woods Pond. PCB peak depths in the backwater cores generally range between 5 and 40 cm and are similar in depth to the Cs-137 peak. Two of the seven cores have PCB peaks near the surface, consistent with the Cs-137 concentrations in these cores. The presence of a PCB and Cs-137 peak near the surface further suggests that these backwater locations have lower deposition rates than those observed in Woods Pond.

Downstream of Woods Pond Dam, GE collected 6 cores for geochronologic analysis, of which two from Rising Pond and one from Bulls Bridge impoundment were interpretable (Figure 4-23). In Rising Pond, the Cs-137 peaks were detected at depths of 28 cm and 36 cm, resulting in approximate sedimentation rates of 0.8 cm/yr and 1.0 cm/yr. The deposition rate for the Bulls Bridge impoundment core was estimated to be 1.3 cm/yr. Overall, the estimated deposition rates for these impoundments are generally higher than, but not inconsistent with, the estimates for Woods Pond, and reflect the depositional nature of impoundments. For the two cores collected from Rising Pond, PCB concentrations in the top 15 cm

are typically less than 10 mg/kg and distinct peaks within the range of 25-30 mg/kg are observed at depths of 35 and 50 cm. PCB concentrations in the Bulls Bridge impoundment core are considerably lower and more variable, with PCB concentrations less than 1 mg/kg within the top 15 cm, and a peak concentration of approximately 2.5 mg/kg at a depth of 45 cm.

4.5.5 PCBs in Sediment Pore Water

In fall 2001, EPA and GE conducted a joint sampling program to evaluate PCB partitioning characteristics (described in Appendix A). This program included PCB analysis of pore water extracted from surface sediment (0- to 6-inch) core samples. PCB concentrations in sediment pore water ranged from 0.4 μg/L to 8.1 μg/L, with an overall average of 2.2 μg/L (Figure 4-24). On average, pore water PCB concentrations were lower in Reach 5A than in Reaches 5B and 5C. Lower concentrations were also observed in the samples from Woods Pond. These differences are related to differences in the concentrations of DOC in the pore water as well as PCB and TOC in the local sediments, and are discussed further, in the context of PCB partitioning, in Section 8.

4.6 Temporal Trends in Sediment PCB Concentrations

Comparison of the historical and recent surface sediment PCB data can provide an indication of temporal trends in PCB transport and deposition in the Housatonic River. Sediment samples have been collected from the Housatonic River at many different locations and for many different reasons since the late 1970s. As noted above, the locations of the samples collected can have a significant impact on the expected or observed sediment PCB concentrations (e.g., sediment collected from an area of fine sediment deposition may be more likely to have higher concentrations of PCB). Therefore, to properly assess changes in PCBs in sediment over time, it is important to maximize the comparability of sample locations. Based on a qualitative comparison of historical and more recent sample locations, Woods Pond and Rising Pond provide the most robust datasets. For this reason, these impoundments were selected for an evaluation of temporal trends in surface sediment PCB concentration. Due to the depositional nature of these impounded areas, changes in surface sediment PCB concentrations over time can provide insight into the changes in deposition and transport within the respective upstream reaches.
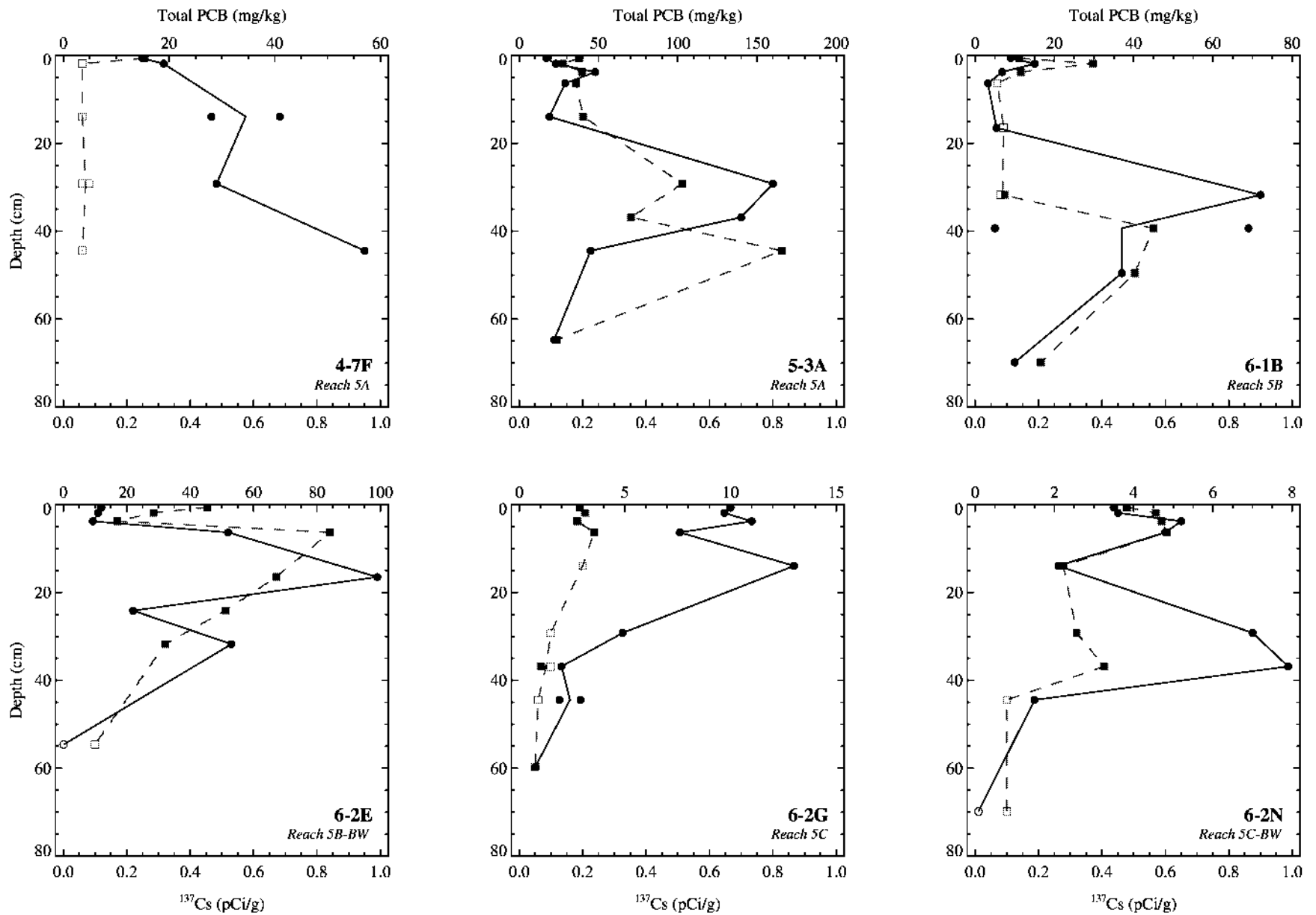
BLASLAND, BOUCK & LEE, INC.   Quantitative Environmental Analysis, LLC

9/26/03   engineers & scientists   4-32
V:\GE_Housatonic_Rest_of_River\Reports and Presentations\RFI Report - Sept Final\70031550 RFI Report.doc

Figure 4-21a. Depth profiles of GE high resolution cores collected within Reach 5 during 1994 - 1995.

Note: Cesium-137 plots are all on the same scale; PCB scales vary by core. Line represents average of duplicate samples.
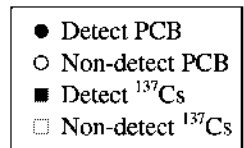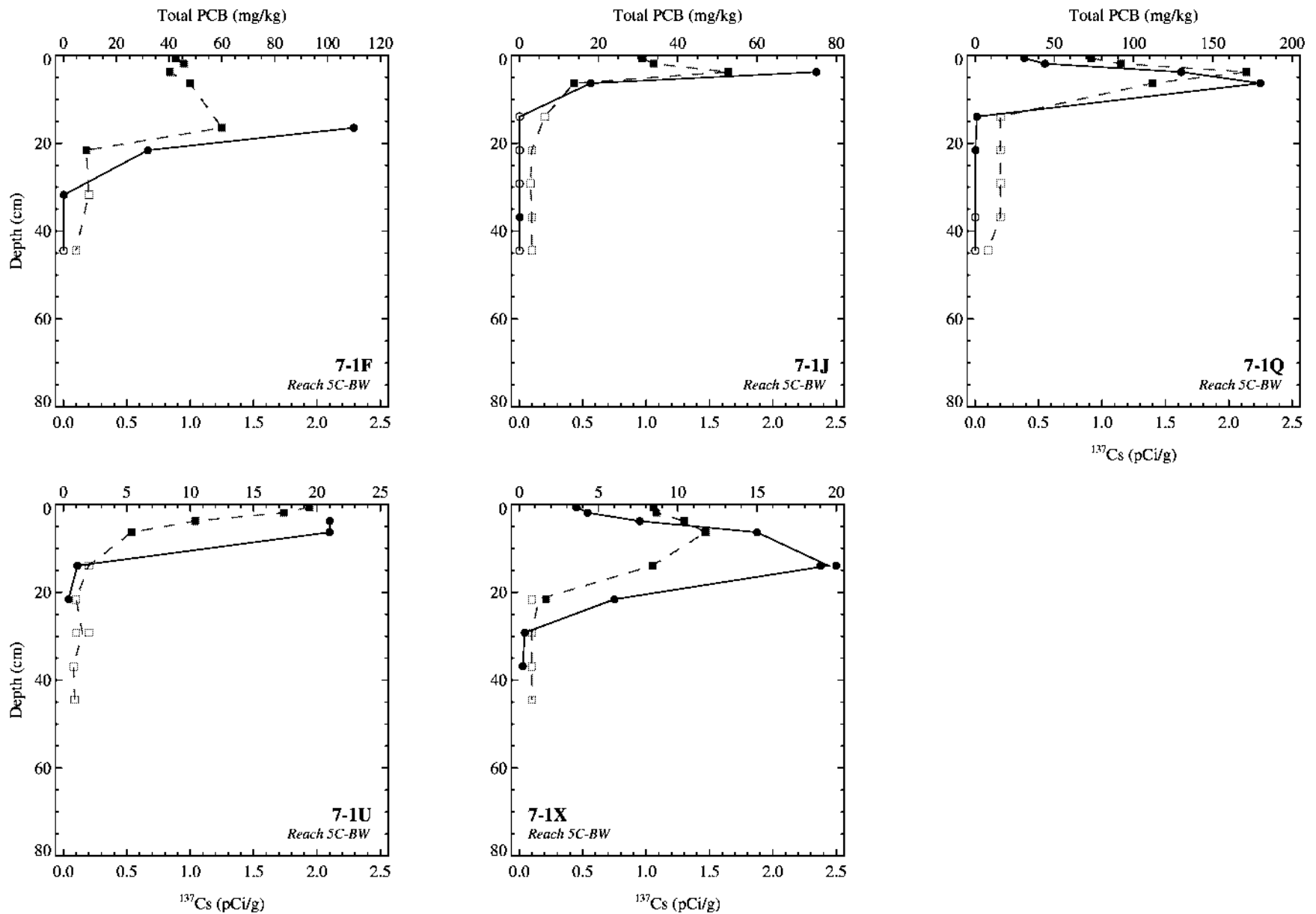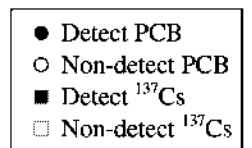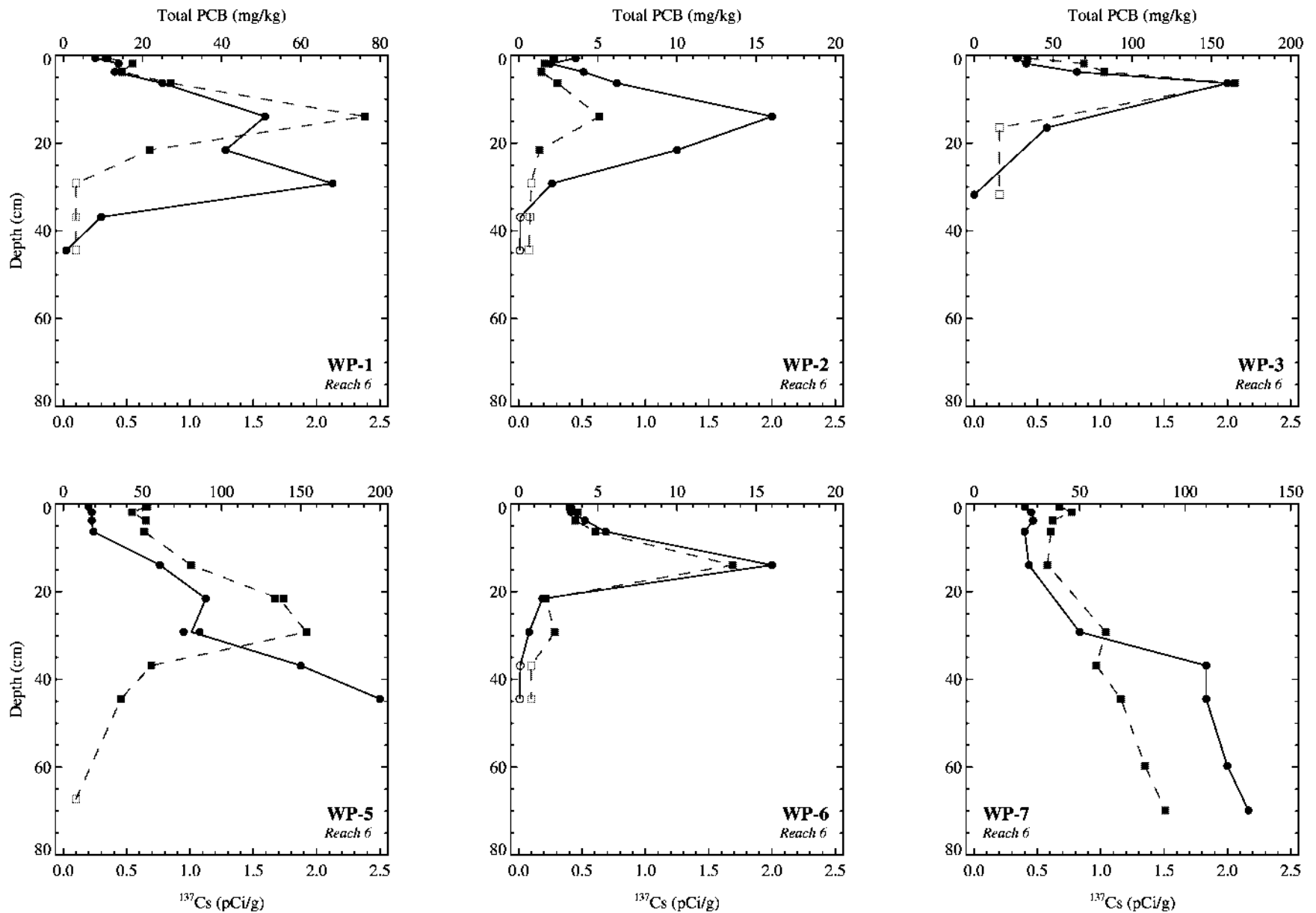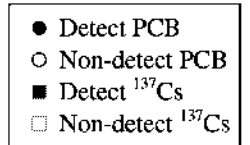
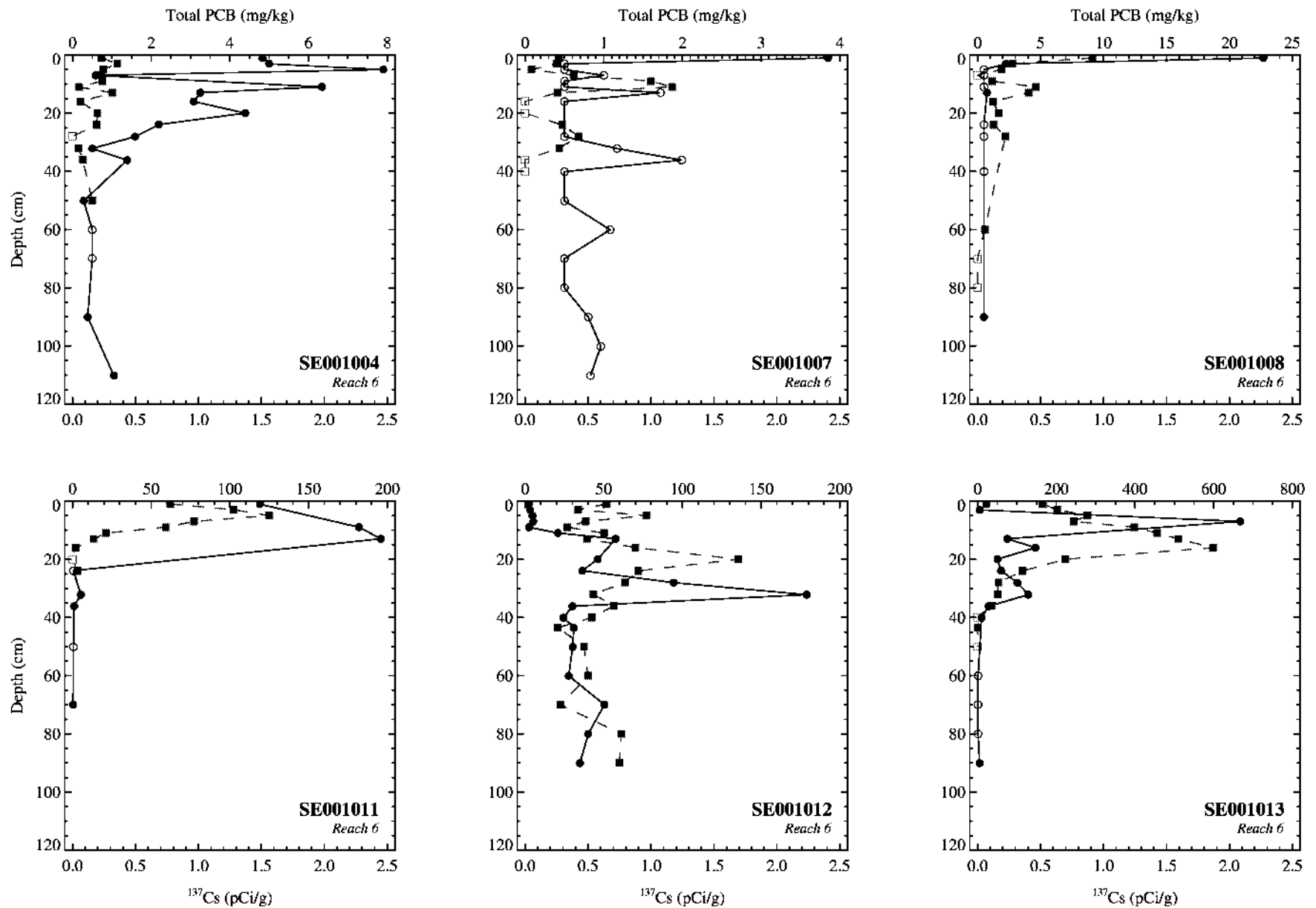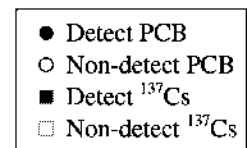**Figure 4-21b. Depth profiles of GE high resolution cores collected within Reach 5 during 1994 - 1995.**

Note: Cesium-137 plots are all on the same scale; PCB scales vary by core. Line represents average of duplicate samples.

Figure 4-21c. Depth profiles of GE high resolution cores collected within Woods Pond during 1994 - 1995.

Note: Cesium-137 plots are all on the same scale; PCB scales vary by core. Line represents average of duplicate samples.
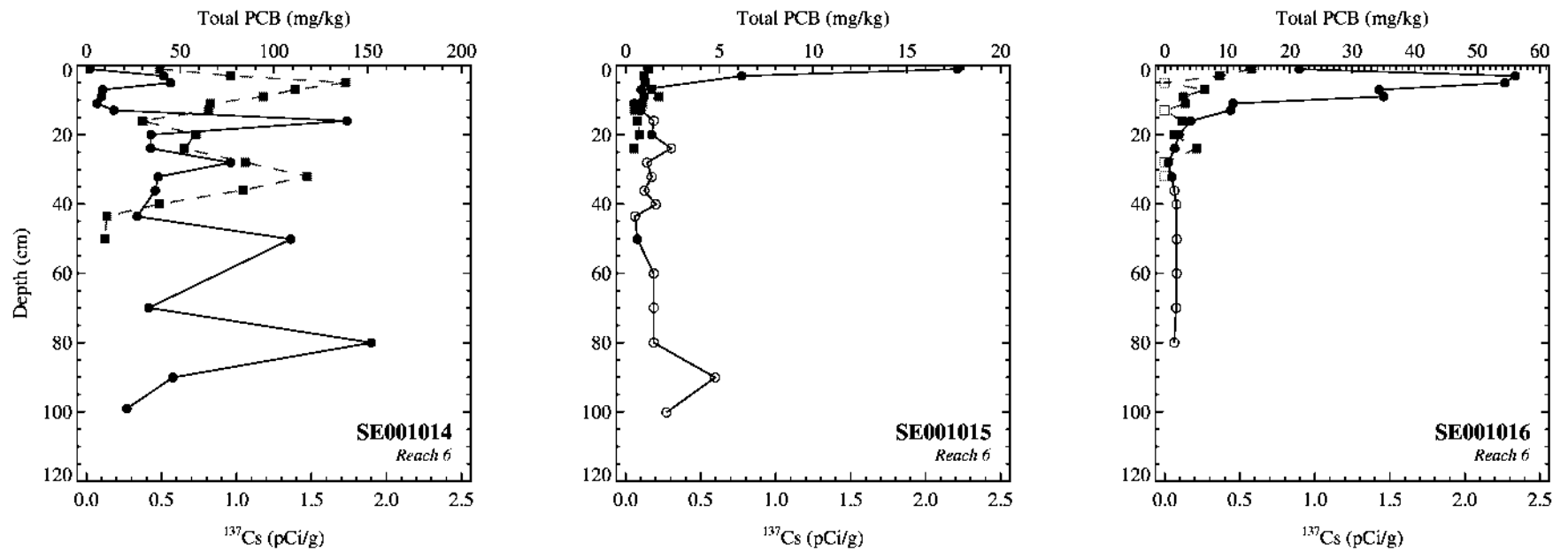
Legend:
- ● Detect PCB
- ○ Non-detect PCB
- ■ Detect ^{137}Cs
- □ Non-detect ^{137}Cs

Figure 4-22a. Depth profiles of EPA high resolution cores collected during 1999.

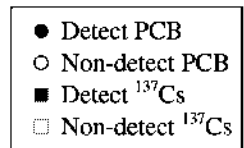*Note: Cesium-137 plots are all on the same scale; PCB scales vary by core. Line represents average of duplicate samples.*

Figure 4-22b. Depth profiles of EPA high resolution cores collected during 1999.

Note: Cesium-137 plots are all on the same scale; PCB scales vary by core. Line represents average of duplicate samples.
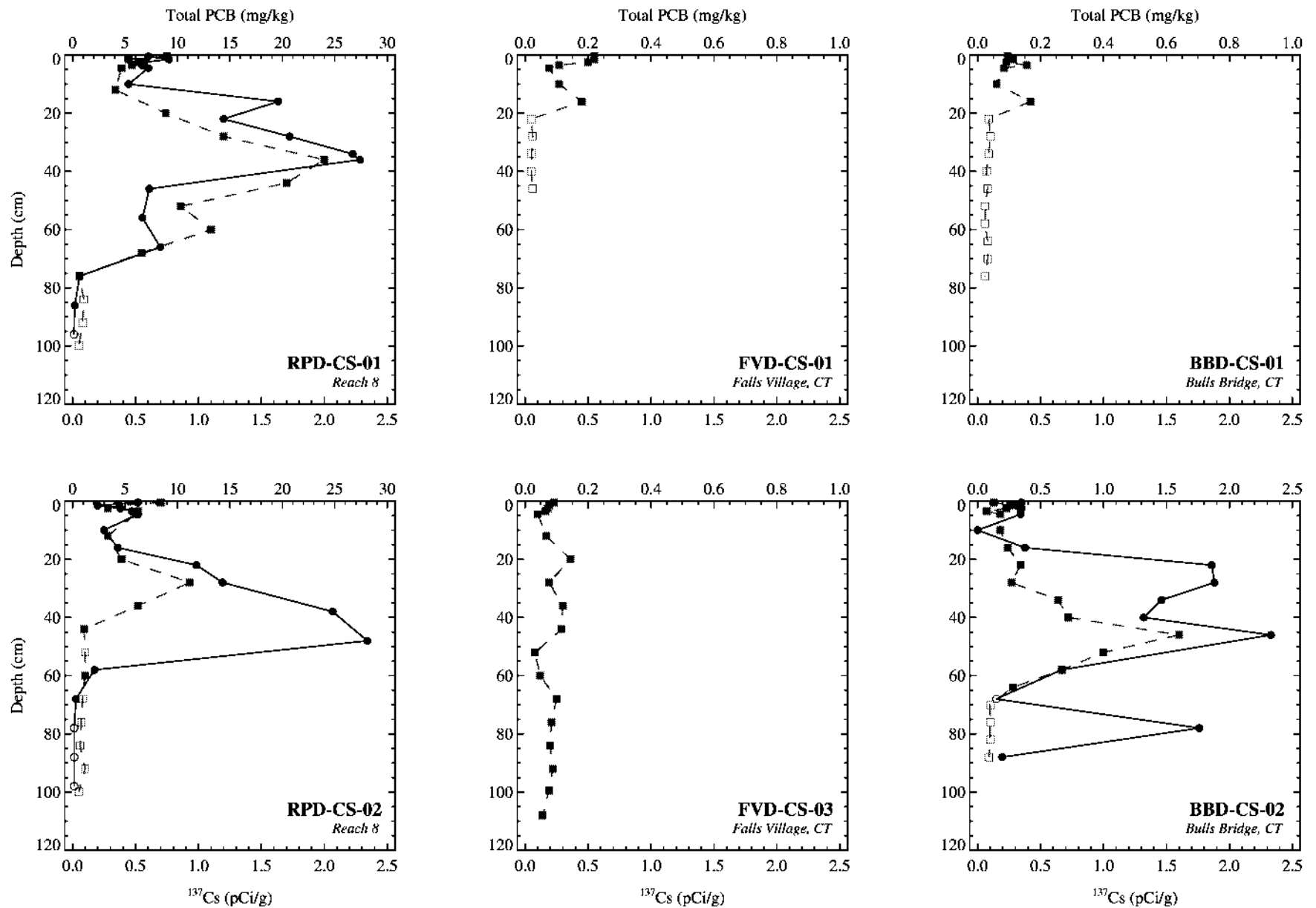
Legend:
- ● Detect PCB
- ○ Non-detect PCB
- ■ Detect ^{137}Cs
- □ Non-detect ^{137}Cs

Figure 4-23. Depth profiles of GE high resolution cores collected during 1998.

Note: Cesium-137 plots are all on the same scale; PCB scales vary by core. Line represents average of duplicate samples.
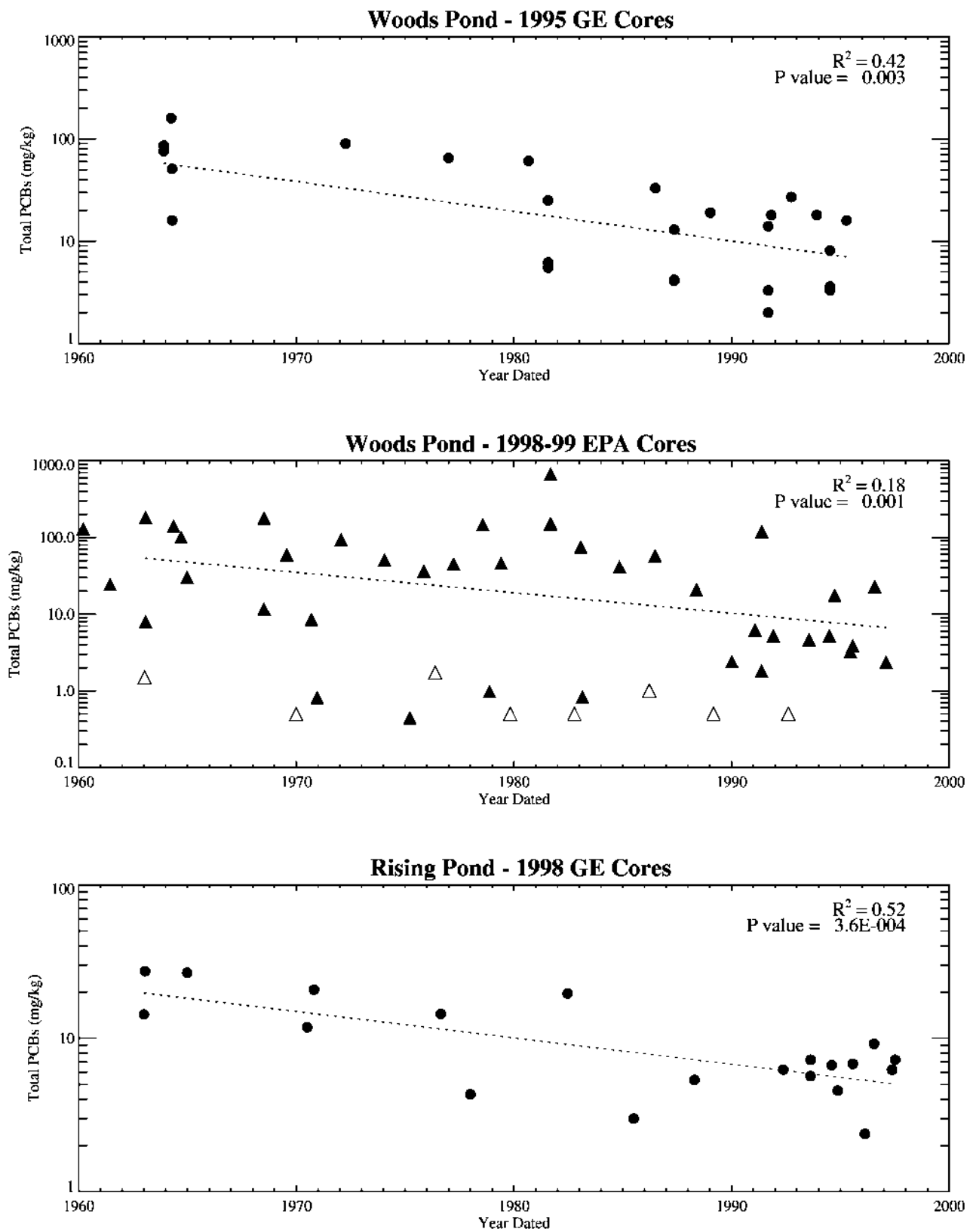
Figure 4-26. Temporal profile of sediment PCB concentrations in Woods Pond and Rising Pond estimated from dated high resolution cores.

Notes: Open symbols denote non-detect PCB data plotted at the MDL. Dating assumes Cs-137 peak in 1963 and constant deposition rate.Regression starts at 1963 and excludes non-detect PCBs.